Examination of different drift gas mixtures for the muon magnetic spectrometer for the SHiP experiment

Untersuchung verschiedener Driftgase für das Myon-Magnetspektrometer im SHiP-Experiment

by

Stefan Bieschke

born:
March 11, 1989
in Bremerhaven

Master thesis

Universität Hamburg

Institut für Experimentalphysik

December 2016

1. supervisor: Prof. Dr. Caren Hagner
2. supervisor: Dr. Daniel Bick

Abstract

The *SHiP* experiment is a newly proposed beam dump experiment at *CERN*, dedicated to the **S**earch for **Hi**dden **P**articles beyond the standard model. Additionally, ν_τ physics is a major topic of research proposed for SHiP. This includes the first-ever observation of the $\bar{\nu}_\tau$, which requires the charge and momentum reconstruction of particles escaping the neutrino interaction vertex. This is going to be the task of the muon magnetic spectrometer. Drift tubes from the decommissioned OPERA experiment are an option for this spectrometer. Due to the high expected event rates, a new drift gas mixture is needed, as the one used in OPERA had a high maximum drift time of about 1.5 μs and a non-linear rt-relation. This would lead to high occupancy. Motivated by results presented in [79], drift gas mixtures containing Argon, Carbon dioxide and Nitrogen were studied regarding their maximum drift time, linearity of the rt-relation, probability of afterpulses and their detection efficiency at *atmospheric pressure*. The drift gas mixture Ar:CO_2:N_2 96:3:1 was found to be the best-suited candidate for future experiments using the drift tubes of the OPERA experiment. The maximum drift time was reduced to about 635 ns, which is approximately 40% of that of the reference gas used in OPERA. The linearity was analyzed with a χ^2-test, showing a significantly more linear behavior. The probability for afterpulses was found to be 0.8%, which is about 3 times higher than at OPERA, but still the lowest for fast and linear gas mixtures. The detection efficiency of 93% is comparable to that of the reference gas in the test setup used for this thesis.

Zusammenfassung

Das SHiP-Experiment ist ein geplantes Experiment am CERN, mit dem Ziel, neue Teilchen zu finden, die über das Standardmodell der Teilchenphysik hinaus gehen. Außerdem ist die Untersuchung von ν_τ, insbesondere die erstmalige Beobachtung des $\bar{\nu}_\tau$, ein experimentelles Ziel. Für letztere Aufgabe ist eine Ladungs- und Impulsrekonstruktion der geladenen Teilchen, die den Neutrinovertex verlassen, unerlässlich. Diese Aufgabe soll vom Myon-Magnet-Spektrometer erfüllt werden. Hierfür ist unter anderem die Verwendung von verbesserten Driftröhren aus dem beendeten OPERA-Experiment vorgesehen. Wegen der hohen Ereignisraten, die bei SHiP erwartet werden, ist die Verwendung einer neuen Driftgasmischung notwendig, da die bei OPERA verwendete Mischung mit einer maximalen Driftzeit von etwa $1,5\,\mu$s eine hohe Totzeit und eine stark nichtlineare Driftzeit-Orts-Beziehung aufweist.

Motiviert durch Ergebnisse von [79] wurden verschiedene Driftgasgemische aus Argon, Kohlenstoffdioxid und Stickstoff bezüglich ihrer maximalen Driftzeit, der Linearität ihrer Driftzeit-Orts-Beziehung, der Wahrscheinlichkeit für Nachpulse, sowie ihrer Nachweiswahrscheinlichkeit untersucht. Die Driftgasmischung Ar:CO_2:N_2 96:3:1 wurde dabei als der vielversprechendste Kandidat für zukünftige Experimente mit den Driftröhren von OPERA identifiziert. Die maximale Driftzeit wurde auf etwa 635 ns und damit auf 40% des Wertes des Referenzgases gesenkt. Die Linearität wurde mit einem χ^2-Test bestimmt und eine deutliche Zunahme der Linearität gegenüber dem zuvor verwendeten Gas festgestellt. Die Wahrscheinlichkeit für Nachpulse liegt bei $0,8\%$, was ungefähr drei mal so hoch ist wie im Vergleich zur alten Gasmischung, jedoch signifikant kleiner als es eine weitere Reduktion des CO_2-Gehalts bewirken würde. Die Nachweiswahrscheinlichkeit ist mit 93% auf einem ähnlich hohen Niveau, wie sie für die Referenzgasmischung gefunden wurde.

Contents

1 Introduction

In high-energy physics, when large areas or volumina need to be instrumented with detectors for charged particle tracking, drift tube detectors are commonly used as they are simple, robust and cost-effective. Their performance largely depends on the drift gas mixture they are operated with. The track reconstruction is based on time measurements. Thus a *linear* relation between drift time and drift distance (rt-relation) is beneficial, as it leads to a more homogeneously distributed spatial resolution along the tube's radius. Additionally, a high drift velocity reduces the maximum drift time, allowing faster signal collection and thus reducing the detector's dead time.

The newly proposed *SHiP* experiment [30, 11] is dedicated to the **S**earch for **Hi**dden **P**articles beyond the standard model of particle physics, as well as detailed studies on the τ neutrino. For the neutrino identification, a charge measurement and momentum reconstruction of the tracks emerging from the vertex is crucial. For the spectrometer performing this task, an improvement of the drift tubes from the decommissioned *OPERA* experiment [49, 36] can be used. The drift gas mixture used in OPERA, however, needs to be replaced by a faster and more linear drift gas mixture, as for the SHiP experiment, a much higher rate of events is expected.

For this thesis, a test setup with a single drift tube of length $L = 30\,\text{cm}$ was rigged up and commissioned. The tube is a shortened tube from the OPERA mass production. The signal readout is performed by a Flash Analog to Digital Converter (FADC) that offers the opportunity to perform detailed studies on the drift tube signals. It was first tested using the drift gas mixture of Ar:CO_2 80:20, that is well known from the OPERA experiment. Additionally, a software for data analysis was developed.

In the tube , several drift gas mixtures of Argon, Carbon dioxide Nitrogen are studied, as these were found to be fast and linear by [79].

The aim of this work is to find a drift gas mixture that provides a more linear rt-relation and faster signal development compared to the drift gas mixture used for the OPERA experiment *at amospheric pressure*. The results presented in [79] are obtained at an absolute gas pressure of 3 bar, leaving it unknown if those results apply to lower gas pressures as well.

The work presented in this thesis is accompanied by additional analyses studying the ability to operate drift tube detectors with a continous triggerless readout. The results are presented in [74].

The structure of this thesis is as follows: An introduction to neutrino physics is given

in chapter 2, including an overview of the current experimental status. As the SHiP experiment focuses on the search for *Heavy Neutral Leptons (HNLs)*, a theoretical focus is placed on the derivation of Dirac-Majorana mass terms and the seesaw mechanism.

The working principle of drift tube detectors is presented in chapter 3. There, the processes of ionization and signal development are explained. Properties of drift gas mixtures and effects on the detector performance are dealt with.

The SHiP experiment is introduced in chapter 4, where a focus is placed on the proposed, experimental setup and ν_τ physics, such as the ability to perform the first-ever direct observation of the $\bar{\nu}_\tau$.

A description of the experimental setup that was used for all measurements presented in this thesis is given in chapter 5. For commissioning first measurements with the reference drift gas mixture, used by the OPERA experiment were performed. Chapter 6 shows the results of the commissioning and gives an introduction to the analysis methods used for all subsequently tested drift gas mixtures.

Chapter 7 shows the experimental results of six additional drift gas mixtures. A summary as well as an outlook can be found in chapter 8.

2 The neutrino

The neutrino, commonly denoted by the greek letter ν, has been an extraordinary particle ever since its proposal in the year *1930*. This chapter will provide a brief overview of the scientific journey to reveal the neutrino's mysteries.

2.1 Historical background

When J.J. Thomson discovered the *electron* by studying *cathode rays* in 1897 [78], he opened a new field of research, known today as elementary particle physics. Thomson estimated the range that a cathode ray could travel through air until it lost its energy through ionization. He discovered that a cathode ray ranges significantly further than it should, assuming it consisted of atom-sized components. So Thomson reasoned that the cathode rays' fundamental component must have been at least *1000* times smaller than an atom. He also measured the spatial deviation of a cathode ray traveling through a magnetic field. Combined with an estimation of the mass by exploring the heat produced when stopping a cathode ray, Thomson was able to conclude that the cathode rays consisted of particles at least *1000* times lighter than the hydrogen atom. Additionally, the mass of the cathode rays' components remains the same, no matter what type of atom the cathode ray was extracted from. The atom could no longer be considered the smallest building block of matter. By about the same time, in 1896, Henri Becquerel discovered radioactivity in Uranium. Radioactivity itself was found to be seperatable into two kinds, known as α- and β-radiation, by *Ernest Rutherford* in 1899.[1] Using J.J. Thomson's method to measure the *charge-to-mass-ratio* e/m of electrons, Becquerel measured e/m for β-radiation, discovering that the ratio was the same as for electrons, therefore concluding that β-radiation consisted of electrons.

2.1.1 The β-decay problem

The β-decay, however, yielded a major problem by the time of its discovery. One was able to detect the remaining nucleus and the emitted electron, so one observed a *two-body decay*. The electron's energy spectrum, however, happens to be a continuous one. According to well known mechanics, a two-body decay is expected to result in the same electron energy for every decay of one decaying atom type, due to the high nucleus mass compared to

[1] The γ-radiation was discovered one year later in 1900.

the electron's mass. So for a continuous spectrum, the law of energy conservation seemed violated.

2.1.2 The neutrino proposal

Ideas arose that in the case of nuclear decays energy might not always be conserved. The Austrian Physicist *Wolfgang Pauli* found a way to explain the continuous energy spectrum of the β-decay as well as a problem with the conservation of angular momentum during β-decays without the need for breaking the conservation laws. He was able to solve the puzzle by introducing a new, yet unobserved particle that is emitted together with the electron during β-decays.

According to Pauli, the newly proposed particle, which he called *neutron*, does not have any electric charge, carries a spin of 1/2 and should have a mass at the same order of magnitude as the electron. He deduced its mass could not exceed one percent of the proton's mass. Today, the neutron proposed by Pauli is known as *neutrino*[2], which it was called by *Enrico Fermi*, who published a theoretical description of the β-decay in 1934 [43]. The nowadays known neutron was discovered in 1932 by James Chadwick [27]. Pauli proposed the *neutrino* must be emitted along the electron in a β-decay, such that the sum of the electron's and the neutrino's energy happen to be constant, thus conserving energy. Because the electron carries a spin 1/2, the alongside emitted neutrino with spin 1/2 conserves the angular momentum as well, since the remaining nucleus carries integral spin values.

Pauli, however, knew about the problems arising with his proposal. As the neutrino had not yet been observed, it became evident that it must be weakly interacting and hard to detect. Not daring to publish his proposal, he first wrote the proposal in an open letter to *Gauvereins-Tagung zu Tübingen*, today commonly known as *Dear radioactive Ladies and Gentlemen*[3] [66]. That proposal led to an understanding of the β-decay. In this process a neutron in the nucleus of a decaying atom transforms into a proton by emitting an electron and a neutrino, specifically an anti-electron-neutrino[4]. This process is written as shown in equation (2.1).

$$ {}^{A}_{Z}X \rightarrow {}^{A}_{Z+1}Y + e^{-} + \bar{\nu}_e \tag{2.1} $$

Here, A is the atom's *mass number*, N its number of nucleons and Z is its number of protons.

[2] *-ino*: italian - small
[3] from German original: *Liebe Radioaktive Damen und Herren*
[4] more in chapter 2.3

2.2 Experimental discovery of the neutrino

A detailed description of the experiments, with which the neutrino was discovered, as well as their historical context can be found in [86, 48, 75].

Following Pauli's proposal of the neutrino, the theory of neutrinos and the weak interaction developed, strongly influenced by Enrico Fermi in the following years. Experiments were designed to observe reactions of the neutrino. As Enrico Fermi's theory of neutrinos states, they only interact via the weak interaction. Thus, they have a small interaction crosssection passing through matter. In order to detect the neutrino in an experiment, a strong, high flux neutrino source is crucial. According to the theory, the strongest sources of neutrinos are nuclear reactors, increasingly being built in the early 1950s. During the fission of ^{235}U, ^{238}U, ^{239}Pu and ^{241}Pu, nuclei with a high neutron count are likely to decay via β^--decay, emitting anti neutrinos $\bar{\nu}_e$ alongside the emitted electron. In 1953, *Clyde L. Cowan* and *Frederick Reines* set up an experiment to discover the anti neutrino at the *Hanford reactor* in the USA, using about 300 liters of liquid scintillator looking for the reaction as shown in (2.2).

$$\bar{\nu}_e + p \rightarrow e^+ + n \tag{2.2}$$

Even though the experiment lacked proper background shielding and had a small volume of liquid scintillator detector, a vague signal could be observed. Hence, a follow-up experiment was set up, today known as the Cowan-Reines-experiment. The follow-up experiment was improved by using a total of 4000 liters of liquid scintillator and providing the detector with stronger background shielding [32]. The experimental discovery of the neutrino could be performed in this *Poltergeist* experiment, thus during Pauli's lifetime. Reines was awarded the *Nobel prize for physics 1995* for the discovery of the neutrino. The muon neutrino was discovered in 1963 by Lederman, Schwartz and Steinberger [33]. They showed that a second kind of neutrino existed, which was associated with muons instead of electrons, by observing that interacting muon neutrinos produce muons instead of electrons, thus must be different from electron neutrinos. They were rewarded the 1988 *Nobel prize for physics*.

The τ neutrino ν_τ was discovered at Fermilab by the DONuT experiment [52]. As they could not distinguish between neutrino and antineutrino, the $\bar{\nu}_\tau$ yet remains undiscovered. The SHiP experiment[5], however, has the first ever ability to discover that last neutrino.

2.3 The neutrino within the standard model of particle physics

Within the standard model of particle physics *(SM)*, neutrinos are among the fermions, more specifically the leptons. Each charged lepton has an associated neutrino. Neutrinos

[5] see chapter 4

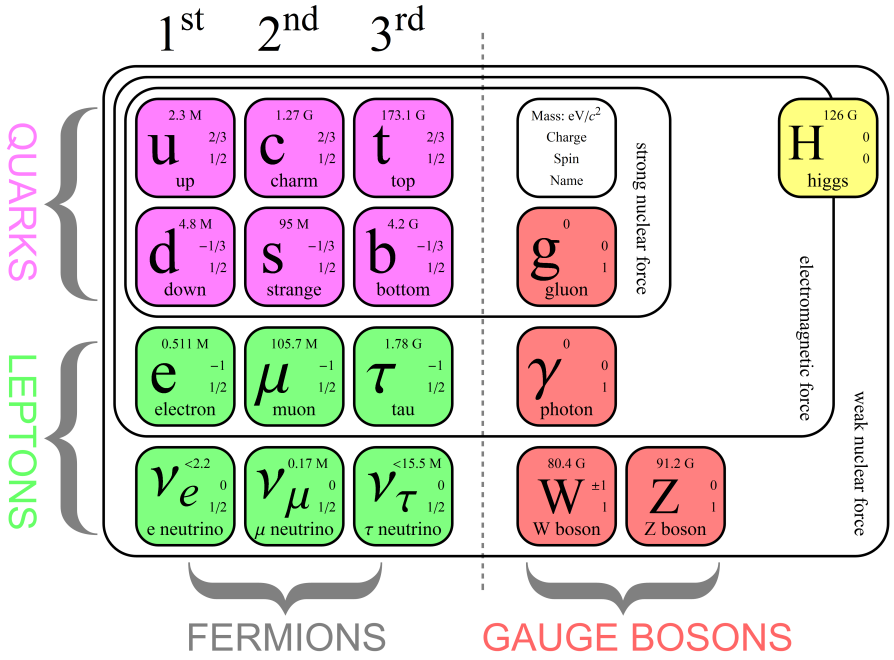

Figure 2.1: Schematic view of the particles within the Standard Model of particle physics. Note, that each fermion has an antimatter partner which is not shown here [80].

carry a lepton number of $L = +1$, antineutrinos $L = -1$ accordingly. The flavor lepton number for a flavor $\alpha \in \{e, \mu, \tau\}$, is consequently given as $L_\alpha(\nu_\alpha) = +1$ and $L_\alpha(\bar{\nu}_\alpha) = -1$. They do not carry electric or color charge, thus do only interact via the weak interaction. Following the SM, they all have a zero-mass[6], which, as an experimental fact, is not true. This shows, theories beyond the standard model must arise, details are shown in the following text. Figure 2.1 shows the three neutrino flavors among the other particles of the SM. Throughout the following text, so called natural units will be used, especially

$$\hbar = c = 1.$$

All derivations will closely follow [86].

2.3.1 Chirality and helicity

Since neutrinos are fermions, they are described by the *Dirac equation* which represents their relativistic wave-equation, as shown in (2.3) [86].

$$\left(i\gamma_\mu \frac{\partial}{\partial x_\mu} - m\right)\psi = 0 \tag{2.3}$$

[6] 2.3.2

Here, Einstein's summing conventions were used. ψ is the four-component spinor and the γ matrices are given as:

$$\gamma_0 = \begin{bmatrix} \mathbf{1} & 0 \\ 0 & -\mathbf{1} \end{bmatrix}, \qquad \gamma_i = \begin{bmatrix} 0 & \sigma_i \\ -\sigma_i & 0 \end{bmatrix} \tag{2.4}$$

In (2.4) $\mathbf{1}$ denotes the 2×2 identity matrix and σ_i the 2×2 Pauli matrices. Note, γ_μ are 4×4 matrices [86]. Furthermore, we can introduce a matrix γ_5 defined as:

$$\gamma_5 = i\gamma_0\gamma_1\gamma_2\gamma_3 = \begin{bmatrix} 0 & \mathbf{1} \\ \mathbf{1} & 0 \end{bmatrix} \tag{2.5}$$

Using these matrices, the chiral projection operators P_L and P_R can be introduced as:

$$P_L = \frac{1}{2}(1 - \gamma_5) \tag{2.6}$$

$$P_R = \frac{1}{2}(1 + \gamma_5) \tag{2.7}$$

The projection operators follow the relations [86]:

$$\begin{aligned} P_L P_R &= 0 \\ P_L + P_R &= 1 \\ P_L^2 &= P_L \\ P_R^2 &= P_R \end{aligned} \tag{2.8}$$

Applying the projection operators to any spinor ψ that is a solution to the Dirac equation, the chiral projections $\psi_{L,R}$ of ψ can be defined [86] as:

$$\psi_L = P_L\psi \qquad \psi_R = P_R\psi \tag{2.9}$$

The chiral projection spinor ψ_L is called *left-handed*, ψ_R *right-handed*. Due to their definitions, the chiral projection spinors are eigenfunctions to γ_5 and follow the eigenequation shown in (2.10).

$$\gamma_5\psi_{L,R} = \mp\psi_{L,R} \tag{2.10}$$

The eigenvalues of (2.10) are called *chirality* [86]. Because of (2.9) and (2.8), the spinor ψ can be written as the sum of its chiral projections.

From the Dirac equation (2.3), a system two coupled differential equations can be obtained by several operations including chiral projections, described in [86]. They are

given in (2.11) and (2.12) [86].

$$\left(i\frac{\partial}{\partial x^0} - i\sigma_i\frac{\partial}{\partial x_i}\right)\psi_R = m\gamma_0\psi_L \tag{2.11}$$

$$\left(i\frac{\partial}{\partial x^0} + i\sigma_i\frac{\partial}{\partial x_i}\right)\psi_L = m\gamma_0\psi_R \tag{2.12}$$

This system of differential equations decouples for $m = 0$, resulting in the *Schrödinger equation*. Therefore, the chiral projection spinors are eigenfunctions to the *Helicity operator*, as given in (2.13), as well.

$$\mathcal{H} = \frac{\sigma \cdot \mathbf{p}}{|\mathbf{p}|} \tag{2.13}$$

The Helicity operator describes a projection of a particle's spin on its momentum. In case of massless particles, the spinor ψ_L is the eigenfunction of $\mathcal{H}$ with eigenvalue $+1$ for particles and -1 for antiparticles and ψ_R vice-versa. For a vanishing mass, helicity and chirality are identical, which is not true for masses different from zero, where (2.11) and (2.12) can not be decoupled [86].

2.3.2 Dirac and Majorana mass terms

In the following text, ψ^c denotes the *charge conjugation* of ψ, thus the spinor for the anti-particle of ψ.

The wave equation for relativistic fermions, the *Dirac equation*, can be deduced with the *Euler-Lagrange* equation from a *Lagrangian*, which is shown in equation (2.14).

$$\mathcal{L} = \bar{\psi}\left(i\gamma_\mu\frac{\partial}{\partial x_\mu} - m_D\right)\psi \tag{2.14}$$

The first term of the Lagrangian describes the kinetic energy of the fermion, the second term is called the *mass term*. Thus, the Dirac mass term is:

$$\mathcal{L} = m_D\psi\bar{\psi} \tag{2.15}$$

When requiring the Lagrangian $\mathcal{L}$ to be Hermitian, the Hermitian adjoint Lagrangian $L^\dagger$, defined by

$$\langle\psi|\mathcal{L}|\phi\rangle = \left(\langle\phi|\mathcal{L}^\dagger|\psi\rangle\right)^*$$

must be equal to the Lagrangian, therefore

$$\mathcal{L} = \mathcal{L}^\dagger.$$

The above mentioned requirement to the Lagrangian implies the Dirac mass m_D from equation (2.15) needs to be real. Using the chiral components, for any two spinors,

equation (2.16) is valid.

$$\bar{\psi}\phi = (\bar{\psi}_L + \bar{\psi}_R)(\phi_L + \phi_R) = \bar{\psi}_L\phi_R + \bar{\psi}_R\phi_L \tag{2.16}$$

Using (2.16), the Dirac mass term can be written as *Weyl spinors* as shown in (2.17).

$$\mathcal{L} = m_D \left(\bar{\psi}_L\psi_R + \bar{\psi}_R\psi_L\right) \tag{2.17}$$

where

$$\bar{\psi}_R\psi_L = \left(\bar{\psi}_L\psi_R\right)^\dagger .$$

When (2.17) is applied to neutrinos, both chiralities of neutrinos must have a dirac mass term as shown above. The standard model, however, only allows left-handed neutrinos, thus they have no Dirac mass.

By introducing the *Majorana mass* m_M, which is in general complex, another hermitian mass term, the so called *Majorana mass term* as shown in equation (2.18) can be introduced.

$$\mathcal{L} = \frac{1}{2}(m_M\bar{\psi}\psi^c + m_M^*\bar{\psi}^c\psi) \tag{2.18}$$

Utilizing the chiral projection operators on the Majorana mass term, two new hermitian mass terms can be written as shown in (2.19) and (2.20).

$$\mathcal{L}^L = \frac{1}{2}m_L(\bar{\psi}_L\psi_R^c + \bar{\psi}_R^c\psi_L) \tag{2.19}$$

$$\mathcal{L}^R = \frac{1}{2}m_R(\bar{\psi}_L^c\psi_R + \bar{\psi}_R\psi_L^c) \tag{2.20}$$

Here, m_L and m_R are real majorana masses since the mass term is required to be hermitian.

The most general mass term that can be written now, is the *Dirac-Majorana mass term*, which is the combination of the Dirac- and the Majorana mass term. The Dirac-Majorana mass term is show in equation (2.21).

$$2\mathcal{L} = \bar{\Psi}_L M\Psi_R^c + \bar{\Psi}_R^c M\Psi_L \tag{2.21}$$

In equation (2.21), M denotes the matrix:

$$M = \begin{bmatrix} m_L & m_D \\ m_D & m_R \end{bmatrix} \tag{2.22}$$

and the fields $\Psi_{L,R}$ are:

$$\Psi_L = \begin{pmatrix} \psi_L \\ \psi_L^c \end{pmatrix} = \begin{pmatrix} \psi_L \\ (\psi_R)^c \end{pmatrix}$$
$$(\Psi_L)^c = \begin{pmatrix} (\psi_L)^c \\ \psi_R \end{pmatrix} = \begin{pmatrix} \psi_R^c \\ \psi_R \end{pmatrix} = \Psi_R^c$$

If CP conservation is required, all elements of M must be real. It comes as an experimental fact, that for interactions of real neutrinos, only the fields ψ_L and ψ_R^c are in effect. Those are often referred to as *active neutrinos*. The fields ψ_R and ψ_L^c do not interact and are called *sterile neutrinos*. In the following text, the active neutrinos will be denoted by the letter ν, the sterile neutrinos with an N. Following this, we get:

$$\psi_L = \nu_L$$
$$\psi_L^c = N_L$$
$$\psi_R = N_R$$
$$\psi_R^c = \nu_R$$

With these notations, equation (2.21)can be written as

$$2\mathcal{L} = m_D(\bar{\nu}_L N_R + \bar{N}_L^c \nu_R^c) + m_L \bar{\nu}_L \nu_R^c + m_R \bar{N}_L^c N_R + h.c, \tag{2.23}$$

where $h.c$ denotes the Hermitian conjugate. The mass eigenstates happen to be:

$$\psi_{1L} = \cos\theta\psi_L - \sin\theta\psi_L^c \qquad \psi_{1R}^c = \cos\theta\psi_R^c - \sin\theta\psi_R \tag{2.24}$$
$$\psi_{2L} = \sin\theta\psi_L + \cos\theta\psi_L^c \qquad \psi_{2R}^c = \sin\theta\psi_R^c + \cos\theta\psi_R \tag{2.25}$$

The mixing angle θ is given by:

$$\tan(2\theta) = \frac{2m_D}{m_R - m_L} \tag{2.26}$$

The mass eigenvalues are

$$m_{1,2} = \frac{1}{2}\left((m_L + m_R) \pm \sqrt{(m_L - m_R)^2 + 4m_D^2}\right). \tag{2.27}$$

A special case of the mass eigenvalues follows from the assumption $m_R \gg m_D$ and $m_L = 0$ as the left handed, sterile neutrino shall not participate in the weak interaction. This corresponds to $\theta \ll 1$, the mass eigenstates can now be written as [86]:

$$m_\nu \equiv m_1 = \frac{m_D^2}{m_R}, \qquad m_N \equiv m_2 = m_R\left(1 + \frac{m_D^2}{m_R^2}\right) \approx m_R \tag{2.28}$$

Here, the subscript ν denotes the mass eigenstate of an active neutrino, N of a sterile neutrino.

This is a possibility to explain the huge mass difference between active neutrinos and all the other fermions. It states that neutrinomasses might be a mixed state of heavy (but non interacting) *sterile neutrino* states and very light *active neutrino* states. The mechanism of mass mixing small Dirac masses with much larger Majorana masses is called the *seesaw mechanism* [60, 61, 69, 65, 11].

The before-mentioned remarks deal with only one neutrino flavor, this can be generalized to n flavors, which is not shown in detail here. By writing the Weyl spinors ν_L and N_R as n-dimensional vectors in flavor-space, the elements of the mass matrix M, given in equation (2.22), each become matrices of size $n \times n$, thus M has dimension $2n \times 2n$. Again, the Dirac-Majorana mass term can be achieved by multiplying (2.21) with the new mass matrix M and the n-dimensional vectors ν_L and N_R. For more information see [86] and the references given there.

2.4 Modern neutrino physics

Since its very beginning, the exploration of the neutrinos' properties has evolved to a major topic of physical research, nowadays known as neutrino physics. A number of problems concerning neutrinos evolved, which are not yet completely understood by the time of writing this thesis. The following section gives an introduction of today's problems in neutrino physics.

2.4.1 Neutrino oscillations

A detailed description of neutrino oscillations and experiments that lead to their examination is given in [86], this text will be closely followed. This section briefly summarizes the mathematical description of neutrino oscillations and their detection in the *Homestake and Kamiokande* experiments. When Raymond Davis began running an experiment to measure solar neutrinos in 1968 [35, 34, 29], he found that an amount of neutrinos was measured that was significantly lower than what was expected following the *standard solar model* [76]. The deficit of detected neutrinos is known today as the *solar neutrino problem.* The detection of the neutrinos emerging the sun was performed using the radiochemical reaction shown in (2.29), which has an energy threshold of 814 keV. The threshold, however, does not allow for the measurement of neutrinos from primary proton-proton fusion in the sun, known as *pp-neutrinos*[7].

$$^{37}\mathrm{Cl} + \nu_e \rightarrow ^{37}\mathrm{Ar} + e^- \tag{2.29}$$

[7] for details on the standard solar model see [76]

The Argon atoms decay via β decay back to chlorine with a half-life of 35 days as shown in (2.30).

$$^{37}\mathrm{Ar} \rightarrow ^{37}\mathrm{Cl} + e^- + \bar{\nu}_e \tag{2.30}$$

The flux of solar neutrinos measured by the Homestake experiment was significantly lower than what was expected, following the standard solar model. The method used for measuring the solar neutrino flux, however, is only sensitive to electron neutrinos, as it uses a *charged current (CC)* reaction, that is mediated by $W^{\pm}$ bosons.

The problem with the too low solar neutrino flux could be solved with the *Sudbury Neutrino Observatory (SNO)* [57] and *(Super-)Kamiokande* [44] experiments. Both of them were sensitive to all neutrino flavors by using the *neutral current (NC)* and *electron scattering (ES)* channels as well. They are both mediated by neutral Z^0 bosons. In the SNO experiment, for the first time a flux of muon and tau neutrinos from the sun could be measured, leading to the idea of neutrino oscillations, because, following the standard solar model, only electron antineutrinos should be emitted by the thermonuclear reactions powering the sun. With the SNO experiment, evidence for the *disappearance of electron type neutrinos* was found [7].

The detection channels for the SNO experiment, using *heavy water* as detection medium are shown below:

$$\begin{aligned} \nu_e + {}^2\mathrm{H} &\rightarrow e^- + p + p && (CC) \\ \nu_x + {}^2\mathrm{H} &\rightarrow \nu_x + p + n && (NC) \\ \nu_x + e^- &\rightarrow \nu_x + e^- && (ES) \end{aligned}$$

With the Super-Kamiokande experiment [63, 44], a flux of muon neutrinos from the atmosphere as a function of the zenith angle was measured, complementing the results from SNO [11]. Atmospheric muon neutrinos originate from cosmic particles, mainly protons, interacting on molecules in the Earth's atmosphere, producing pions. These pions decay, mainly via $\pi^{\pm} \rightarrow \mu^{\pm} + \nu_{\mu}^{(c)}$, followed by the decay of the muon via $\mu^{\pm} \rightarrow e^{\pm} + \nu_{\mu}^{(c)} + \nu_e^{(c)}$. Thus, a rate of muon type neutrinos over electron type neutrinos is assumed to be around 2. Here, a *disappearance of muon type neutrinos* was found, hinting at all active neutrino flavors participating in neutrino oscillations [45].

For the discovery of neutrino oscillations, *Arthur B. McDonald*, for his work on the SNO experiment and *Takaaki Kajita*, for his work on the Super-Kamiokande experiment, were awarded the *Nobel Prize for physics 2015*.

In order to enable a neutrino of flavor $\alpha \in \{e, \mu, \tau\}$ to oscillate into another flavor, neutrinos flavor states must be a linear superposition of mass eigenstates with masses different from zero. The mass eigenstates $|\nu_i\rangle$ mix to flavor states $|\nu_\alpha\rangle$ via the matrix element $U_{\alpha i}$ of a unitary matrix U as shown in equation (2.31). The following text deals

with neutrino states, each deliberation is valid for anti-neutrinos by substituting $U_{\alpha i}$ by its complex conjugate $U^*_{\alpha i}$.

$$|\nu_\alpha\rangle = \sum_i U_{\alpha i}|\nu_i\rangle \tag{2.31}$$

The mass eigenstates, on the other hand, can be deduced using (2.32).

$$|\nu_i\rangle = \sum_\alpha U^\dagger_{i\alpha}|\nu_\alpha\rangle \tag{2.32}$$

Assuming a finite number of n flavor eigenstates, they follow

$$\langle\nu_\alpha|\nu_\beta\rangle = \delta_{\alpha\beta};$$

the n mass eigenstates accordingly

$$\langle\nu_i|\nu_j\rangle = \delta_{ij}.$$

For n eigenstates in flavor and mass, the unitary matrix of size $n \times n$ has a number of n^2 parameters. Thus, $2n$ neutrino states with $2n-1$ relative phases exist and the set of parameters of the matrix U can be reduced to $(n-1)^2$ independent parameters. Those parameters are commonly chosen to be $\frac{1}{2}n(n-1)$ mixing angles of a rotational matrix and $\frac{1}{2}(n-1)(n-2)$ CP violating phases.

The time-evolution of a mass eigenstate $|\nu_i\rangle$ is achieved by multiplying the time-evolution operator $U_t = e^{-iE_it}$ to the mass eigenstate at time $t = 0$ as shown in equation (2.33).

$$|\nu_i(x,t)\rangle = e^{-iE_it}|\nu_i(x,0)\rangle \tag{2.33}$$

$$E_i = \sqrt{m_i^2 + p_i^2} \approx p_i + \frac{m_i^2}{2p_i} \approx E_i + \frac{m_i^2}{2E_i} \tag{2.34}$$

In equation (2.34), the assumptions of $p_i \gg m_i$ in the first approximation and accordingly $E \approx p$ in the second approximation were made.

The time evolution of a neutrino state emitted as $|\nu_\alpha\rangle$ at time $t = 0$ is given by equation (2.35).

$$|\nu(x,t)\rangle = \sum_i U_{\alpha i}e^{-iE_it}|\nu_i\rangle = \sum_{i,\beta} U_{\alpha i}U^*_{\beta i}e^{ipx}e^{-iE_it}|\nu_\beta\rangle \tag{2.35}$$

The transition amplitude to the flavor eigenstate $|\nu_\beta\rangle$ in this state $|\nu(x,t)\rangle$ is given by

$$A_{\alpha\to\beta}(t) = \langle\nu_\beta|\nu(x,t)\rangle.$$

Hence, the probability of measuring an eigenstate $|\nu_\beta\rangle$ in an emitted $|\nu(x,t)\rangle$ is

$$P_{\alpha\to\beta} = |\langle\nu_\beta|\nu(x,t)\rangle|^2 = \sum_i \sum_j U_{\alpha i} U^*_{\alpha j} U^*_{\beta i} U_{\beta j} e^{-i(E_i - E_j)t}. \tag{2.36}$$

The term given in (2.36) can be summarized to:

$$P_{\alpha\to\beta} = \sum_i |U_{\alpha i} U^*_{\beta i}|^2 + 2\,\mathrm{Re} \sum_{j>i} U_{\alpha i} U^*_{\alpha j} U^*_{\beta i} U_{\beta j} \exp\left(-i \frac{\Delta m^2_{ij}}{2} \frac{L}{E}\right) \tag{2.37}$$

In (2.37), we used

$$\Delta m^2_{ij} = m^2_i - m^2_j$$

and

$$L = ct.$$

As equation (2.37) states, the measurement of neutrino oscillations can not reveal absolute neutrino masses, as they are only sensitive to Δm^2. If CP invariance is required, equation (2.37) can be further simplified to:

$$P_{\alpha\to\beta} = \delta_{\alpha\beta} - 4 \sum_{j>i} U_{\alpha i} U_{\alpha j} U_{\beta i} U_{\beta j} \sin^2\left(\frac{\Delta m^2_{ij}}{4} \frac{L}{E}\right) \tag{2.38}$$

The matrix U, often denoted as U_{PMNS} after Pontecorvo, Maki, Nakagawa and Sakata [67, 56], is unitary. Note the analogy to the CKM mixing matrix in the quark sector [25, 51]. One possible factorization of the matrix U_{PMNS} is:

$$\begin{aligned}
U_{\mathrm{PMNS}} &= U_{12} \times U_{23} \times U_{13}, \\
U_{12} &= \begin{bmatrix} c_{12} & s_{12} & 0 \\ -s_{12} & c_{12} & 0 \\ 0 & 0 & 1 \end{bmatrix}, \\
U_{23} &= \begin{bmatrix} 1 & 0 & 0 \\ 0 & c_{23} & s_{23} \\ 0 & -s_{23} & c_{23} \end{bmatrix}, \\
U_{13} &= \begin{bmatrix} c_{13} & 0 & s_{13} e^{i\delta} \\ 0 & 1 & 0 \\ -s_{13} e^{i\delta} & 0 & c_{13} \end{bmatrix}.
\end{aligned}$$

with:

$$\begin{aligned} c_{ij} &= \cos(\theta_{ij}), \\ s_{ij} &= \sin(\theta_{ij}), \\ \delta &\widehat{=} \text{ CP violating phase.} \end{aligned}$$

In the case of the existence of sterile neutrinos, the oscillation matrix needs to be extended, which will not be described here.

Two flavor oscillation A common approximation is the reduction to an oscillation of two neutrino flavors. This approximation can be made since the mass squared mass differences Δm^2_{12} and $\Delta m^2_{23} \approx \Delta m^2_{13}$ show a large difference and the length scales of the oscillation are not comparable. Thus, a decoupling of the three neutrino mixing is possible. The mixing matrix U can then be written as a rotational matrix, that mixes the mass eigenstates $\nu_{1,2}$ to flavor eigenstates $\nu_{e,\mu}$ as shown in equation (2.39).

$$\begin{pmatrix} \nu_e \\ \nu_\mu \end{pmatrix} = \begin{bmatrix} \cos(\theta) & \sin(\theta) \\ -\sin(\theta) & \cos(\theta) \end{bmatrix} \begin{pmatrix} \nu_1 \\ \nu_2 \end{pmatrix} \tag{2.39}$$

The probability to measure a muon neutrino, that was emitted as electron neutrino (or vice-versa) is given by equation (2.40).

$$P_{\nu_e \to \nu_\mu} = P_{\nu_\mu \to \nu_e} = P_{\bar{\nu}_e \to \bar{\nu}_\mu} = P_{\bar{\nu}_\mu \to \bar{\nu}_e} = \sin^2(2\theta) \sin^2\left(\frac{\Delta m^2}{4} \frac{L}{E}\right) \tag{2.40}$$

In this notation, the mixing angle theta denotes θ_{12}, L is the distance between the neutrino emitter and the location where it is measured with energy E.

2.4.2 Experimental status on neutrino physics

Mixing angles and mass differences As described above, the mixing angles as well as the mass differences can be measured with neutrino oscillation experiments. The observation of solar neutrino oscillations with SNO was confirmed by the *KamLAND* experiment [41], which measured the disappearance of reactor neutrinos. The atmospheric oscillation, first observed with Super-Kamiokande was confirmed by the *MINOS* [59] and *K2K* [12] experiments both observing the disappearance of muon neutrinos in a muon neutrino beam from accelerators. The oscillation of electron neutrinos to tau neutrinos was found with the reactor neutrino experiments *Daya Bay* [13, 14], *RENO* [8] and *Double Chooz* [4] as well as the neutrino beam experiment *T2K* [3], which operated at a very different energy scale. A global fit to the oscillation parameters using the above mentioned experiments is presented in [47], a summary of the global fit results from [11] is shown in table 2.1.

Table 2.1: Mass differences and neutrino mixing angles as a result from a recent, global fit performed in [47] and summarized by [11]. The term *idem* states that this quantity could not have been determined yet.

	Δm^2_{sol} (eV^2)	Δm^2_{atm} (eV^2)	$\theta_{12}(^\circ)$	$\theta_{23}(^\circ)$	$\theta_{13}(^\circ)$	$\delta(^\circ)$
NH	$7.5(2)\cdot 10^{-5}$	$2.46(5)\cdot 10^{-3}$	33.5(8)	$42.3^{+3}_{-1.6}$	8.5(2)	306^{+39}_{-70}
IH	idem	$-2.45(5)\cdot 10^{-3}$	idem	$49.5^{+1.5}_{-2.2}$	idem	254^{+63}_{-62}

Mass hierarchy and mass scale As shown in chapter 2.4.1, measurements of neutrino oscillations do not allow the direct measurement of neutrino masses but are only sensitive to the mass differences Δm^2_{ij} of the states i and j. Upper boundaries on neutrino masses, however, can be determined for example by studying the high-energy cutoff in the β spectrum of tritium. Another important upper boundary of neutrino masses could be set with the observation of neutrinos from the supernova *SN1987A*. From that supernova, 19 neutrinos were observed that arrived within a timeframe of ten seconds with a certain range of energies. As massive particles, their velocity depends on their energy and from the fact that the time interval of their arrival is rather small, an upper limit on neutrino masses of

$$m_\nu < 20\frac{\text{eV}}{c^2}$$

could be established [48].

As the mass differences Δm^2_{12} and Δm^2_{23} are known from experiments, it is not yet known, if the masses are ordered in the so-called *normal hierarchy*, or the *inverted hierarchy*. While in the first case, the masses would be ordered as $m_1 < m_2 < m_3$, the latter case would imply $m_3 < m_1 < m_2$. The two hierarchies, however, would result in a slight difference in the probability of a specific flavor state in neutrino oscillations. The mass hierarchies are illustrated in figure 2.2. For a recent review, see [68, 46].

Due to the relatively *large* mixing angle $\theta_{13} \approx 8.4^\circ$, the mass hierarchy can be determined by oscillation experiments in the near future. One experiment being built by the time of writing of this thesis is the *Jiangmen Underground Neutrino Observatory (JUNO)* experiment [38], which is aimed at finding the mass hierarchy that is realized in nature. Figure 2.3 shows the expected spectra of anti neutrinos from nuclear reactors with normal and inverted mass hierarchy. Being able to distinguish between the differences in the spectra between the two hierarchies is an ambitious project, that requires an exceptionally high energy resolution for large scale detectors.

The absolute mass of neutrinos, however, remains yet unknown.

2.4.3 Sterile neutrinos

There is an extension of the SM, by adding sterile neutrinos as right-chiral counterparts of the neutrinos, that is referred to as the νMSM (*neutrino Minimal Standard Model*)

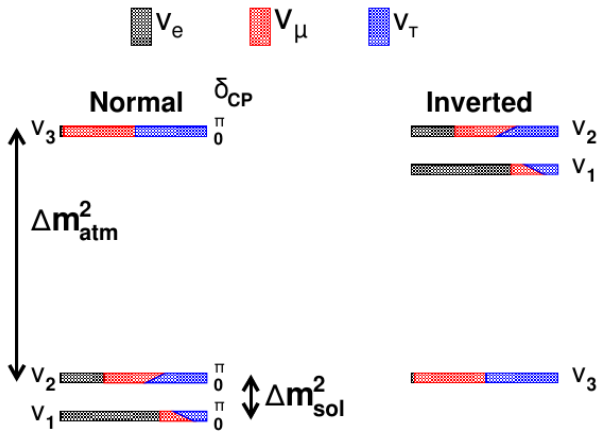

Figure 2.2: Normal and inverted mass hierarchies illustrated. The mixing of flavor and mass eigenstates, based on current measurements of the mixing angles, is indicated by coloring of the states. The flavor mixing, however, remains a function of the yet unknown CP-phase δ_{CP}. The mass differences $\Delta m^2_{\mathrm{atm}} \approx \Delta m^2_{31} \approx \Delta m^2_{32}$ and $\Delta m^2_{\mathrm{sol}} \approx \Delta m^2_{21}$ denote the atmospheric and solar mass differences [68]

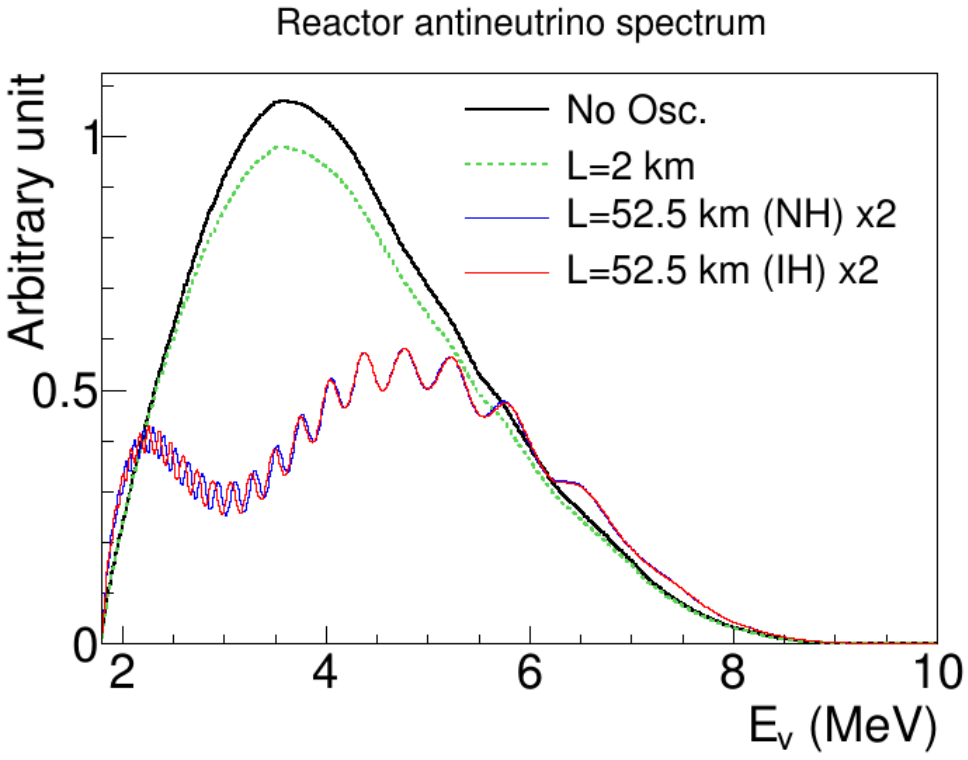

Figure 2.3: Plot of the reactor anti-neutrino spectra with normal and inverted mass hierarchy. A perfect energy resolution is assumed. Note that in order to be able to distinguish between the red and the blue spectrum, a high energy resolution is crucial [68].

[15, 16]. The number $\mathcal{N}$ of introduced sterile neutrinos can be chosen. From measurements

of neutrino oscillations, however, it is a known fact, that due to the two mass differences Δm^2_{atm} and Δm^2_{sol}, at least two of the three active neutrino dirac masses must be different from zero [11]. As a consequence, the number of sterile neutrinos must be at least two, $\mathcal{N} \geq 2$, where for a minimal choice of two sterile neutrino states, the lightest active neutrino mass becomes equal to zero [11]. The minimal number of right-chiral, sterile neutrinos to explain the baryon asymmetry of the universe, the smallness of neutrino masses and dark matter at the same time, however, is $\mathcal{N} = 3$ [11]. As this number could be higher, three seems a reasonable choice, as it remains within the three-type-ness of the standard model fermions.

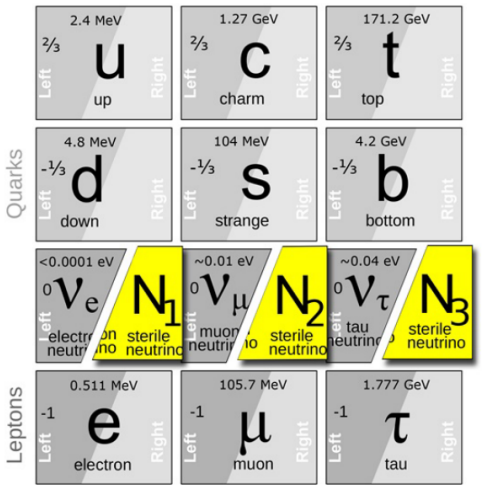

Figure 2.4: The fermions with the sterile neutrions. This shows a model containing three sterile neutrinos N_1, N_2 and N_3 which are theoretically introduced as right-chiral counterparts for the normal neutrinos ν_e, ν_μ and ν_τ, which happen to be always left-chiral[11].

2.4.4 Reactor Antineutrino Anomaly

By observing the flux of antineutrinos from nuclear reactors, especially from the fission of the Uranium and Plutonium isotopes ^{235}U, ^{238}U, ^{239}Pu and ^{241}Pu, a flux deficit with respect to expectations is measured. In [58], a ratio of observed anti-neutrinos over the number of expected antineutrinos from fissions of 0.943 ± 0.023 was observed. This shows a deviation from the expectations, including neutrino oscillation, at a confidence level of 98.6%. This takes a higher thermal power of nuclear reactors into account than what it was thought to be for earlier reactor anti-neutrino flux expectations. While this experimental hint is controversial, theories have been put forward that this could be explained with light sterile neutrinos taking part in the oscillation of the active neutrino flavors [54].

3 Drift tube detectors

Drift tube detectors are simple, yet efficient and affordable gaseous detectors for ionizing particles. The following sections give a brief introduction of drift detectors, their working principle and potential for future development.

3.1 Working principle

A drift tube consists of a conductive tube, filled with a drift gas mixture[1], in whose center a conducting wire is clamped. Between tube and wire, a high voltage is applied such that the tube's wall acts as a cathode, the wire as an anode. This results in the development of an electric field, radially symmetric and rising to high field strengths near the anode wire[2].

For charged particle detection with drift tube detectors, the energy loss via Coulomb ionization[3] of charged particles passing through matter, is used. A particle traversing the drift tube interacts with the electrons of the drift gas' atoms and molecules along its path, resulting in the ionization of these atoms and molecules (*primary ionization*). Since the process of ionization is a statistical process, a spatial distribution of ionization clusters along the particle track is observed. Depending on the transferred energy in the process of one ionization, the number of free electrons and ions in a cluster may vary. Electrons and ions begin to *drift* along the electric field lines, electrons towards the anode wire, ions towards the tube's wall. The electrons are much more mobile than the ions and on their way to the anode wire they pass a high electric field accelerating the electrons and enabling them to further ionize atoms and molecules along their path (*secondary ionization*). As the secondary electrons are accelerated in the high electric field as well, they themselves gain the ability to further ionize gas molecules, leading to a fast multiplication of charge carriers. The ions from secondary ionizations traverse a high potential difference and are the major contributors to the electric signal[4].

If the time of the charged particle traversing the tube is known by an external trigger, the time difference between trigger signal and the first electrons reaching the anode wire can be measured. The first electrons reaching the anode wire are those that drift the

[1] for gas properties required for use in drift tube detectors, see section 3.3.2
[2] see section 3.3.1 for details on the electric field
[3] see section 3.2
[4] for more information on the signal development see section 3.3.4

shortest distance, the *drift radius*. The time needed for the shortest drift is called the *drift time*. The particle track is a tangent to the drift circle, within the uncertainty of the statistical distribution of ionization clusters along the particle track. Consequently, for a particle track to be spatially reconstructed, drift time measurements of multiple drift tubes are needed. Then, a particle track can be fitted to the drift circles of all the drift tubes.

Figure 3.1 shows a schematic of ionization clusters along the track of a charged particle passing through a drift tube.

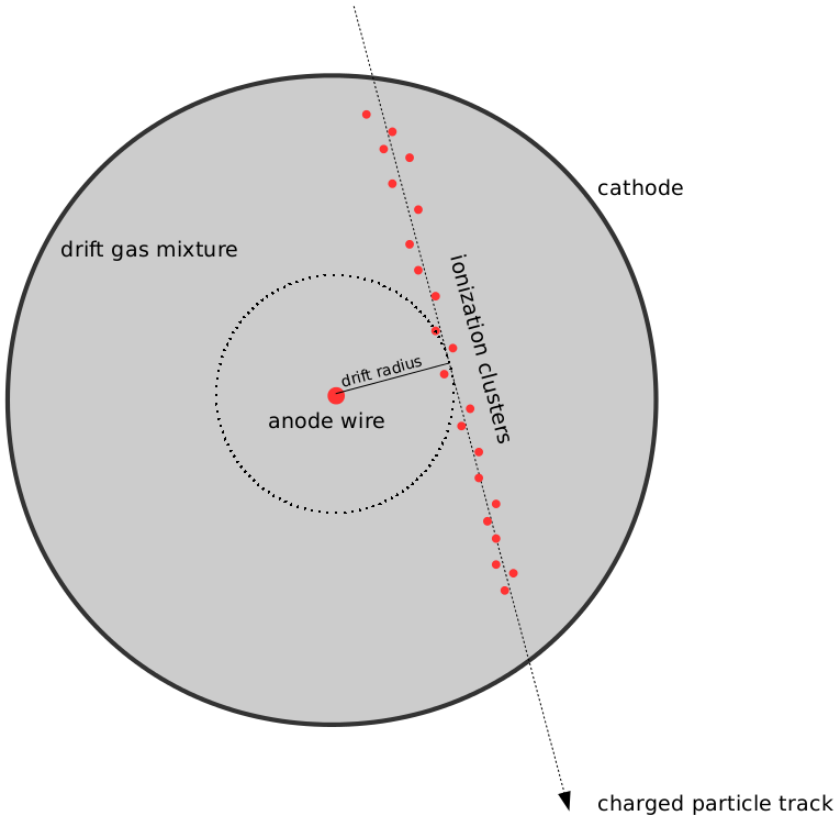

Figure 3.1: Schematic picture of a drift tube. The atoms and molecules of the drift gas mixture are ionized in a statistical process along the particle track (primary ionization). The electrons and ions now begin to drift along the radially symmetric electric field inside the drift tube. The field strength near the anode wire can provide sufficiently high acceleration of the electrons to enable them to further ionize atoms and molecules (secondary ionization). This process of multiplication of charge carriers within the tube is called gain. The less mobile ions do not gain enough energy to be able to further ionize drift gas molecules.

3.2 Ionization

Due to Coulomb interaction, charged particles can ionize atoms and molecules along their passage through matter. The energy loss per unit length of a charged particle passing through matter is described by the *Bethe-Bloch formula* [20, 21] given in equation (3.1).

$$-\frac{dE}{dx} = \frac{4\pi r_e^2 m_e c^2 N_A Z \rho z^2}{A\beta^2}\left[\ln\left(\frac{2m_e c^2\beta^2}{I(1-\beta^2)}\right) - \beta^2 - \frac{\delta(\beta)}{2}\right] \tag{3.1}$$

In equation (3.1), we use:

$r_e \hat{=}$ classical electron radius $r_e = 2,8 \cdot 10^{-15} m$
$N_A \hat{=}$ Avogadro number
$Z \hat{=}$ Proton number in absorber's nuclei
$m_e \hat{=}$ electron mass
$\rho \hat{=}$ absorber's density
$\beta \hat{=}$ relativistic velocity $\beta = \frac{v}{c}$
$A \hat{=}$ absorbers mass number
$z \hat{=}$ charge of the ionizing particle
$I \hat{=}$ absorber's mean ionization energy [eV]
$\delta(\beta) \hat{=}$ density effect shielding the nuclear potential

The ratio Z/A can be approximated as constant for many materials, the energy loss can be assumed to be dependent on two parameters, both being specific to the absorber material. Specifically, the energy loss per unit length is dependent on the absorber's density ρ and its mean ionization energy I. For the tested gas mixtures, these values can be found in table 3.1 in chapter 3.3.2. Note, that for the derivation of the Bethe-Bloch-equation, assumption need to be made that do not hold true for electrons, due to their lower mass compared to other charged particles. As the measurements performed for this thesis are performed with atmospheric muons, the above mentioned formula is a sufficient approximation.

Figure 3.2 shows a plot of the the energy loss of different particles in air computed using equation (3.1). The energy loss per unit length reaches a minimum that is roughly the same particle momentum for all particles having more mass than an electron. At momenta of about 1 GeV/c, the energy loss is minimal. Being able to detect those *minimal ionizing particles* is an important task which each detector for charged particles must fulfill.

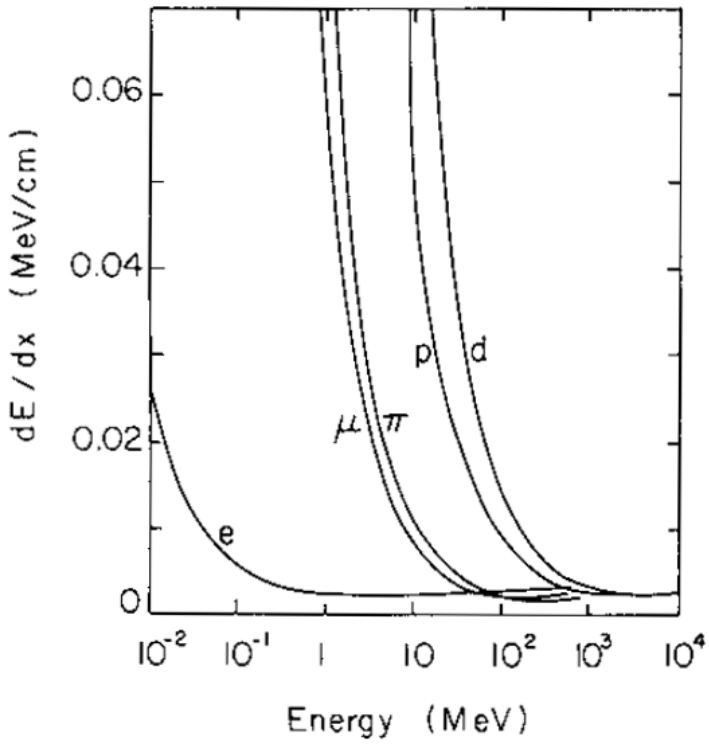

Figure 3.2: Energy loss dE per unit length dx plotted for several different particles versus their energy E. The values were computed using equation (3.1) for air as absorbing medium. At particle momenta above 1GeV/c, all particles deposit about the same energy per unit length, leading to the so called *minimal ionizing plateau*. The electrons' behavior differs from all other particles, due to the fact that electrons have a lower mass than all other displayed particles, and thus bremsstrahlung has a significant impact on the electrons' energy loss [73].

3.3 Drift of ions and electrons

In the following text, all calculations are for a drift tube of length L with an inner radius b in whose center an anode wire of radius a is clamped.

3.3.1 Electrical field inside a drift tube

Between the anode wire in the tubes center and the tube wall being the cathode, a high voltage U_{HV} is applied, which will lead to a radially symmetric electric field $\vec{E}$, as shown in the following. A more detailed discussion can be found in [53].

In order to achieve a quantitative description of the electric field inside the drift tube, one applies *Maxwell's equations*. In particular *Gauss' law*, which is shown in equations

(3.2) and (3.3), where in the latter one, *Stokes' theorem* is applied.

$$\vec{\nabla} \times \vec{E} = \frac{1}{\varepsilon\varepsilon_0}\rho \tag{3.2}$$

$$\int_V \left(\vec{\nabla} \times \vec{E}\right) dV = \oint_{\partial V} \vec{E} \cdot d\vec{A} \tag{3.3}$$

In equation (3.2), ρ denotes the charge density, which is limited to the anode wire in space. ∂V is the closure of the volume V. Using the integrated Gauss law (3.3) and using the radial symmetry, thus $\vec{E} \parallel d\vec{A} \ \forall\vec{r}$, we get:

$$\oint_{\partial V} \vec{E} \cdot d\vec{A} = \int_0^z \int_0^{2\pi} E(r) r d\varphi dz' = 2\pi E(r) r z \tag{3.4}$$

$$\int_V \left(\vec{\nabla} \times \vec{E}\right) dV = \frac{1}{\varepsilon\varepsilon_0} \int_V \rho dV = \frac{q}{\varepsilon\varepsilon_0} \tag{3.5}$$

Now using (3.3), we can write:

$$2\pi E(r) r z = \frac{q}{\varepsilon\varepsilon_0} \tag{3.6}$$

We assume a drift tube of inner radius b with an anode wire of radius a clamped in the tube's center. To enable us of neglecting edge effects, we further assume that the length L of wire and tube is much larger than the tube's inner radius, so $L \gg b$. Thus, the assumption of

$$\frac{q}{z} = \frac{dq}{dz} = const$$

can be made. Using this in (3.6), we get the electric field as shown in (3.7).

$$E(r) = \frac{1}{2\pi r \varepsilon\varepsilon_0} \frac{dq}{dz} \tag{3.7}$$

Since the electric field is a conservative field, thus can be written as the negative gradient of a potential $U(\vec{r})$, equation (3.8) holds true.

$$\int_a^b E(r) dr = \int_a^b \frac{1}{2\pi r \varepsilon\varepsilon_0} \frac{dq}{dz} = \frac{1}{2\pi\varepsilon\varepsilon_0} \ln\left(\frac{b}{a}\right) \frac{dq}{dz} = -\int_a^b \vec{\nabla} U(\vec{r}) d\vec{r} = U_{\mathrm{HV}} \tag{3.8}$$

Summarizing, we find

$$\frac{dq}{dz} = \frac{2\pi\varepsilon\varepsilon_0 U_{\mathrm{HV}}}{\ln\left(\frac{b}{a}\right)}.$$

Using this in equation (3.7), the electric field is written as shown in equation (3.9).

$$E(r) = \frac{U_{\mathrm{HV}}}{r \ln\left(\frac{b}{a}\right)} \tag{3.9}$$

3.3.2 Drift gases

Drift gases strongly influence the properties of a drift tube detector. They are compositions of two basic components: a gas that can easily be ionized, which typically holds true for noble gases, and a *quenching gas*. They must perform the tasks of a charge multiplication near the anode wire as well as a supression of photon emission. Monatomic inert gases offer a low crosssection for atomic excitation states, that do not result in ionization but in photon emission.

The detection of muons, that typically are minimal ionizing particles in high energy physics, requires a high density of primary ionizations. This density, however, is proportional to the nuclear charge Z of the inert gas, so heavy gas are preferable. The use of Radon with $Z = 86$ is not possible because of its own radioactivity. Xenon ($Z = 54$) and Krypton ($Z = 36$) are an optimal choice as drift gas detection components. However, both of those gases are expensive, thus using them in large scale drift tube detectors is not cost-efficient. Argon with a nuclear charge of $Z = 18$ offers a compromise of cost and primary ionization density. For the SHiP experiment, a high flux of γ photons in the muon magnetic spectrometer is possible. In order to suppress ionization due to those γ, a gas with lower Z has advantages as well. The photon interactions at high energies are dominated by *pair production*, for which the crosssection is proportional to Z^2. Hence, Argon as detection component seems a reasonable choice.

However, in the process of charge multiplication, radiative excitations of Argon might occur. The lowest energy excitation of Argon is at an energy of $E^*_{0,\mathrm{Ar}} = 11.6$ eV. Thus, a photon from an Argon deexcitation has enough energy to release a photo electron from the aluminum cathode[5]. As those photo electrons are multiplied near the anode wire as well, their production results in signals following the original signal, which are known as *afterpulses*. Hence, the admixture of molecular gases, that have high crosssections for the absorption of photons, that excite states with a nonradiative deexcitation through rotation or vibration, is preferable. A common choice of a such a quenching gas is CO_2. The effect of the addition of Nitrogen to the drift gas mixture is studied in this thesis.

3.3.3 Gas amplification

The gas amplification (or gas gain) G describes the process of multiplication of charge carriers due to secondary ionization. The gain of free electrons $\frac{dN}{N}$ per unit length dr can be described by the *first Townsend ionization coefficient* $\alpha_T(\frac{E}{r'}, \rho)$ [42]. The term $\frac{E}{r'}$ denotes the *reduced field strength*, ρ the gas density. The gain of free electrons then is given by equation (3.10).

$$\frac{dN}{N} = \alpha_T \left(\frac{E}{r'}, \rho \right) dr \tag{3.10}$$

[5] Aluminum has a work function of $W_{\mathrm{Al}} = 4.25$ eV

Table 3.1: Properties of the drift gases' components investigated within this thesis. A denotes the mass number of the atoms or molecules, Z their number of protons in the nucleus/nuclei. Their minimal ionization potential is given as I_0 and their mean ionization potential is denoted by I. The density ρ is given at normal conditions [73, 22].

gas	A	Z	I_0 [eV]	I [eV]	ρ [$kg\,m^{-3}$]
Ar	2	18	15.76	188	1.78
CO_2	44	22	13.81	85	1.98
N_2	28.01	14	15.5	82	1.25

The first Townsend ionization coefficient cannot be analytically derived but has to be measured for any gas mixture and field strength E. The gas gain G now can be computed by integrating equation (3.10), which results is shown in equation (3.11).

$$G = \frac{N_f}{N_0} = \exp\left(\int_{r_{\min}}^{a} \alpha_T(r)dr\right) = \exp\left(\int_{E(r_{\min})}^{E(a)} \frac{\alpha_T(E)}{dE/dr}dE\right) \tag{3.11}$$

Here, a is the anode radius and $r_{\min}$ denotes the radius where the avalanche begins. N_f is the number of free electrons reaching the anode wire and N_0 the number of free electrons at the beginning of the avalanche. Using the electric field as shown in equation (3.9), the gain can be written as:

$$G = \exp\left(\frac{U_{\mathrm{HV}}}{\ln(\frac{b}{a})}\int_{E(r_{\min})}^{E(a)} \frac{\alpha_T(E)}{E^2}dE\right) \tag{3.12}$$

Diethorn [37] proposed a parametrization of the Townsend coefficient, assuming a linear dependence of $\alpha_T(E)$. Using this parametrization, equation (3.12) can be integrated [42], which results in:

$$\ln(G) = \frac{\Delta\Phi}{\Delta V}\ln(2) = \frac{\ln(2)}{\Delta V}\frac{U_{\mathrm{HV}}}{\ln(b/a)}\ln\left(\frac{E(a)}{E(r_{\min})}\right) \tag{3.13}$$

Here, $\Delta\Phi$ is the potential difference between the anode and the radius where the avalanche begins. The difference ΔV is the potential that electrons need to pass in order to be enabled for another ionization, thus the energy $e\Delta V$ corresponds to the ionization energy of the gas [42].

3.3.4 Signal development

The electric signal on the anode wire is a result of drifting electrons and ions, that are accelerated on their path towards anode or cathode, reducing the electric field energy ε. An electric charge q drifting in an electric field $\vec{E}(r)$ reduces the energy of that field by an amount $\Delta\varepsilon$ as shown in equation (3.14).

$$\Delta\varepsilon = q \int_{r_1}^{r_2} \vec{E}(r) d\vec{r} = q(\Phi_2 - \Phi_1) \tag{3.14}$$

In (3.14), Φ_i is the electric potential at point i. Since both electrons and ions drift in the electric field, the signal is composed of two components, that of the electrons and the ions. As stated in chapter 3.1, the electrons undergo multiplication in high electric field strengths near the anode wire. The last half of charge carriers is created at about one mean free path λ_e of the electrons from the anode wire. Assuming a pair of electron and ion is produced at a distance r' from the anode wire, according to [53], the voltage difference due to the drifting electron (u^-) and due to the ion (u^+) are:

$$u^- = -\frac{-e/L}{2\pi\varepsilon_0} \int_{a+r'}^{a} \frac{1}{r} dr = \frac{-e/L}{2\pi\varepsilon_0} \ln\left(\frac{a+r'}{a}\right) \tag{3.15}$$

$$u^+ = -\frac{+e/L}{2\pi\varepsilon_0} \int_{a+r'}^{b} \frac{1}{r} dr = \frac{-e/L}{2\pi\varepsilon_0} \ln\left(\frac{b}{a+r'}\right) \tag{3.16}$$

$$u = u^+ + u^- \tag{3.17}$$

As stated in [53], the contribution of the electrons drift to the electric signal for typical values of drift tubes used is small, usually in the range of one per cent.

3.3.5 Drift time and radius

The relation of the measured drift time t_d and the radius r of the drift circle, the particle track is a tangent to, is known as the *rt-relation*. The drift circle's radius can be written as shown in equation (3.18).

$$r(t_\mathrm{d}) = \int_0^{t_d} v_d(t) dt = \int_0^{t_\mathrm{d}} \frac{dr}{dt} dt \tag{3.18}$$

Here, v_d is the drift velocity, that can be written as shown in equation (3.19).

$$v_d = \frac{dr}{dt} = \frac{dr}{dN}\frac{dN}{dt} \tag{3.19}$$

Assuming a homogenous distribution of particle tracks with respect to the tubes radius, which is true for measurements with atmospheric muons as carried out within the context of this thesis, the number dN of tracks, that pass through the tube in an interval $[r; r+dr]$ over dr is shown in (3.20).

$$\frac{dN}{dr} = \frac{N_{\text{tracks}}}{r_{\text{tube}}} \tag{3.20}$$

N_{tracks} here denotes the total number of tracks and r_{tube} the tube's radius. Using (3.20) in (3.19), the drift velocity can be written as:

$$v_d = \frac{r_{\text{tube}}}{N_{\text{tracks}}} \frac{dN}{dt}$$

Inserting this drift velocity into equation (3.18), the rt-relation is found to be as shown in equation (3.21).

$$r(t_d) = \frac{r_{\text{tube}}}{N_{\text{tracks}}} \int_0^{t_d} \frac{dN}{dt} dt \tag{3.21}$$

The distribution of drift times $\frac{dN}{dt}$ is called the *drift time spectrum*. A drift time spectrum that was measured using a test setup for the *OPERA* experiment is shown in figure 3.3.

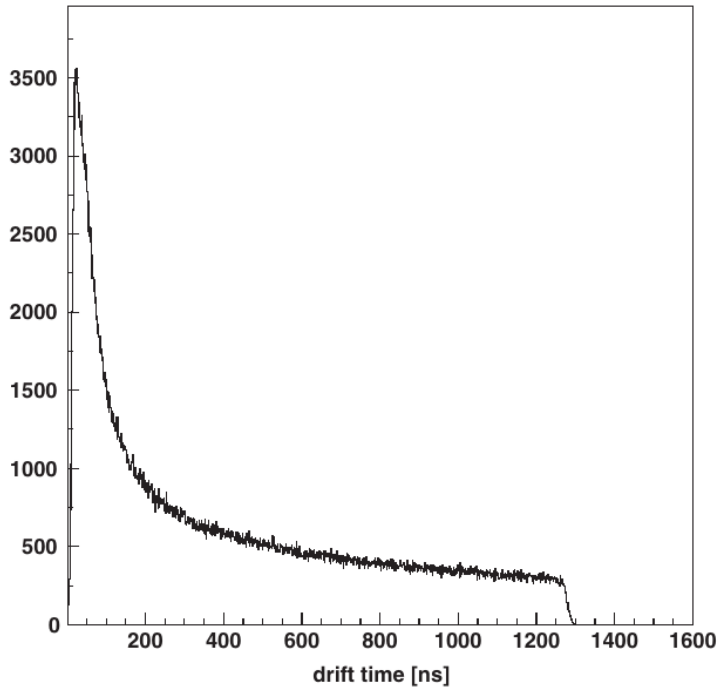

Figure 3.3: Spectrum of drift times measured for the *precision tracker* of the *OPERA* experiment. The used drift gas mixture, for which this spectrum shape is typical, is 80% Ar and 20% CO_2 [85].

Following equation (3.21), by integrating the drift time spectrum, one can compute the *rt*-relation. In order to achieve a spatial resolution not varying much with the radius of the drift circle, a *linear rt*-relation is beneficial, which results from a box-shaped drift

time spectrum. The maximum drift times originate from tracks near the cathode, a *fast* drift gas has shorter maximum drift times which allows for faster collection times.

3.4 Detection efficiency

The detection efficiency η is given by the fraction of number of detected events N_e by the drift tube over the number of triggered events N_t by the external trigger, as shown in equation 3.22

$$\eta = \frac{N_e}{N_t} \tag{3.22}$$

The single events are independent from each other and happen with low rates, so they follow a Poissonian distribution. The standard deviation σ_η on the efficiency is given by the Gaussian propagation of errors (3.23), which describes the error of a quantity G, where G itself is a function of multiple quantities, that are associated with error themselves:

$$\sigma_G = \sqrt{\sum_i \left(\frac{\partial G}{\partial x_i}\sigma_{x_i}\right)^2} \tag{3.23}$$

Hence, for the efficiency, the deviation of η is shown in equation (3.24).

$$\sigma_\eta = \sqrt{\frac{\eta(1-\eta)}{N_t}} \tag{3.24}$$

3.5 Track reconstruction

From the measurement of the drift time, the radius at which a charged particle passed the drift tube can be calculated. Thus, measuring the drift time of a single drift tube only provides a drift circle, which the particle track is a tangent to. When the drift circles of multiple layers of drift tubes are combined, a particle track can be *fitted* to these drift circles, as shown in figure 3.4. The reconstructed track, however, is a two dimensional track since no information is present about the location along the tube axis, where the particle passed. As the electric signal propagates on the sense wire with a finite speed, the time differences between the signal being measured at each side of the tube can be done, which was tested for the *OPERA* drift tubes and resulted in a resolution along the tube axis of $\sigma_L = 49.2$ cm [24]. This resolution along the tube axis comes at the cost of a second set of readout electronics needed for each tube. The spatial resolution achieved this way usually does not justify the additional cost. For certain purposes in high energy physics, however, a three dimensional track reconstruction with much higher accuracy is required. This can be achieved by tilting several layers of drift tubes by a *stereo angle* against each other. The two dimensional tracks reconstructed by each layer of tilted drift tubes can then be combined to reconstruct the three dimensional particle track.

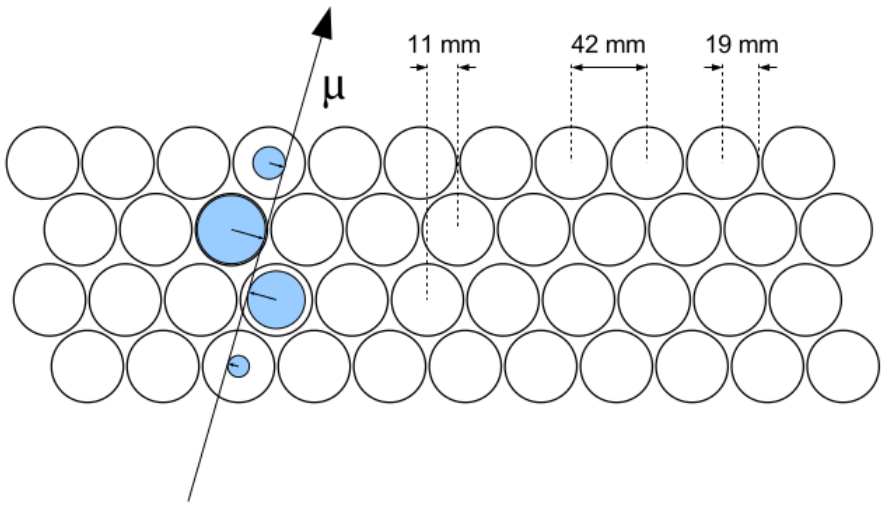

Figure 3.4: A muon track fitted to the drift circles of four drift tubes hit. The drift tube setup is from one wall of the precision tracker of the *OPERA* experiment [55].

3.6 Effects influencing detector performance

Several physical and chemical effects influence the performance of a drift tube detector. As there are many such factors, not every contribution is discussed here.

3.6.1 Drift gas mixture pressure

The spatial resolution of the drift circle depends on the pressure of the drift gas mixture. According to [22], a change in pressure by a factor k results in a higher spatial resolution of a factor $1/\sqrt{k}$. However, drift tube detectors with a large volume, such as the drift tubes for the muon magnetic spectrometer for the SHiP experiment, might not be operated at higher pressures for security reasons. Consequently, the gas pressure must be chosen as a compromise of safe detector operation and the necessary spatial resolution.

3.6.2 Uncertainties in time measurements

As shown in equation (3.21) and described in chapter 3.5, the spatial resolution of a drift tube detector largely depends on the accuracy of drift time measurements. Thus, a high resolution in time measurements is needed in order to operate a drift tube detector with high accuracy. This effect is dominant near the anode wire as shown in [84].

3.6.3 Diffusion

The atoms and molecules in a gas have a thermal energy, the average value being $\varepsilon_T = 3/2 k_B T$ and following Maxwell's probability distribution shown in equation (3.25) [73].

$$F(\varepsilon) = C\sqrt{\varepsilon} e^{-\frac{\varepsilon}{k_B T}} \tag{3.25}$$

Charges, produced by ionization undergo multiple collisions in the gas, broadening the energy distribution and diffusing away from their point of origin (neglecting the drift along the field lines). Due to diffusion, the location distribution of the charges after a time t follows a Gaussian distribution as shown in (3.26).

$$\frac{dN}{N} = \frac{1}{\sqrt{4\pi Dt}} e^{-(x^2/4Dt)} dx \tag{3.26}$$

Here, $\frac{dN}{N}$ is the fraction of charges that can be found a distance x from its origin and D is the *diffusion coefficient*. When taking the drift along the electric field into account, the diffusion coefficient is a function of the electric field strength. As a broadened energy distribution broadens the distribution of their arrival times as well, a high diffusion coefficient results in a lower spatial resolution [73].

3.6.4 Aging

The process of aging describes chemical changes in the material, mainly of the sense wire. Detailed examinations of the sense wire aging were performed for the *transition radiation tracker (TRT)* [31] for the ATLAS experiment [17], described in [9]. Additional background information can be found in [22]. As the detector, in particular the sense wire, ages, chemical changes in the sense wire material, especially deposits of metals or oxidation of the sense wire material can occur as the sense wire accumulates charge during its operation. Those changes are more likely to happen in environments with admixtures of water or oxygen in the tube, which accelerates the aging process. In [9], studies on chemical and physical changes of the sense wire were performed using captures from a *Scanning electron microscope (SEM)*, accompanied by *energy dispersive X-Ray (EDX)* analysis of material defects. Figure 3.5 shows a photo of a gold-plated tungsten wire that accumulated a charge of 0.5 C/cm in an environment with the admixture of 1.5% of O_2 and 1.2% of H_2O. An examination of this defect using EDX showed the presence of tungsten and oxygen in the material defect, significantly changing the electric field near that location on the sense wire.

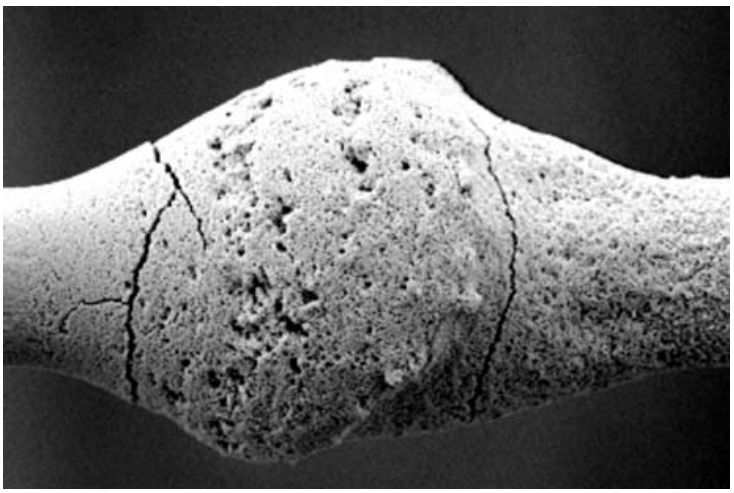

Figure 3.5: Photo from a scanning electron microscope of a gold-plated tungsten wire for the aging studies for the ATLAS transition radiation tracker (*TRT*). The aging was accelerated for testing purposes by adding 1.5% of O_2 and 1.2% of H_2O. The accumulated charge per unit length is approximately 0.5 C/cm. An energy dispersive X-ray analysis has shown the presence of WO in the bulb [9].

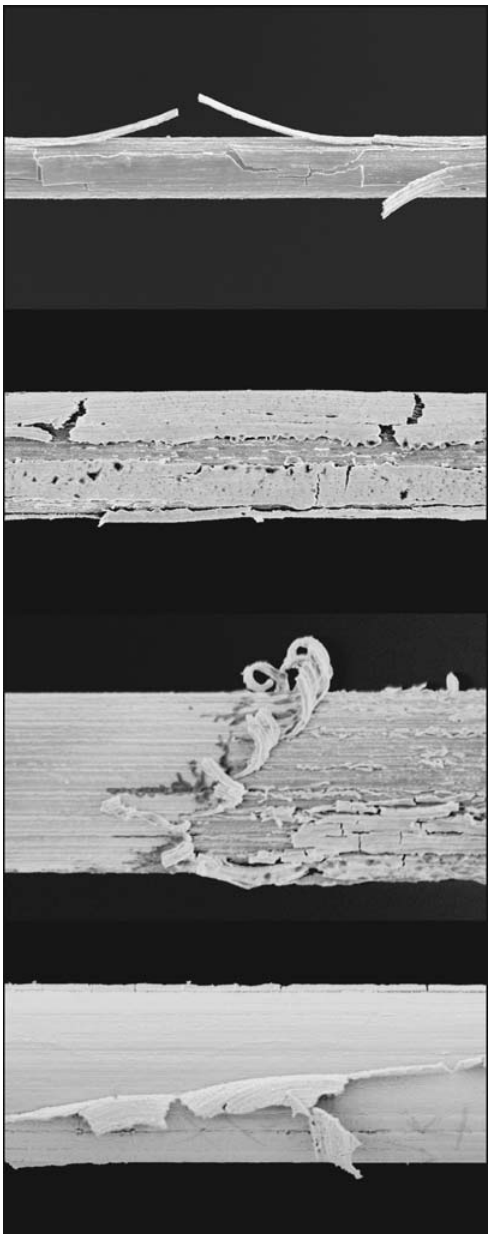

Figure 3.6: Damage on the gold plating of the sense wire after $2-6$ C/cm of accumulated charge. No damage was observed when the amount of water in the drift gas mixture was lower than 0.1% [9].

3.7 Experiments using drift tube detectors

As seen above, drift tube detectors are reliable, cheap detectors applicable for the instrumentation of large volumina. As drift tube detectors are able to measure minimally ionizing particles with a reasonable spatial resolution and operate in magnetic fields, they are commonly used as muon trackers in high energy physics. Muons are minimally ionizing at relatively low energy. In electromagnetic and hadronic calorimeters, they usually cannot be stopped, enabling them to escape the detector. In a symmetric energy collider experiment, in order to achieve an event reconstruction with the major particle masses and energies, one needs to reconstruct all transverse momenta. Charged particles leaving signals in the electromagnetic and hadronic calorimeters, but not producing showers that dump large amounts of energy in those calorimeters, can be assumed to be muons. They are then measured in the outermost detector parts, the muon trackers. Through bending their tracks in magnetic fields, one can reconstruct their transverse momenta, so that their contribution to the balance of transverse momenta can be accounted for. Neutrinos however cannot be reconstructed and can, in the end, only be recognized as missing transverse momentum.

Some recent experiments using drift tube detectors are *OPERA [49, 36] and ATLAS [17]*, which are discussed below. Note that drift tube detectors are commonly used in many experiments, that can not be discussed here.

OPERA The now decommissioned *OPERA* experiment was an experiment for neutrino oscillations, searching for the appearance of ν_τ in the ν_μ beam CNGS[6]. It successfully proved the appearance of τ-neutrinos in a μ-neutrino beam [6]. OPERA used a target tracker of bricks made of lead interleaved with photo emulsion. Most of the neutrinos in the CNGS beam reach the underground laboratory LNGS[7] as muon neutrinos, interacting in the lead with a muon in the final state. Tau neutrinos, however, interact, producing a τ lepton, which decays further with a muon and two neutrinos in the final state. As the neutrinos carry momentum, the muon travels at different direction than the τ, thus the track will show a *kink* at the location of the decay vertex. The decay length of the τ-lepton is in the range of a μm, thus a high spatial resolution in the target tracker is needed.

A reconstruction of the charge sign and the momentum of the muons is of vital importance in order to clearly identify an event originated in an interaction of a ν_τ from the neutrino beam. For the momentum and charge reconstruction, drift tubes were used. The drift tubes were 8 m long and filled with a drift gas mixture of 80% Ar and 20% CO_2. They were grouped to walls of eight modules, each containing 48 drift tubes in four layers. The drift tubes at the OPERA experiment, being a low-rate experiment, had an

[6]CERN neutrinos to Gran Sasso
[7]Laboratori Nazionali del Gran Sasso

expected trigger rate of 1.2 Hz per wall [42]. Due to the low expected rate, no admixtures of gases were made, that lead to higher drift velocities, thus reducing the maximum drift time and dead time, the maximum drift time of about 1300 ns was considered sufficient. An upgrade of the drift tubes of the OPERA experiment is planned to be used for the SHiP experiment, where a muon flux of 4 kHz/m^2 is expected, thus faster collection times are needed.

ATLAS The ATLAS[8] experiment, being one of the experiments situated at the *Large Hadron Collider (LHC)*, uses drift tubes as muon spectrometer. Each tube has a diameter of 30 mm and is operated with a drift gas mixture of 93% Argon and 7% CO_2 at a pressure of 3 bar. More than 350,000 drift tubes seperated into 1,200 modules are placed in a ring shape around the hadronic calorimeter. As the hadronic calorimeter is designed to stop hadrons, only muons are expected to pass through the muon spectrometer. The ATLAS experiment was designed to search for the Higgs boson, which has decay channels with muons in the final state. Thus, a reconstruction of the muon tracks and momenta is mandatory. The muon spectrometer of ATLAS operates in a strong, toroidal magnetic field, enabling the spectrometer to reconstruct transverse momenta with a resolution of $2-3$ % for muon transverse momenta up to $p_T = 100$ GeV. At $p_T = 1$ TeV, the resolution is about 10%. The spatial resolution of the ATLAS muon spectrometer is about 50μm [77]. For the luminosity upgrade of the *LHC*, faster collection times of the ATLAS muon spectrometer were needed. For that purpose studies with linear and fast drift gas mixtures were performed in [79], also motivating the research performed within the context of this thesis.

[8] acronym for A Toroidal Lhc ApparatuS

4 The SHiP experiment

The *Search for Hidden Particles (SHiP)* experiment is a newly proposed, beam dump experiment which is to be built using beamtime from the *Super Proton Synchrotron (SPS)* at *CERN*[1]. Among other tasks, it is a preaccelerator for the *Large Hardon Collider (LHC)*. SHiP offers the opportunity, to explore physics beyond the standard model[2] without the need for new accelerators. A special focus lies on neutrino physics, especially the question, if normal neutrinos might be supplemented with heavy sterile neutrinos[3], which are proposed to be of a much higher mass than the active neutrinos by some models. The following text will introduce the reader to how SHiP can explore BSM physics in comparison with LHC or future collider experiments. In addition, SHiP will offer the first ever ability to directly observe the $\bar{\nu}_\tau$.

4.1 Physical motivation

The discovery of the *Higgs Boson* by the LHC experiments *ATLAS* [1] and *CMS* [28] in 2012, led to the situation that all particles, that were proposed by the standard model of particle physics, were discovered. The small, non-zero neutrino masses as well as cosmological phenomena such as the baryon asymmetry of the universe (BAU) and the existence of dark matter can not be explained by the standard model. Therefore, in order to develop a more complete theoretical description of nature, we need to explore physics beyond the standard model. Many BSM theories propose the existence of yet undiscovered particles.

The properties of the SHiP detector in comparison with other experiments, dedicated to the search for sterile neutrinos are shown in table 4.1. For details on the PS191 experiment, see [18, 19, 82]. Details on NuTeV can be found in [39] and for the CHARM experiment, see [81].

4.1.1 Intensity frontier

There are two ways of searching for yet undiscovered particles. They might either have masses higher than those accessible with nowadays collider experiments. These particles

[1] Conseile Eurepéen pour la Recherche Nucléaire (french) - European Organization for Nuclear Research
[2] in the following text denoted by *BSM* (beyond standard model) physics
[3] see section 2.4.3 for more information on sterile neutrinos

Table 4.1: Experiments dedicated to search for HNLs in comparison [30]

Experiment	PS191	NuTeV	CHARM	SHiP
Proton energy (GeV)	19.2	800	400	400
Protons on target ($\cdot 10^{19}$)	8.86	0.25	0.24	20
Decay volume (m^3)	360	1100	315	1780
Decay volume pressure (bar)	1 (He)	1 (He)	1 (air)	10^{-6} (air)
Distance to target (m)	128	1400	480	80-90
Off beam axis (mrad)	40	0	0	0

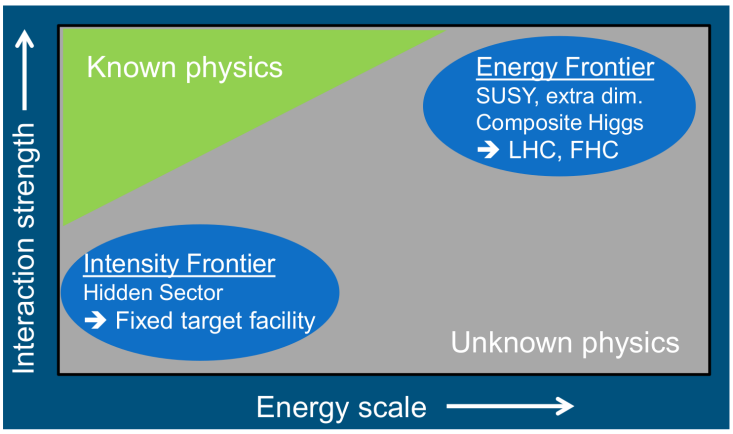

Figure 4.1: Illustration of ways to explore physics beyond the Standard Model. In the intensity frontier, small interaction strengths can be explored, included the *Hidden Sector*. High energy scales ca be explored with future collider experiments at higher energies, including for example supersymmetric (SUSY) models [11].

may be discovered with future generations of particle accelerators and colliders, hidden particles, that can be found with higher energies are called to be in the *energy frontier*. The SHiP experiment, however, using the 400 GeV, high intensity proton beam from the SPS utilizes another approach. It will search for particles at lower masses but with small couplings, that need a high intensity to be discovered, what is called the *intensity frontier* [30]. A sketch of how to explore physics beyond the standard model is shown in figure 4.1.

4.1.2 ν_τ physics

Production of tau neutrinos The proton beam of 400 GeV is stopped in the proton target[4], where τ neutrinos are produced in two major ways. In primary proton interactions, due to the target material, $D_s^{\pm}$ mesons, containing a charm quark, are produced in

[4]described in chapter 4.3.1

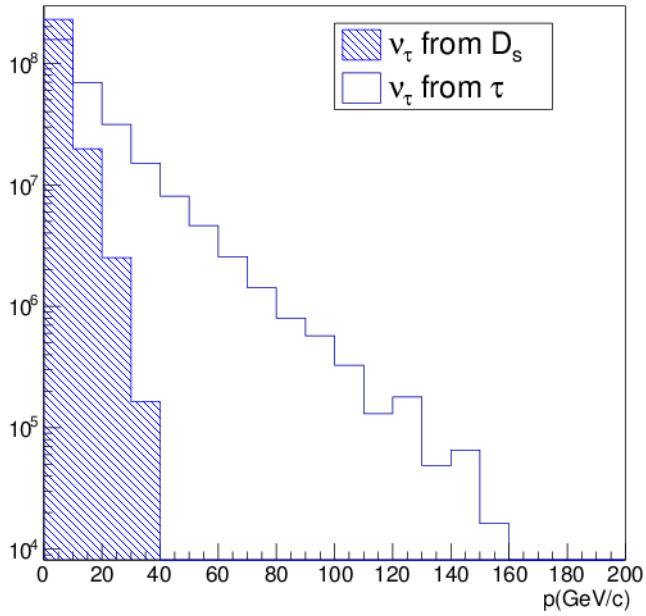

Figure 4.2: Estimated momentum distribution of ν_τ produced either in the decay of D_s mesons (shaded) or the decay of τ leptons. The distribution is the same for $\bar{\nu}_\tau$ [30].

an equal amount [30]. The ratio of D_s meson production is:

$$f_{D_s} = (7.7 \pm 0.6^{+0.5}_{-0.4})\%$$

as shown in [5]. The leptonic decay of the $D_s^\pm$ mesons can happen to τ leptons accompanied by τ neutrinos with a branching ratio of [64]:

$$Br(D_s \to \tau) = (5.54 \pm 0.24)\%$$

The second process producing τ neutrinos is the decay of the before mentioned τ leptons. This results in a number of produced τ neutrinos for $2 \cdot 10^{20}$ protons on target of $N_{\nu_\tau + \bar{\nu}_\tau} = 5.7 \cdot 10^{15}$ [30]. As a result of the different kinematics involved in these two processes, the expected spectra of ν_τ and $\bar{\nu}_\tau$ differ, being softer for neutrinos from meson decays [30]. An estimated momentum distribution of ν_τ produced in decays of τ and D_s is shown in figure 4.2.

Electron and muon neutrinos, however, can be produced by many decays. Especially pions and kaons that are produced as secondary particles from proton interactions, do often decay with electron and muon neutrinos in the final state. A simulation of the proton target and hadron stopper using Geant4 has been performed. It provides expected neutrino spectra produced in the proton target and surviving the hadron stopper as shown in figure 4.3. In those spectra, a cut of 0.5 GeV is applied, since neutrinos of energies

lower than that have a smaller cross section and a wide angular distribution, resulting in a neglegible contribution [30].

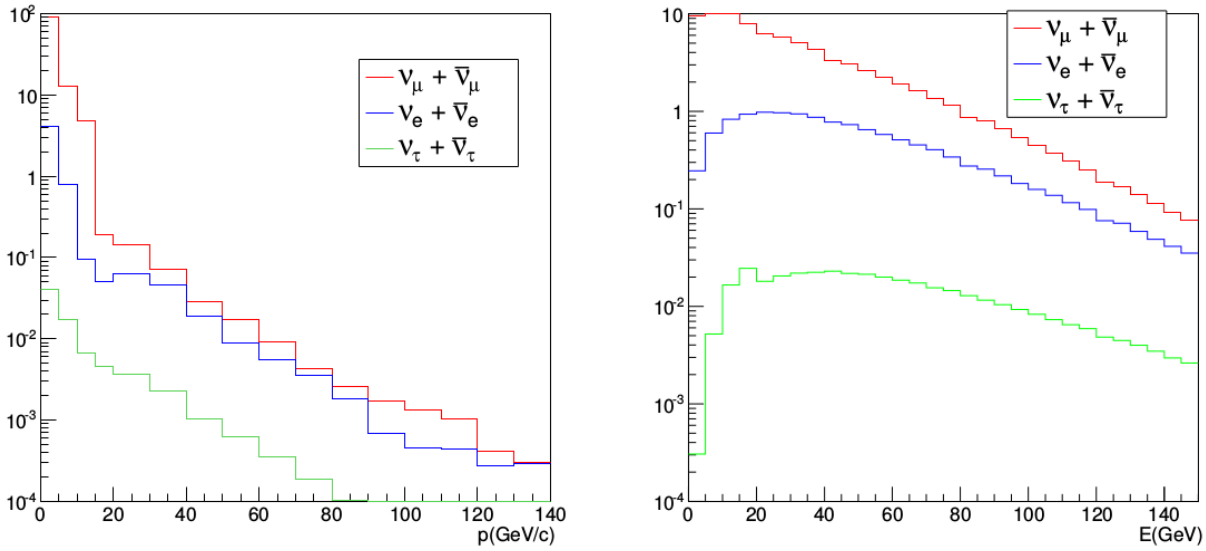

Figure 4.3: Simulated spectra of the produced neutrinos in the proton target (left) and neutrinos reaching the neutrino detector (right). The total neutrino number is normalized to 100 and a cut of 0.5 GeV/c is applied for electron and muon neutrinos as lower energy neutrinos have a neglegible interaction cross section and a wide angular distribution [30].

First ever direct observation of the $\bar{\nu}_\tau$ As the *DONuT* experiment at Fermilab was not able to distinguish between neutrino and antineutrino, they were just able to find the ν_τ [52]. The SHiP experiment, however, due to its high spatial resolution in its target tracker as well as its ability to measure the charge sign of the particles in the final state, will offer the first ever ability to directly observe the anti tau neutrino $\bar{\nu}_\tau$.

Structure functions of tau neutrinos The differential cross section $\frac{d^2\sigma^{\nu(\bar{\nu})}}{dxdy}$ for CC interactions of the ν_τ and $\bar{\nu}_\tau$ is given by equation (4.1) [30].

$$\frac{d^2\sigma^{\nu(\bar{\nu})}}{dxdy} = \frac{G_F^2 M E_\nu}{\pi(1+Q^2/M_W^2)}\left(\left(y^2x + \frac{m_\tau^2 y}{2E_\nu M}\right)F_1 + \left(\left(1 - \frac{m_\tau^2}{4E_\nu M}\right) - \left(1 + \frac{Mx}{2E_\nu}\right)\right)F_2 \pm \left(xy\left(1-\frac{y}{2}\right) - \frac{m_\tau^2 y}{4E_\nu M}\right)F_3 + \frac{m_\tau^2(m_\tau^2+Q^2)}{4E_\nu^2 M^2 x}F_4 - \frac{m_\tau^2}{E_\nu M}F_5\right) \tag{4.1}$$

In equation (4.1), the differential cross section is divided to a set of five structure functions F_1 to F_5. The variables x, y, Q are related as $Q^2 = 2M_N E_\nu xy$. They represent the common set of kinematic variables of deep inelastic scattering (*DIS*). While the terms corresponding to the structure functions F_4 and F_5 can be neglected in case of muon neutrino interactions [10], they do indeed contribute to the differential cross section of

τ neutrinos due to the higher mass of the τ lepton. The value of F_4 was calculated to be about 1% of F_5 in [70] at NLO. Five years of data acquisition will enable SHiP to be sensitive to the structure functions F_4 and F_5 and test the hypothesis $F_4 = F_5 = 0$. This would result in a higher cross section for charged current deep inelastic scattering (*CC DIS*) than expected following the standard model with values that differ from zero. Figure 4.4 shows a plot of the expected cross sections of CC DIS interactions for ν_τ and $\bar{\nu}_\tau$ as predicted by the SM and the hypothesis $F_4 = F_5 = 0$. The difference is larger for lower energies, becoming neglegible at higher energy. Evidence for non-zero values of F_4 and F_5 can be achieved with a significance of 3σ requiring $\frac{\sigma_{\text{SM}}}{\sigma_{\text{zero-hypothesis}}} \equiv r > 1.6$, which is satisfied for $E_{\bar{\nu}_\tau} < 38$ GeV. At this energy range, the observation of $300\bar{\nu}_\tau$ interactions is expected [30].

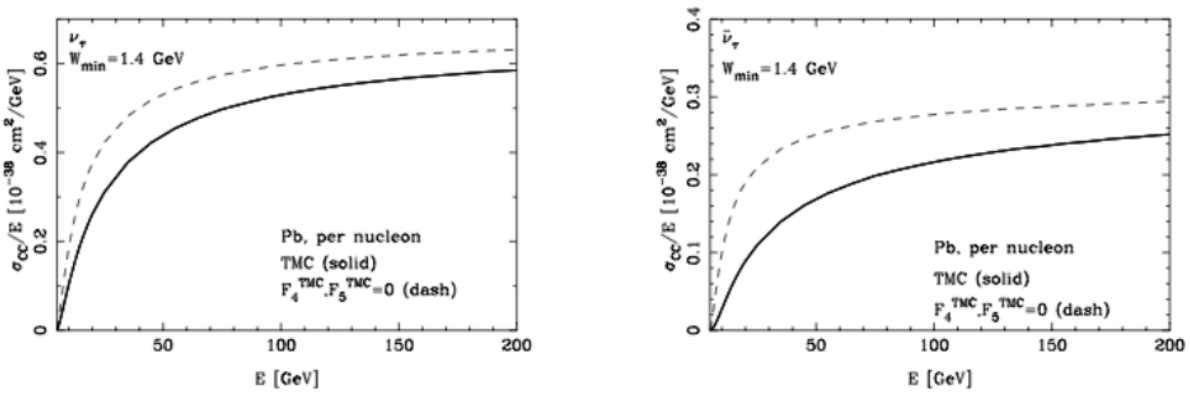

Figure 4.4: Expected cross sections for charged current deep inelastic scattering of ν_τ (left) and $\bar{\nu}_\tau$ (right). The solid graph shows the cross section as predicted by the standard model, the dashed graph the hypothesis $F_4 = F_5 = 0$ [30, 70].

4.1.3 Hidden sector portals

The SM fails to explain several phenomena, that are observed in particle physics, astrophysics and cosmology. BSM theories exist, that can explain some of those phenomena but they require the existence of yet undiscovered particles. These undiscovered particles can be grouped into three types of particles, that are coupled to SM particles via *renormalizable* interactions with small, dimensionless coupling constants, that are called *portals*. All those portals have a mass scale, that depends on the mass dimension of the singlet operators of the SM [11].

Vector portal: Coupling via the vector portal ϵ to the SM hypercharge field $F_Y^{\mu\nu}$, new particles are Abelian fields $A'_{\mu\nu}$ with a field strength $F'_{\mu\nu}$. The Lagrangian for vector portal interactions is:

$$\mathcal{L}_{\text{Vector portal}} = \epsilon F'_{\mu\nu} F_Y^{\mu\nu}$$

Thus, the new vector particles couple to photons and Z bosons. The mass dimension is in the order of $\mathcal{O}(\mathrm{GeV}^2)$.

Scalar portal: New, neutral singlet scalar S_i couple to the square of the Higgs field $|\Phi|^2$ via two couplings λ_i and g_i, in this case dimensionful, with the Lagrangian:

$$\mathcal{L}_{\text{Scalar portal}} = (\lambda_i S_i^2 + g_i S_i)(\Phi^\dagger \Phi)$$

The scalar portal has a mass scale of $\mathcal{O}(\mathrm{GeV}^2)$ as well.

Neutrino portal: The introduction of new, neutral singlet fermions N_I (sterile neutrinos, HNLs in the SHiP context)[5] coupling to the singlet operators $(L_\alpha \tilde{\Phi})$ lead to a Lagrangian:

$$\mathcal{L}_{\text{Neutrino portal}} = F_{\alpha I}(L_\alpha \tilde{\Phi}) N_I$$

L_α is one of the lepton doublets in $SU(2)$ ($\alpha \in \{e, \mu, \tau\}$), Φ is the Higgs doublet and $F_{\alpha I}$ the dimensionless *Yukawa coupling*. It has a mass scale of $\mathcal{O}(\mathrm{GeV}^{\frac{5}{2}})$.

For a detailed description of those portals, see [11]. In the context of this thesis, only the neutrino portal, especially how it can be accessed by the SHiP experiment, is further discussed in chapter 4.1.4.

4.1.4 Heavy neutral leptons

Following the assumption, that heavy sterile neutrinos (in the context of the SHiP experiment often referred to as HNLs (*Heavy Neutral Leptons*) exist, they can be produced instead of an active neutrino wherever kinematically possible. The production of a sterile neutrino is supressed with a factor of θ^2 with respect to the production of an active neutrino[6] [11].

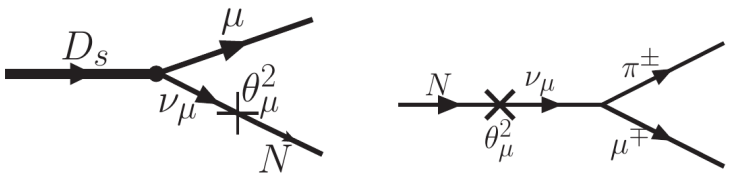

Figure 4.5: Production and decay of the sterile neutrino N_I [11].

Many decay channels of HNLs end up with pions and muons in the final state, which can be mimicked, mainly by decaying K_L^0, that do have the ability to enter the hidden sector decay volume undetected and mimic HNL decays in there. For a more detailed

[5] discussed in chapter 2.3.2
[6] see chapter 2.3.2 for details

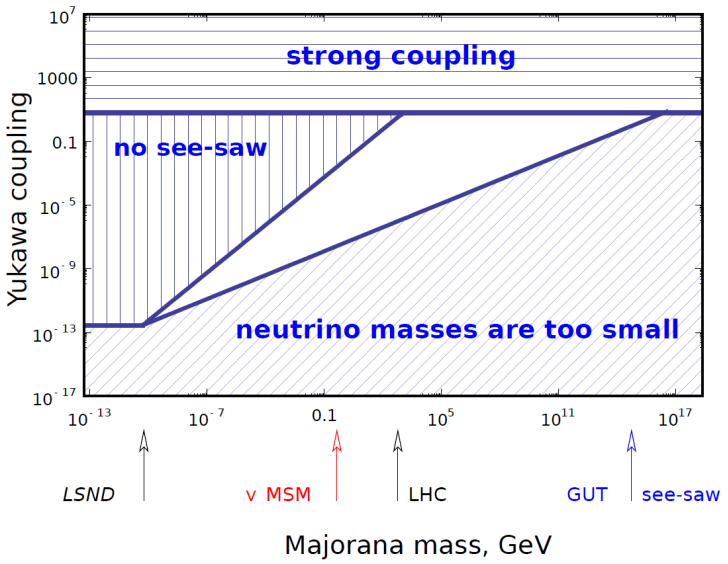

Figure 4.6: Explorable region of Yukawa couplings and Majorana masses of HNLs for see-saw models. The shaded regions are excluded due to different reasons. Too strong Yukawa couplings are excluded because with such strong couplings, HNLs must have been already discovered, other areas can be excluded as they would either not allow for the seesaw mechanism or would agree with existing constrains on active neutrino masses. Possible combinations of Yukawa couplings and Majorana masses for HNLs to exist are to be explored in the unshaded region [2].

description of background sources in the hidden sector decay volume are, see [30]. To identify a hidden particle decay, a track and momentum reconstruction of the daughter particles of the decay is needed. Additionally, veto tagging is crucial due to the low number of expected events. For a more detailed look at the detectors, performing this task, see chapter 4.3.5.

4.2 Site

The SHiP experiment is planned with minimal modifications to existing beam transfer and extraction of the SPS required. At its planned location, the SHiP facility can share the TT20 beam transfer line with other experiments at the CERN north area [30]. The existing beam transfer line allows for beam extraction with a spill of $4 \cdot 10^{13}$ protons over 1.2 seconds [30].

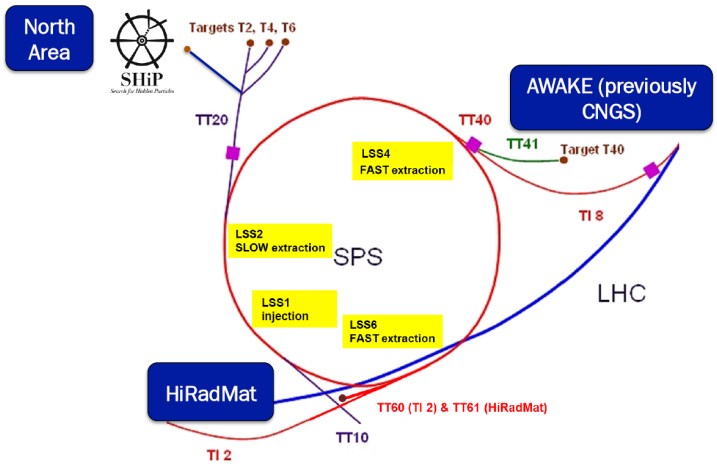

Figure 4.7: Planned SHiP site at the north area of CERN [30].

4.3 Detector layout

In the following passages, a short introduction of the major detector components will be given. Within the context of this thesis, there will be a focus on the *Muon Magnetic Spectrometer*, since the experimental results presented within this thesis are to be seen with the needed properties of this very detector component. All the following sections are based on the *SHiP technical proposal* [30] and the *SHiP physics case* [11].

4.3.1 Proton target

The proton target is designed to maximize the production of heavy mesons and minimize the production of muons and neutrinos. In order to fulfill this task, it must be made of a material with a short nuclear interaction length λ and big enough to contain the full proton shower, so absorbing all the beam energy. The high intensity, SPS proton beam with an energy of 400 GeV has an average beam power of 350 kW with a peak power of one proton *spill* of 2.56 MW. Since the flight of pions and kaons resulting from the proton interactions is to be minimized, the target must be designed with a minimal amount of space used for cooling channels. Due to the high beam power, the design of the proton target is a challenging task. The target performance required for SHiP can be aqcuired with a hybrid target made of *titanium-zirconium doped molybdenum* (TZM) alloy for the first 58 cm (4λ) and another 58 cm of pure tungsten (6λ) following downstream the TZM target. The target blocks are water cooled through 16 cooling slits, each 5 mm thick. The cooling slits' positions are optimized to achieve a uniform energy deposition distribution in the target, the maximum power density in the target is computed to be about 850 J/cm^3/spill [30]. Figure 4.9 shows a longitudinal cross cut through the proton target with the target dimensions.

The energy deposition density in the target for one spill of $4 \cdot 10^{13}$ protons on target is

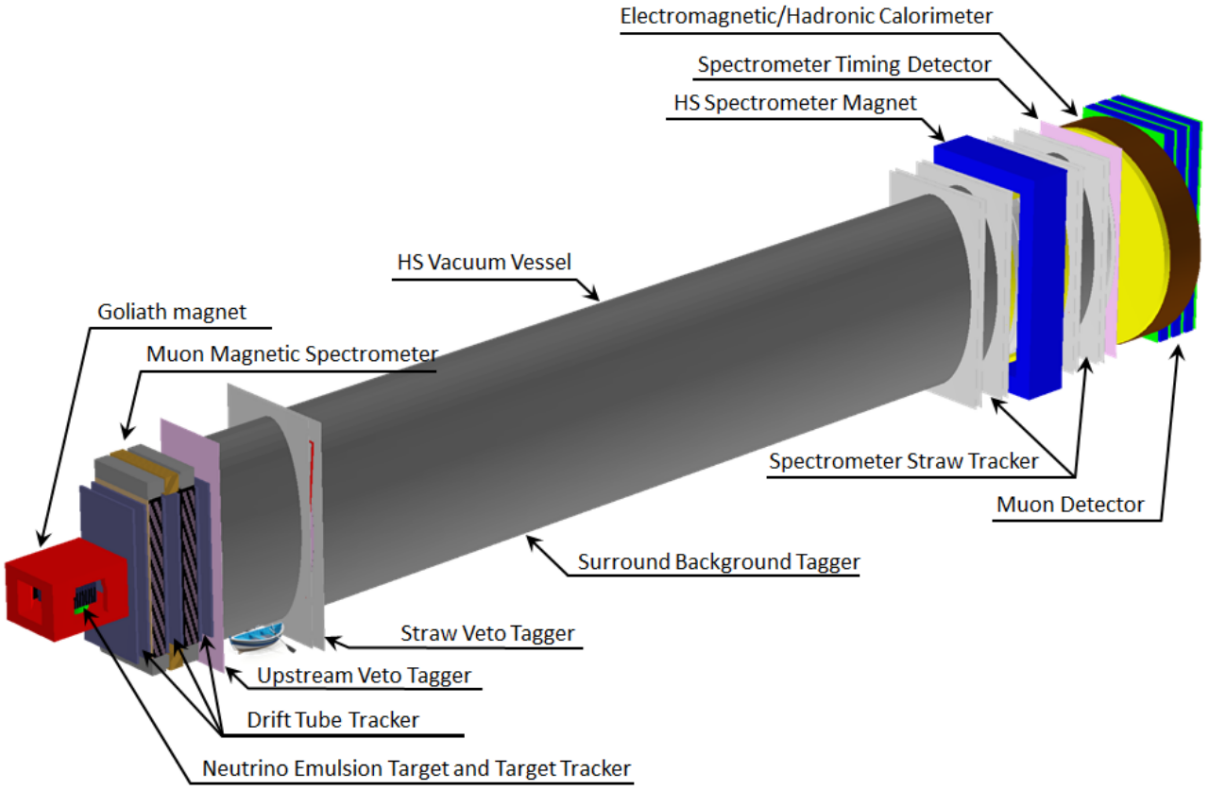

Figure 4.8: Conceptional overview of full the SHiP detector [30].

shown in figure 4.10.

The proton target is embedded in a water cooled cast iron bunker, which itself is set up in a target complex and designed to remote handable. Downstream the target, a proximity shielding of five meters thickness is set up, that is to absorb secondary hadrons and non-interacting protons escaping the target, thus reducing the irradiation of the muon shielding[7]

4.3.2 Muon shielding

Even though the proton target is designed to minimize the primary production of neutrinos and muons, a muon production rate of $5 \cdot 10^9$ muons per spill is expected. The muons, however, must not enter the hidden sector decay volume, and therefore must be bent away. Additionaly, the transverse size of the HS detector must be small enough in order to reduce background effects. Both, active and passive muon shields are under investigation. In both cases, the design heavily depends on the muon spectrum, that has been simulated [30]. The hidden sector detector decay volume design foresees an aperture of 5 m, muons must be bent beyond this aperture on a path of 48 m along the beam line.

For a solution with active shielding, a total field of $B_y = 40$ Tm is needed in order to

[7] see section 4.3.2 for more information.

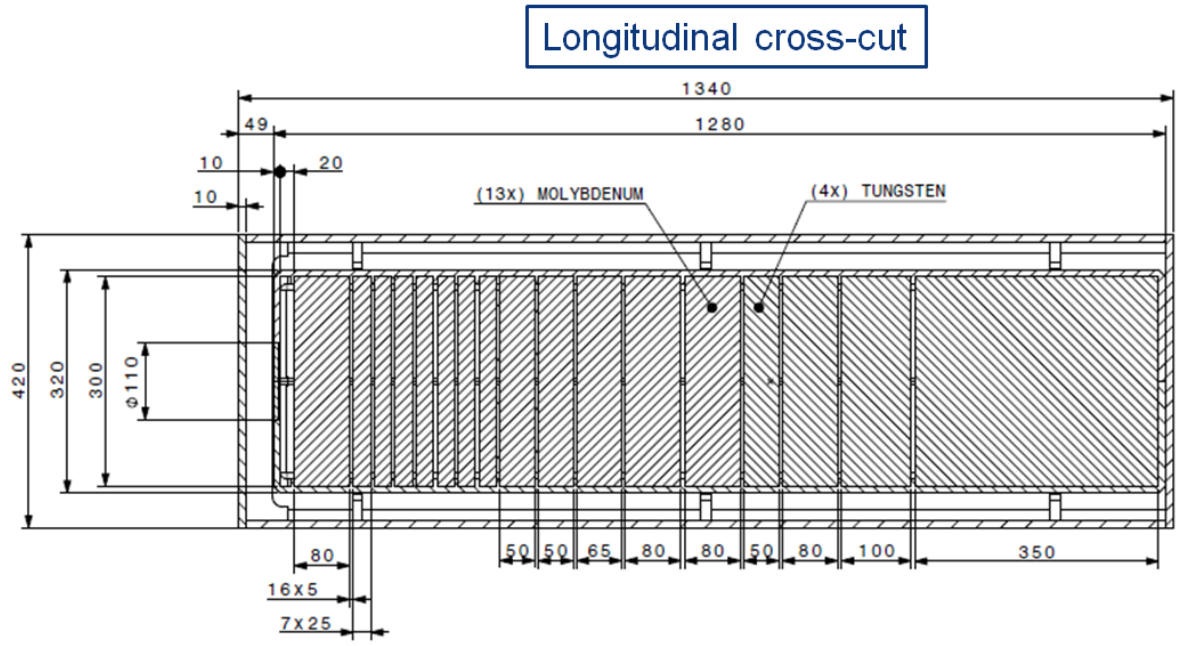

Figure 4.9: Sketch of the proton target, stopping the spill of 400 GeV, SPS accelerated protons. The areas hatched from the lower left to the upper right represent titanium-zirconium doped molybdenum (TZM) target blocks. Hatched from the upper left to the lower right side areas show the pure tungsten target. The slits within the target show the water cooling slits. Their position is optimized so that the energy deposition density is uniformly distributed [30].

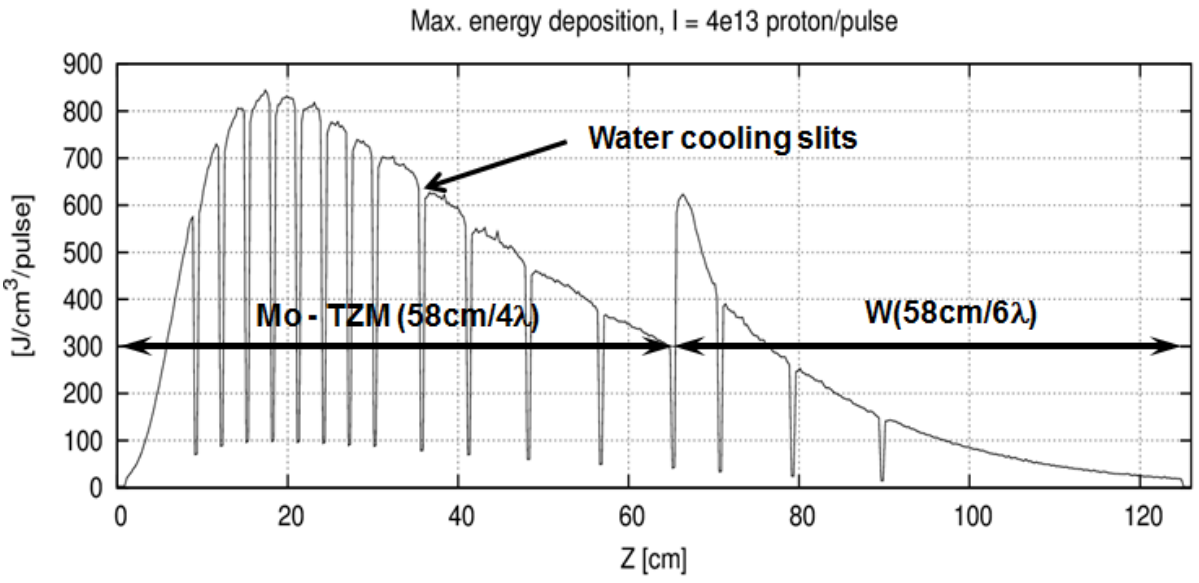

Figure 4.10: Plot of the maximum energy deposition per cm^3 in the proton target. The hadronic interaction lengths λ are shown in the plot. The local minima are the positions of the water cooling channels, where less energy is deposited due to waters lower density [30].

bend muons with an energy of 350 GeV [30]. As the CERN beamline already has existing, conventional magnets of 1.8 T field strength and 5.66 m length. A total length of 23 m of those magnets would provide enough integrated field, their return fields would reflect muons back into the HS vessel aperture. Thus, the design of new magnets is mandatory. Passive shielding solutions proved unsuited in simulations.

4.3.3 ν_τ detector

The tau neutrino detector is primarily designed to perform the first ever observation of the anti tau neutrino $\bar{\nu}_\tau$. Therefore it is optimized to maximize the number of ν_τ interactions. At the same time it must be relatively small due to the high muon flux along the beamline axis that is diverted away from the neutrino target by the muon shielding, which it must avoid. Since the interaction of ν_τ results in the production of τ leptons, that decay after travelling about 1μm, a spatial resolution of a micron within the neutrino target is needed. As all neutrino flavors are produced in the target, an aim of the neutrino detector design is to identify all neutrino flavors, of which the τ flavor is the most challenging due to the short decay length of the τ lepton. In addition, the SHiP neutrino detector offers the unique ability of distinguishing between ν and $\bar{\nu}$. Therefore, a charge determination of the the particles escaping the neutrino vertex must be achieved, which is done using the bending of the trajectories in a magnetic field. In order to keep the target small enough to fit in the muonshielded volume, a magnetic field of about 1 T is needed. The *Goliath magnet*[8] is one possible magnet able to achieve the requirements but other options are under active investigation.

The neutrino detector will be a high density target capable of detecting charged particles with a sub micron spatial resolution. This will be achieved using a multicomponent detector and target. Following the experience from the *OPERA* experiment, the ν_τ target will be segmented into *bricks*, each consisting of 57 thin layers of emulsion film, interleaved with 56 lead plated, each 1mm thick. This is utilizing the so called *Emulsion Cloud Chamber (ECC)* technique. The bricks combine a sub micrometer spatial resolution tracker and a high density target. Each brick has a weight of 8.3 kg and measures 128×102 mm transverse the beam direction and 79 mm longitudinal. The photo emulsion consists of AgBr crystals in a gelatine binder, that each have a diameter of 0.2μm [30]. A particle scattering on those crystals induces the growth of silver clusters along its path, that have a diameter of 0.6μm. These are visible in an optical microscope [30]. A minimal ionizing particle has a typical density of 36 silver clusters per 100μm.

Nuclear emulsion films, however, have the disadvantage of integrating all charged particle tracks over their lifetime. For SHiP, a replacement of all bricks twice a year is needed. Thus, the target must be within reach for maintenance [30].

The branching ratio of the τ lepton is largest to hadrons, as shown in table 4.2. Thus,

[8] used for example in the NA57 experiment, see [62]

Table 4.2: Branching ratios for the decay channels of the τ lepton [30].

Channel	branching ratio
$\tau^- \to e^- \nu_\tau \bar{\nu}_e$	17.8%
$\tau^- \to \mu^- \nu_\tau \bar{\nu}_\mu$	17.7%
$\tau^- \to h^- \nu_\tau (n\pi^0)$	49.5%
$\tau^- \to h^- h^- h^- \nu_\tau (n\pi^0)$	15.0%

in order to distinguish ν_τ and $\bar{\nu}_\tau$, it is mandatory to be able to measure their charge inside the target, as hadrons typically are not able to escape the ν_τ-target. Decays of the τ are separated to *long* and *short* decays. Short decays are those, where the τ decays in the same lead plate, where the neutrino interaction occurs, whereas long decays of the τ happen further downstream [30]. In the first case, selection of the τ candidates is performed by measurement of the impact parameter w.r.t the vertex of the decay's daughter particles, in the latter case based on a measurement of kink angle between τ track and daughter track [30]. The expected distribution of the decay length and kink angle of the τ lepton is shown in figure 4.11. Immediately downstream each ECC brick, *Compact Emulsion Spectrometer*

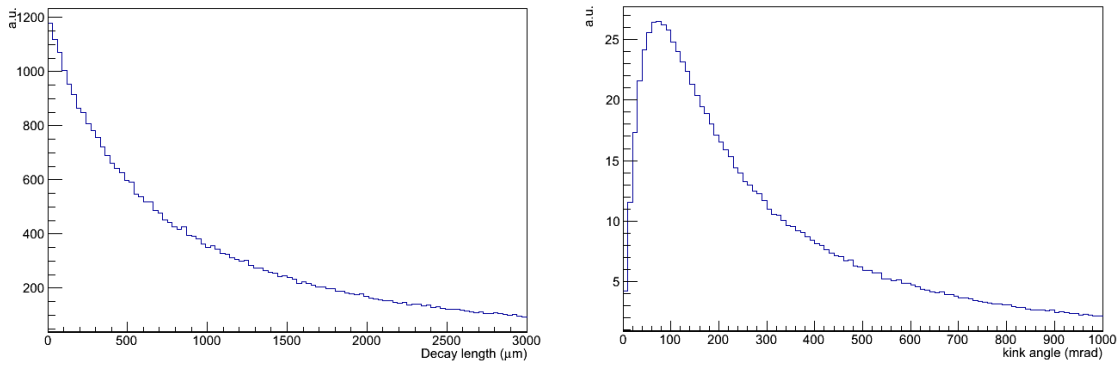

(a) decay length distribution (b) kink angle distribution

Figure 4.11: Distribution of the decay length of the τ lepton (left) and distribution of the kink angle for the decay $\tau \to h$ [30].

(CES) bricks are attached. These consist of three emulsion film layers interleaved with two Rohacell layers, each 15 mm thick. The Rohacell plates have a low density of 57 mg/cm^3, minimizing the error due to multiple Coulomb scattering on the sagitta measurement and at the same provide enough spacing between the emulsion film layers. A schematic view of one ECC brick with an attached CES is shown in figure 4.12. The set of ECC and CES is called a *detector-cell*.

The CES performance has been simulated with $\pi^\pm$ in the momentum range from 0.5 to 10 GeV/c. It is expected to be able to measure those hadrons charge with a confidence level of 3σ up to momenta of 10 GeV/c with a momentum resolution of 20% [30]. A

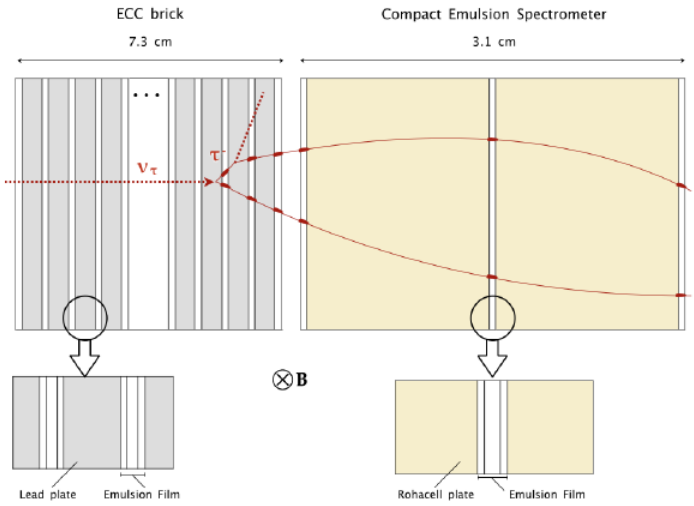

Figure 4.12: Schematic of one neutrino detector cell, consisting of an ECC brick and one unit of *compact emulsion spectrometer* (CES). The detection scheme of tau neutrino is shown with a ν_τ entering the brick from the left and a τ^- escaping the vertex and decaying in a lead plate of the brick. The thick drawn track parts are detected tracks within active detector parts [30].

schematic view of the momentum measurement is shown in 4.13. The neutrino detector of the SHiP experiment will consist of 11 wall of bricks, each wall with 15×7 bricks with a cumulative sum of 9.6 tonnes. The walls are interleaved with planes of electronic target trackers. A schematic overview of the complete neutrino target is shown in figure 4.14.

The electronic target tracker provides the time stamp for an event and predict, in which cell of the target the primary neutrino interacteed [30]. An additional plane of target tracker directly upstream the target is planned as a veto, resulting in a total of 12 target tracker planes. For the target tracker, the options of *scintillating fibres (SciFi)* and *micro-pattern gaseous detectors* are under investigation [30].

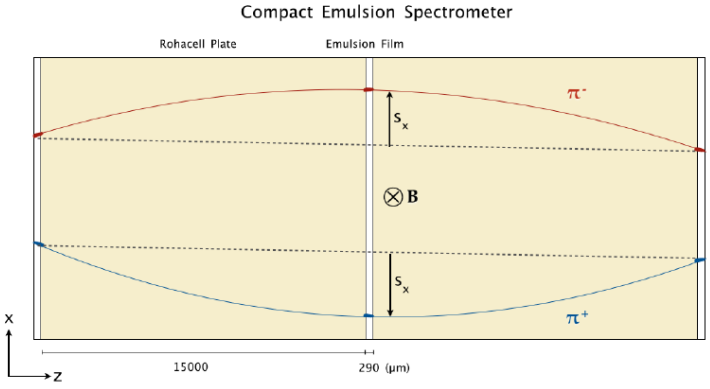

Figure 4.13: Sagitta measurement within the compact emulsion spectrometer (CES) simulated in a $1T$ magnetic field [30].

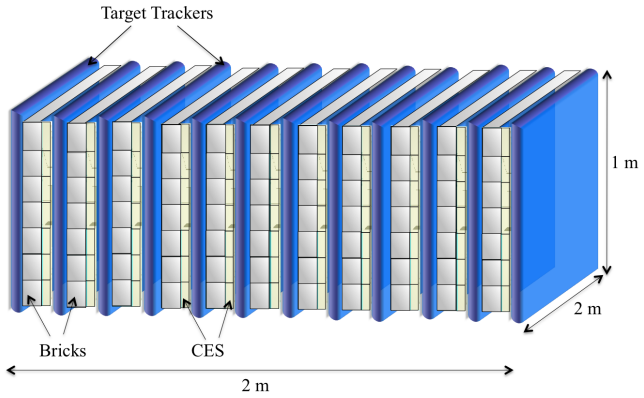

Figure 4.14: Overview of the tau neutrino target [30].

Table 4.3: Efficiency of the decay search ϵ_{ds} and the overall detection efficiency $\epsilon_{tot} = \epsilon_{geom} \cdot \epsilon_{loc} \cdot \epsilon_{ds}$ for the different decay channels of the τ lepton [30].

decay channel	$\epsilon_{ds}(\%)$	$\epsilon_{tot}(\%)$
$\tau \to \mu$	72	60
$\tau \to h$	74	62
$\tau \to 3h$	76	63
$\tau \to e$	67	56

4.3.4 Muon Magnetic Spectrometer

The main experimental objective of the muon magnetic spectrometer is a precise measurement of the charge signs and momenta of the muons emerging the neutrino target. In order to connect the muon tracks with the neutrino target, a three dimensional track of the muons needs to be reconstructed. The muon magnetic spectrometer consists of several components, all of which based on experience gained from the *OPERA* experiment. A warm magnet to bend charged particles' tracks in order to measure their charge sign, several layers of drift tube detectors and a resistive plate chamber (*RPC*) electronic tracking detector is proposed [30]. The magnet is shown in figure 4.15, it consists of two walls of iron, each made up from 12 iron layers of 5 cm thickness. The iron layers are separated by 2 cm of air, that house the RPC detectors [30]. In addition, it is equipped with top and bottom flux return yokes, the expected field along the walls is at 1.57 T [30]. The RPC detectors in the magnet provide a resolution in the range of 1 cm, the momentum measurement is performed by the more accurate drift tubes.

The drift tube detector for the SHiP muon magnetic spectrometer can be reused from the *high precision tracker* of the *OPERA* experiment. The aluminum tubes are 7926 mm

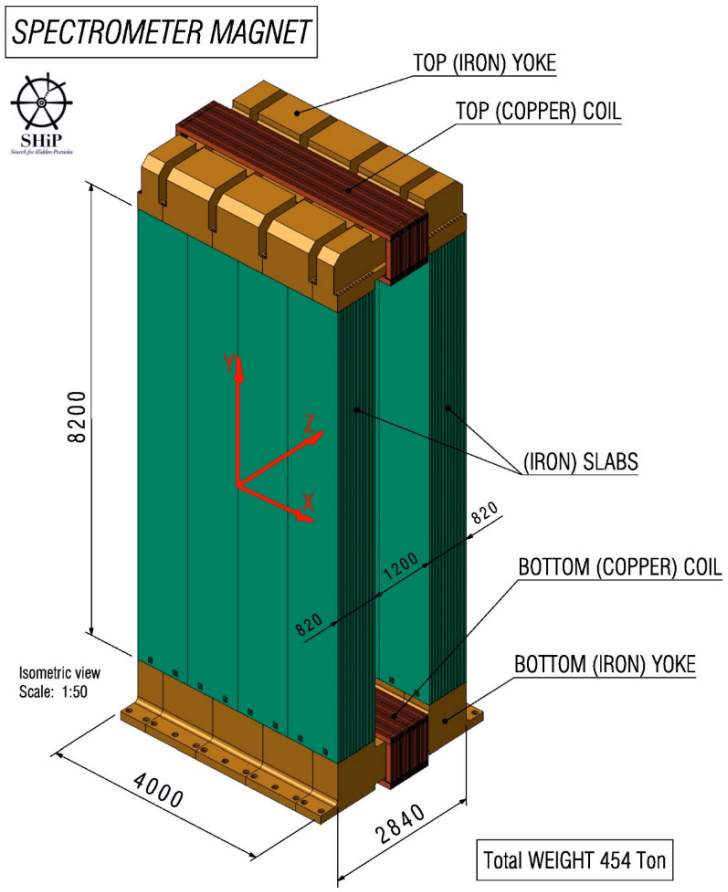

Figure 4.15: Schematic view of the warm magnet for the SHiP muon magnetic spectrometer. It consists of two walls, each made of 12 layers of 5 cm thick iron, interleaved by $2cm$ of air. This setup has a total iron thickness of 1.2 m in the beam direction, which is a compromise of high enough magnetic field and low material budget [30].

long, have an outer diameter of 38 mm and a wall thickness of 850μm [30]. The tubes are grouped to *modules* of 48 tubes, that are staggered in four layers of tubes. For the OPERA experiment, a drift gas mixture of 80% Ar and 20% CO_2 was used, which has a maximum drift time of approximately 1.3μs and a spatial resolution of 255μm. The momentum resolution at 20 GeV/c was measured to be at $\Delta p/p = 20\%$ [30]. In order to reduce in drift tubes' occupancy for the SHiP experiment, drift gas mixtures with low admixtures of molecular Nitrogen are foreseen, that are investigated within the context of this thesis. As shown in chapter 3.5, layers of drift tubes rotated by a *stereo angle* against each other are needed for a three dimensional reconstruction.

For the SHiP experiment, a stereo angle of $\varphi = \pm 3.6°$ was chosen. This angle is optimized in order to enable the reuse of the drift tubes from the decommissioned OPERA experiment with minimal changes needed. The angle must not be too large, so that the lateral dimension of the drift tube detector does not reach out to the area where the flux of diverted muons bent by the shielding is high, thus occupying the drift tubes. A schematic view of the muon magnetic spectrometer and its positioning relative to the ν_τ-target is

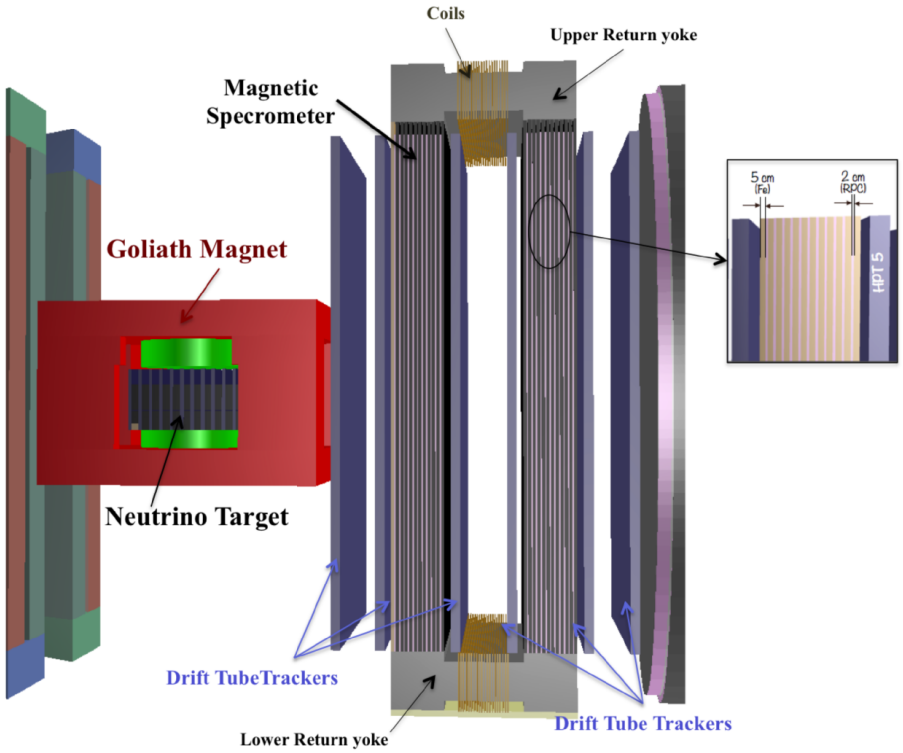

Figure 4.16: Detailed view of the ν_τ-detector and the muon magnetic spectrometer, which is placed immediately downstream the ν_τ-detector. The layered layout of the magnet, which is interleaved by RPC detectors, as well as the layers of drift tubes can be seen [30].

shown in figure 4.16.

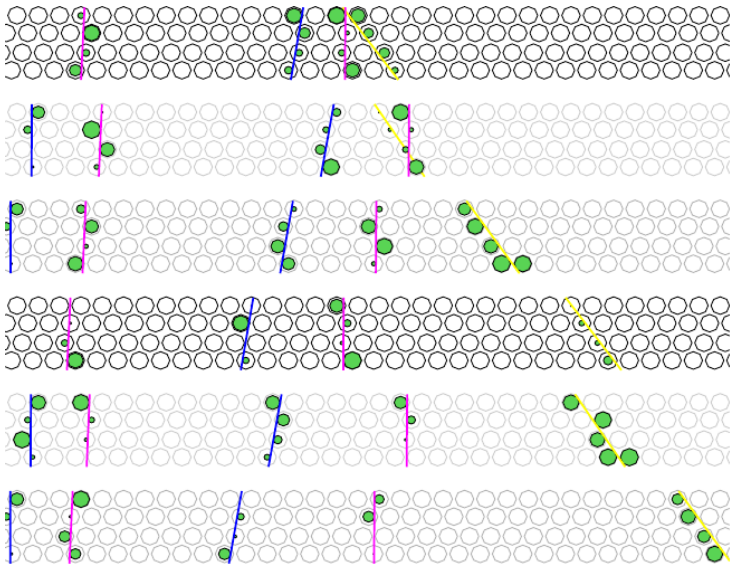

Figure 4.17: Simulated tracks of a ν_μ^{CC}-charm event. The first six planes of drift tubes are shown, the different gray shades of the tubes account for the three projections of rotated drift tubes. The green circles in the tubes represent drift circles based on drift time measurements and the rt-relation. Pink tracks refer to muons, yellow tracks show electrons and blue tracks show hadrons [30].

4.3.5 Hidden sector detector

As this thesis focuses of the neutrino detector and muon magnetic spectrometer, only a brief introduction to the hidden sector detector is given. For details see [30] and [11]. The hidden sector detector consists of several components ordered from upstream to downstream:

1. Decay volume with veto
2. spectrometer tracker
3. electromagnetic and hadronic calorimeter
4. muon detector

The decay volume design foresees an evacuated, double-walled vessel with an elliptical shape. It has a horizontal dimension of 5 m and a vertical dimension of 10 m. The volume is planned to be evacuated to a level of 10^{-6} bar in order to minimize the number of interactions with neutrinos and muons [30]. Different designs for the HS decay volume are under investigation as well. As very low observation rates for hidden sector particles are expected, a strong background rejection capability is crucial [30]. Therefore, *veto taggers* both upstream and surrounding the decay volume are foreseen.

The surrounding background tagger is based on a liquid scintillator filled in between the walls of the decay vessel, which provides an almost full solid angle coverage. The light collection is planned to be performed utilizing the *wavelength-shifting optical module (WOM)* technique with PMTs[9].

For the upstream veto tagger a design using an array of plastic scintillators is foreseen, which combines low cost with high efficiency, large coverage and low maintenance [30]. Using this upstream veto tagger, the background from neutral kaons is thought to become neglegible and it provides a veto on muons entering the HS vessel through its front window [30]. It is complemented with an additional *straw veto tagger*, located $5m$ further upstream in the vacuum, using a minimal material budget at the cost of slightly lower efficiency [30].

The spectrometer tracker directly downstream the decay volume must provide track- and momentum reconstruction of charged particles originating in hidden particle decays. To achieve this task, the use of straw tubes, operating in a magnetic field is planned. This needs a time stamp with a resolution at the order of one nanosecond. Therefore, a timing detector is planned, for which plastic scintillators and RPCs are under investigation. [30].

[9] for more details see [30].

The calorimeters downstream the spectrometer tracker follow the well known design in high energy physics. Directly downstream the spectrometer, an electromagnetic calorimeter (ECAL) is present, which must have a high energy resolution as well as the ability to identify electrons, photons and pions [30]. This is crucial in order to separate HNL decays from Kaon decays. The ECAL is consists of cells, each being made as sampling scintillator-lead structure, readout by plastic fibres [30].

The *hadronic calorimeter (HCAL)* must now separate pions from muons, especially for low energies and tag neutral hadrons, that have escaped observation on all other detector parts. It is designed with a layered layout of alternating 1.5 cm of steel and 0.5 cm of scintillator, wrapped by highly reflective Tyvek paper [30].

The muon detector must perform the identification of muons with high efficiency. Therefore, a detector using walls of scintillator bars in both horizontal and vertical orientation are set up, providing a granularity of five to ten centimeters. The walls of scintillators are interleaved with passive iron filters [30].

5 Experimental setup

The experimental setup is divided into several parts. They will be described in this chapter. It consists of the drift tube itself, a gas flow system, two plastic scintillators with photomultiplier tubes acting as trigger system as well as electronics and analog to digital conversion. Each component will be shown in the following sections.

5.1 Drift tube

Within the context of this thesis, a single drift tube is used. The used aluminum drift tube has a length of $L = 30\,\text{cm}$ and an outer diameter of $d_o = 38^{+0}_{-0.15}\text{mm}$. The wall thickness measures $850^{+0}_{-150}\,\mu\text{m}$. In its center, a gold plated tungsten wire with a diameter of $45\mu\text{m}$ is clamped, acting as anode. The drift tube design is the same as the drift tubes for the precision tracker of the *OPERA* experiment and is described in [42]. The drift tube setup has a shielded box for a radioactive source[1], which is not used within the context of this thesis. The tube is closed with a mylar foil against the source housing. A schematic view of the tube with source housing and struts for mechanical construction support is shown in figure 5.1. Figure 5.2 shows a photo of the real setup as used for the here shown measurements. A box containing the *L3* electronic amplifier[2] and wiring for

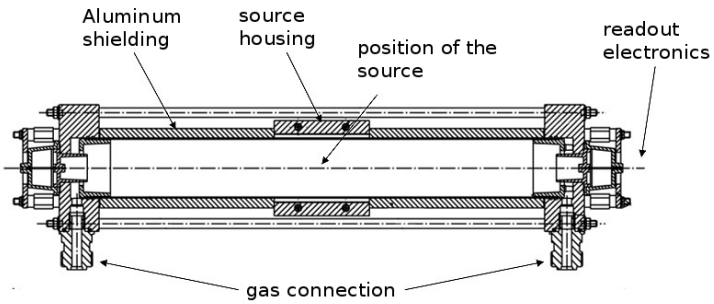

Figure 5.1: Schematic view of the 30 cm drift tube. In the center of the tube, a shielded aluminum housing for a radioactive source is present, which is not used within the context of this thesis [42] (edited).

the high voltage supply is attached to one end of the drift tube.

[1] it was originally designed to contain a ^{55}Fe source

[2] originally designed for the L3 experiment at CERN. For more information see section 5.4.1

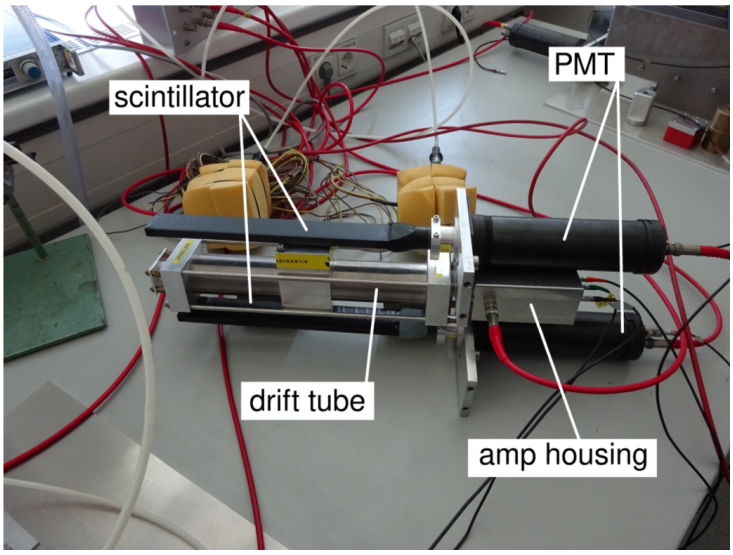

Figure 5.2: Photography of the setup of drift tube itself as well as the scintillators with photomultiplier tubes acting as triggersystem

5.2 Gas system

The gas system must perform the tasks of providing a constant, low flow of drift gas through the drift tube as well as a rough control of the gaspressure within the tube. The pressure should be at atmospheric pressure, a monitoring of the pressure and temperature is not present.

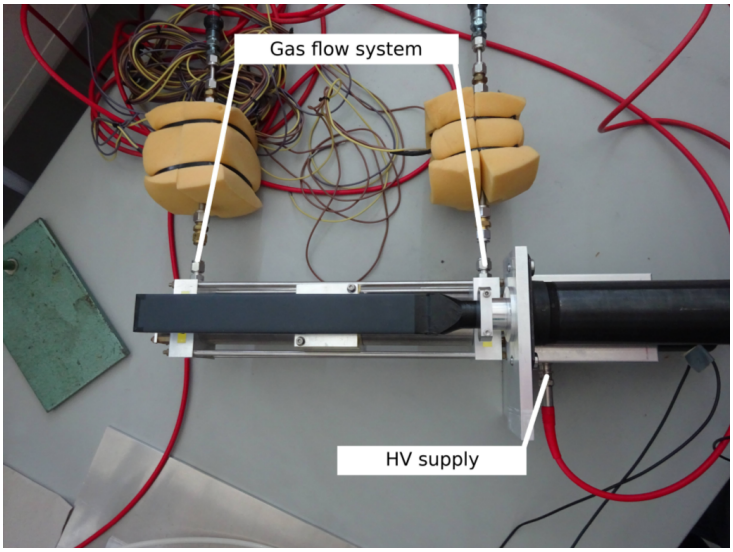

Figure 5.3: Experimental setup shown from above. The gas in- and outflow to the tube as well as its HV supply can be seen.

The drift gas is supplied by a pressurized gas tank with an adjustable pressure reducer. attached to it. Pressure reduced gas flows through an adjustable flowmeter to the drift tube. Downstream the flowmeter the gas enters the drifttube on one side, the outflow is

on the other side of the tube. The gas is bled out of the system through a *bubbler*, an oil filled glas tube. The atmospheric pressure applies force on the oil's surface such that only an atmosphere exceeding pressure inside the tube is enabled to escape the bubbler. The flowmeter is set to a low gas flow in order to enable the drift tube to compensate its inner gas pressure with respect to atmospheric pressure. A too high inflow of gas might result in an exceed in pressure since the tube has a limited capability of bleeding gas through its closure by a bubbler. The gas tank with the attached pressure reducer is shown in figure 5.4, the flowmeter as well as the gas systems closure with the bubbler are shown in figure 5.5. For flushing a new gas mixture to the tube, a flow of approximately $5\,l/h$ is set. During normal operation, the flow is reduced to about $1\,l/h$.

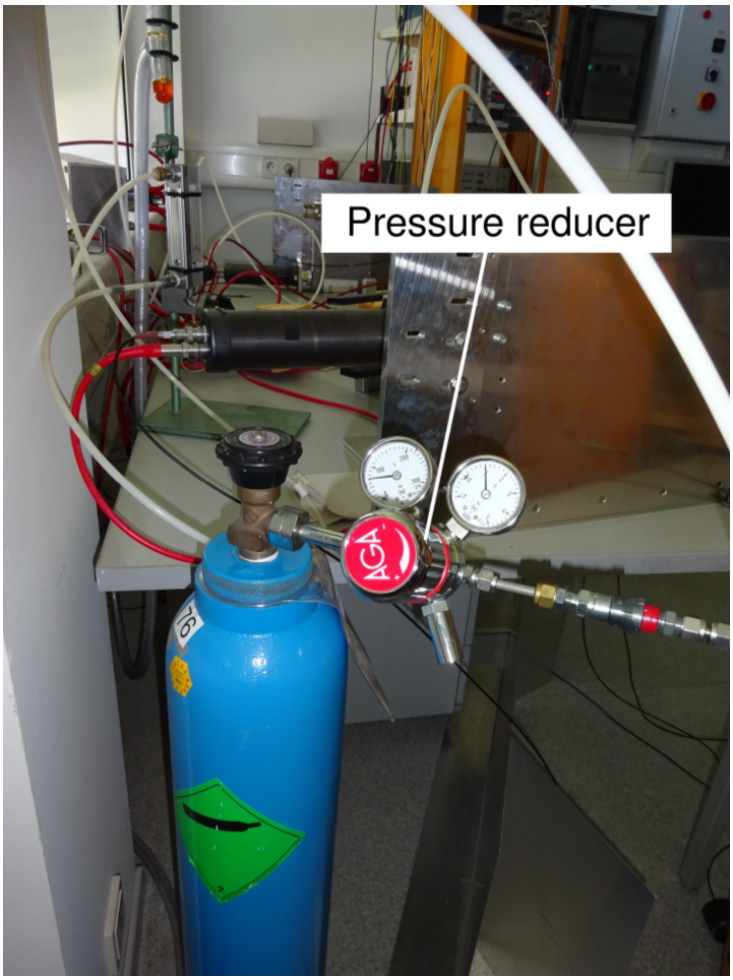

Figure 5.4: System for reducing the gas pressure to order of few bars.

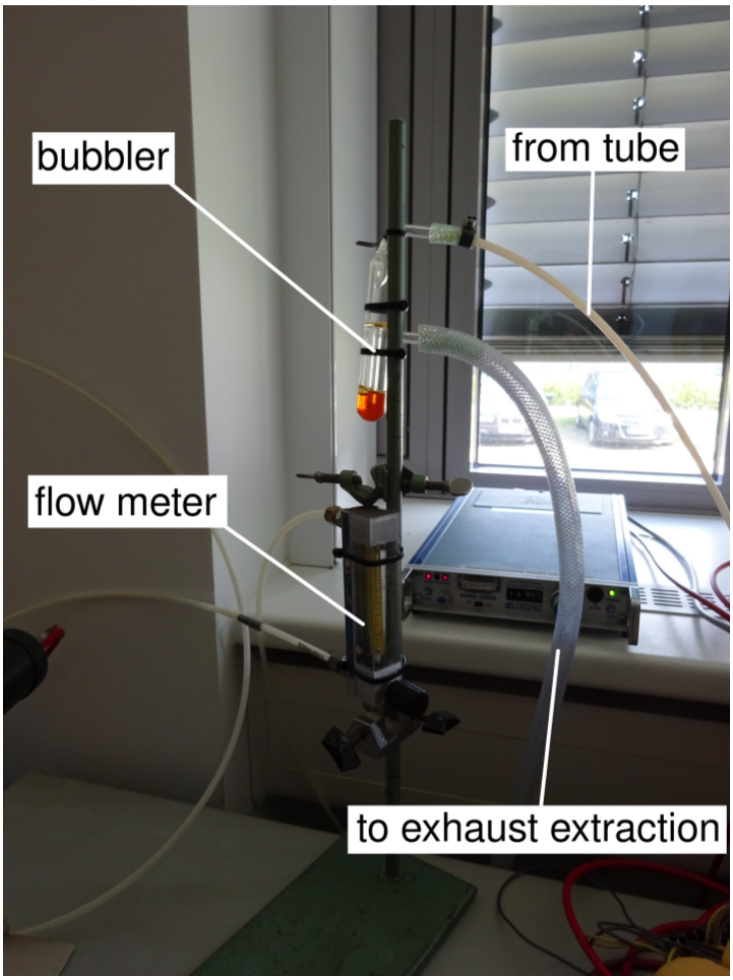

Figure 5.5: Photography of the *bubbler*. An oil filled glas tube acting as pressure control with coupling to atmospheric pressure. The atmospheric pressure presses onto the oil's surface, suppressing gas flowing out of the tube through the oil. So, a self compensating pressure control is achieved, assuming the inflow of gas to the tube is reasonable low. The inflow is controlled using the flowmeter, mounted under the bubbler. A rotary knob adjusts the gas flow. For flushing the drift tube with a new gas when changing the gas mixture, the flow is adjusted to approximately $5\,l/h$.

5.3 Trigger

An electronic trigger is realized by two plastic scintillators, one set above, one below the drift tube. Both scintillators are equipped with the same model of *Photomoltiplier Tubes (PMTs)*. A coincidence of both PMTs showing a signal within a short time frame is used as trigger.

The scintillators are seperated by a distance of $d_{\text{scint}} = 15\,\text{cm}$ from each other. They are 3.7 cm wide and 30 cm long. They completely overlap the drift tube.

The measurements are performed using *atmospheric muons* as probe particles. A muon traversing both scintillators must traverse the tube too for geometric reasons. The short distance between both scintillators and the approximate speed of light of the muons refer

to a muon time of flight of less than one nanosecond. This is lower than the time resolution of the following electronics[3]. The signals of the two scintillators can be approximated as instantanious. The PMTs are connected to the electronics with cables of equal length. Given the fast signal development of scintillators and PMTs, the trigger signal will be faster than the drift tube signal[4]. A delay, however, is not needed due to the ring buffer of the *Flash Analog to Digital Converter (FADC)* that is used for signal readout.

First, the signals of the PMTs are discriminated to achieve *NIM*[5] logic signals with adjustable length in time. The threshold voltage U_{th} is adjustable. The discriminated logic signals of the two PMTs are passed to a *logic unit* &-circuitry. Its output is a NIM logic signal showing a coincidence of both PMTs. The NIM logic signal is the trigger signal.

As the scintillators are placed along the tube axis, covering the complete drift tube cross section, edge effects at the tube's ends cannot be neglected. About one tube diameter off the end caps, the electric field in the tube does not remain radially symmetric. This may result in higher drift times for muon tracks passing near the end caps. The effect due to the angular acceptance of tracks deviated with respect to the tube's longitudinal axis, can be neglected. A track passing the tube entering on one end of the tube and escaping it at the opposite, longitudinal end take about one nanosecond for that distance, which is smaller than the time resolution of the FADC of 4 ns. Additionally, horizonal muons are suppressed by their $\cos^2(\theta)$ distribution.

[3]For a list of used hardware, see chapter 5.4

[4]see section 3.3.4 for drift tube signal development

[5]Nuclear Instrumentation Modules - standard in nuclear experiments, logic signals are $-800\,\mathrm{mV}$

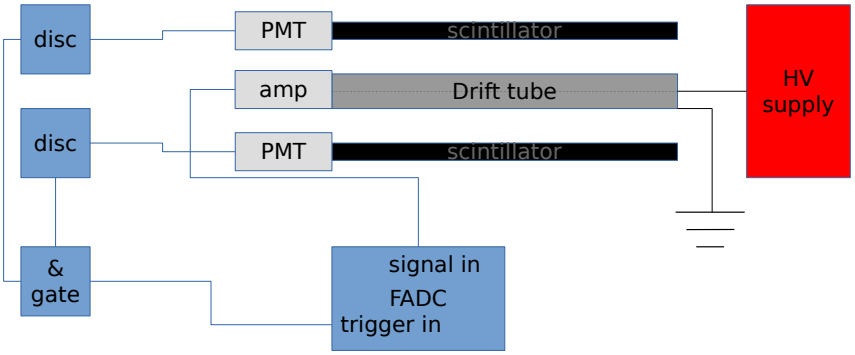

Figure 5.6: Schematic drawing of the experimental setup. The gas system is not shown.

5.4 Electronics

A *Wenzel N 1130-4 H.V. Power Supply* supplies the drift tube's high voltage. It is offering four high voltage channels of switchable polarity, supplying up to 6 kV at 0.5 mA. The accuracy is 10 V. All logic signals are NIM standard, being −800 mV for a high state and 0 V for low. All voltage measurements are performed with a closure at $R_{\text{in}} = 50\,\Omega$.

A *LeCroy Model 623 octal discriminator* discriminates the PMT signals. The trigger signal is produced by a coincidence of both discriminated PMT signals using the *and* logic mode of a *CAEN Mod. N405 3 Fold logic unit*.

5.4.1 Amplification

The anode wire signals are too small to be displayable on an FADC, thus they have to be amplified.The hybrid *L3* differential amplifier [83, 71] is used in this setup. The amplifier's circuit layout is shown in figure A.1 on page 103[6]. The positive out of the amplifier is headed to the readout electronics, the negative out is displayed on an oscilloscope. Note that the positive out shows negative voltages, it is not inverted. A photo of an inverted event is shown in figure 5.7.

The operating voltage $U_{\text{op}} = 5\,\text{V}$ of the L3 amplifier is provided by a floating laboratory power supply. The amplification is frequency dependent. Absolute measurements of the gas amplification, could be performed, correcting this effect of the amplifier. In the context

[6]Thanks to Prof. Dr. Walter Schmidt-Parzefall for providing the layout

of this thesis, no absolute gas amplification measurements are performed, only relative measurements that are comparable with each other among different gas mixtures.

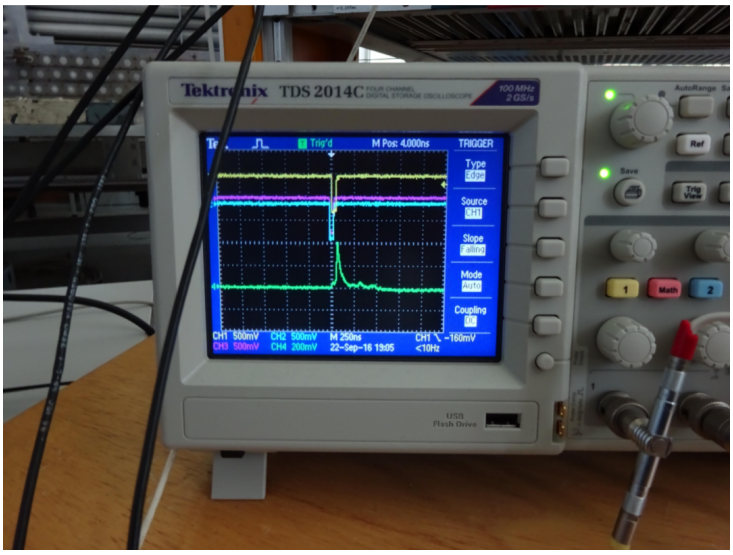

Figure 5.7: Photography of the display of an oscilloscope showing a triggered event. The violet and green signals show the discriminated signals of the two PMTs, the yellow displayed signal shows the coincidence of both PMTs and the signal displayed in green shows the negative part of the differential signal from the L3 amplifier, so a signal from the drift tube. Note the drift tube's signal here is positive, because the signal itself is a negative voltage, amplified and inverted by the amplifier. The uninverted signal from the amplifier is transferred to the FADC.

5.4.2 Analog to digital conversion

The conversion from analog voltages to digital data is performed by a programmable, Flash Analog to Digital Converter (*FADC*) model *CAEN mod. V1720* as shown in figure 5.8. The FADC is connected to a PC, storing the acquired data and steering the FADC via a *CAEN mod. V1718* USB VME Bridge. It is operated at a sampling rate of 250 MHz, resulting in a time resolution of 4 ns per bin. The accepted range of input voltage is $[-6\,\mathrm{V}; +6\,\mathrm{V}]$ which is mapped with 12 bit resolution (4096 steps) [26]. The voltage, read in arbitrary FADC units U_{ADC}, can be converted to a real voltage using:

$$U[\mathrm{V}] = \frac{12\,\mathrm{V}}{4096} U_{\mathrm{ADC}} \tag{5.1}$$

Chapter 5.6 describes the software used for FADC readout and data processing.

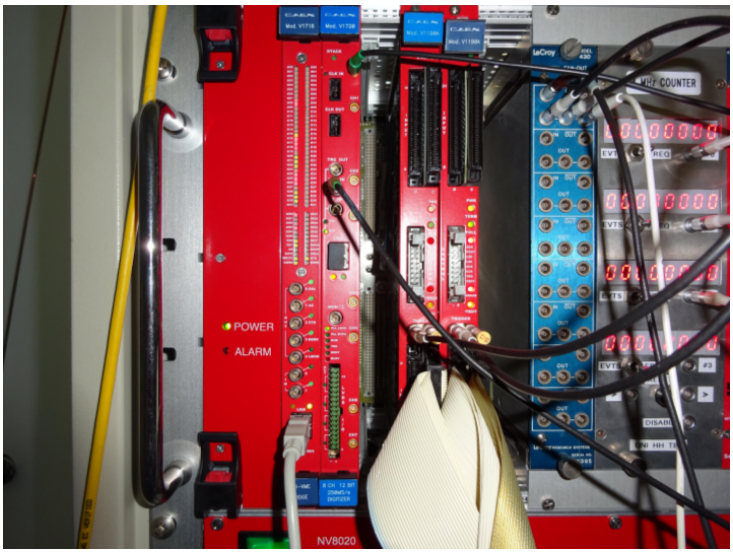

Figure 5.8: Photography of the FADC CAEN mod. V1720 and the USB VME Bridge CAEN mod. V1718.

5.5 Commissioning

The commissioning included several tasks. The drift tube that was chosen to work with was not used for several years. During its downtime, it was not flooded with a gas to protection the drift tube system against aging[7]. The first goal was the reproduction of the well known spectrum of drift times using a gas mixture of 80% Ar and 20% of CO_2. In order to be able to perform this task, the commissioning of a gas system, electronic readout and voltage supply as well as a trigger system was necessary.

When changing the drift gas mixture, the tube's volume needs to be flushed several times with the new drift gas mixture in order to ensure a pure drift gas mixture in the drift tube. Especially at commissioning, a flooding of the tube is necessary to avoid admixtures of water or oxygen, that lead to aging effects.

5.6 Software

The FADC was read using an open source software from [50]. The further processing of the data was performed using a self-developed software that is also provided as open source software at [40]. In comparison to earlier methods of drift time measurements, software-based analysis of the raw voltage signals from the drift tube's sense wire offers the following opportunities of studies on *the same dataset*:

1. analyze the effect of different threshold voltages on the drift time spectrum

2. study afterpulses on large datasets

[7] see chapter 3.6.4

3. study distributions of signal ends

4. ability to apply new analysis methods after data acquisition

The software is written in C++ using the ROOT framework [23] in major version 6, strictly developed in object oriented design. It is as well using the openMP library for multithreading, reducing the runtime for finding the drift time spectrum for a set of triggered events. A class diagram in *Unified Modeling Language (UML)* can be found in the appendix, figure B.1.

6 Reproduction of known results with 80% Ar and 20% CO_2

In order to test the detector performance after commissioning, the first task is the reproduction of the drift time spectrum of the gas mixture 80% Ar and 20% CO_2[1] which is well known from the OPERA drift tubes. All measurements are performed using atmospheric muons. 24 hours of data acquisition resulted in approximately 20000 triggered events. The number of random trigger coincidences in that time was measured to about 400.

Note that all measurements that are presented in the following are performed with a single drift tube, thus without the ability for tracking. This deprives the possibility to precisely test the maximum drift time against a reconstructed track. Therefore, less precise methods need to be applied and any absolute measures of time, especially error estimations need to be read with care. When comparing results of different drift gas mixtures later, these errors are expected to cancel out.

6.1 Voltage pulse shape

The measurements are performed with an FADC, recording the drift tube signal after electronic amplification. An example pulse of a triggered event using a high voltage of $U_{\mathrm{HV}} = 2300$ V is shown in figure 6.1. The typical features of a drift tube voltage pulse can be seen: The signal height of a voltage pulse is proportional to the number of clusters reaching the anode wire. Assuming a constant density of ionization clusters along the particle track, for geometrical reasons, the number of ionization clusters reaching the anode wire is larger for short drift times. Thus, the first pulse in one event is typically the one with the highest voltage. Another effect which will be of use later in the analysis is due to the electronic amplifier: On a timescale of few nanoseconds, when a signal is amplified by the L3-amplifier, the baseline of the voltage is shifted upwards due to a capacitor charging. This effect can be seen in figure 6.2, where the signal height is lower, thus small variations are not as suppressed due to scaling of the plot.

[1] in the following Ar:CO_2 80:20

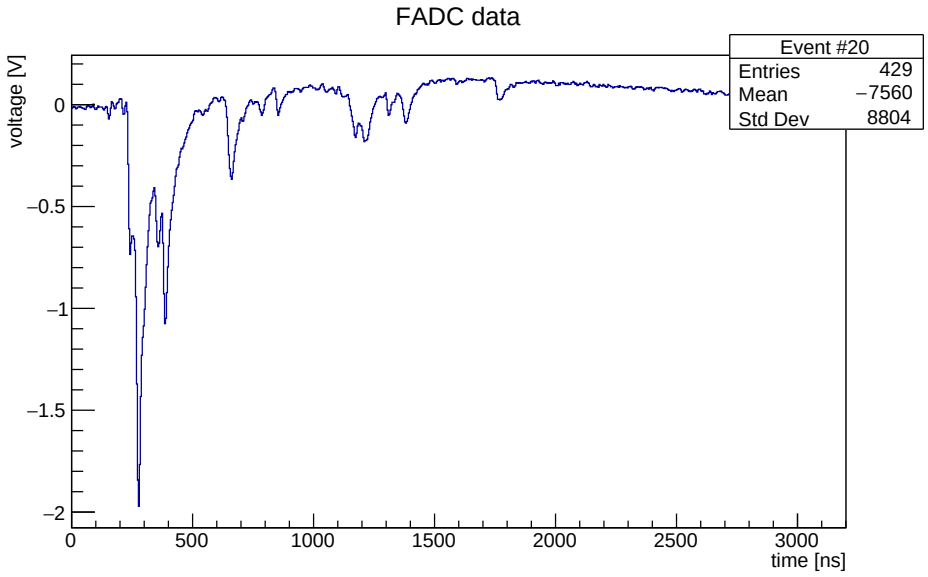

Figure 6.1: Voltage pulse shape. Multiple peaks, originating from multiple ionization clusters can be seen.

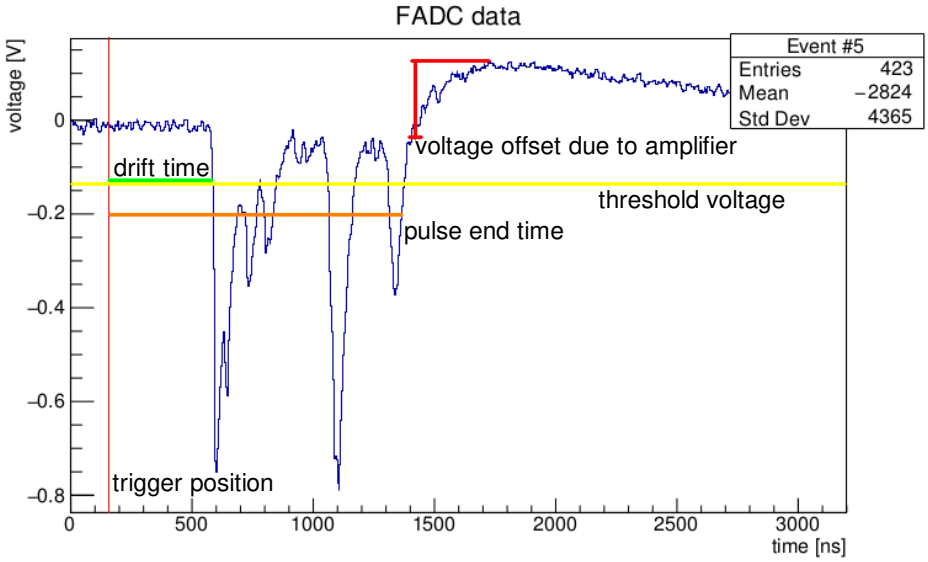

Figure 6.2: Pulse shape for 80% Ar and 20% CO_2 at $U_{HV} = 2300$ V. Features such as the drift time (green), threshold voltage (yellow) and voltage offset (red, right) of the electronic amplifier can be seen. The position of the trigger signal on the time axis is represented by a vertical, red line (left). The position is at $t_{trigger} = 160$ ns for all measurements in the following. For further analysis, this trigger offset is already subtracted.

6.2 Charge collection

The amount of electric charge Q in one pulse is proportional to the gas amplification. As already described, due to effects of the electronic amplifier, no absolute gas amplification

is measured. A measure proportional to the charge is the integral of a voltage pulse, since the voltage is proportional to the current via *Ohm's law*.

$$I(t) = \frac{U(t)}{R}$$

The integral over the current yields the charge transported with the current as the following equation holds true:

$$I(t) = \frac{dQ}{dt}$$

Hence, the integral over the voltage of a pulse is proportional to the charge. However, the voltage is electronically amplified and not equal to the real charge in the drift tube. Plots of the integrals of the pulses (figures 6.1 and 6.2) are shown in figure 6.3. Note that these

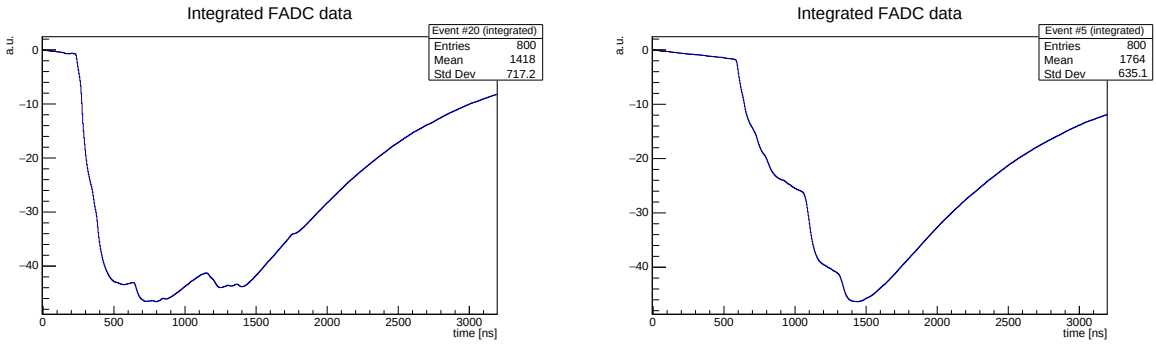

(a) Event number 20

(b) Event number 5

Figure 6.3: Integrals of two voltage pulses for Ar:CO_2 80:20 at $U_{HV} = 2300$ V. Figure 6.3(a) shows the integral of the the pulse shown in figure 6.1, 6.3(b) corresponds to 6.2. These show a minimum which can be explained with an effect of the electronic amplifier that shifts the zero voltage to a positive voltage after the first voltage pulse. This is due to a capacitor in the amplifier charging and results in a global minimum of the integral of one pulse.

plots show a minimum, which is due to the amplifier offsetting the voltage. Consequently, after the voltage pulse in the tube, a low positive voltage is measured after the amplifier, resulting in a rising integral after the pulse ended. The minimum position of the integral of a pulse can therefore be a measure of the time that the pulse ended, which will later be discussed. As within the context of this thesis, a specific effect of the electronic amplifier is used, this effect can be mimicked in software by manually changing the zero voltage level after finding the drift time.

The height of the minimum of a pulse integral is proportional to the charge in a pulse. The distribution of integral minimum heights for Ar:CO_2 80:20 is shown in figure 6.4. The arithmetic mean of that distribution will be used as rough estimate of the gas amplification. The drift tube is known to be safely operable at this high voltage. Too high amplification might lead to sparks damaging the tube.

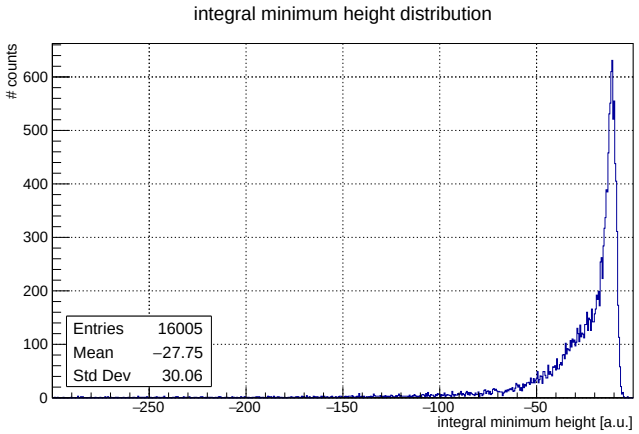

Figure 6.4: Distribution of integral minimum heights for Ar:CO_2 80:20 at $U_{\mathrm{HV}} = 2300$ V. This is used as a rough estimate for the gas amplification. For all other drift gas mixtures, the high voltage is slowly raised until an oscilloscope shows signals of the drift tube, when the PMTs trigger an event. Then, measurements for approximately 24 hours are performed and the integral minimum distribution is computed for this measurement. The arithmetic mean of this distribution is then used as estimate for the gas amplification. If, for the new drift gas mixture, the mean value is lower than for this reference gas, the high voltage is tuned up by 50 V until the mean values are roughly the same. The aim of this procedure is not to damage the tube due to too high gas amplification, enabling sparks to occur, thus damaging the drift tube.

6.3 Drift time spectrum

From the signal pulse shapes recorded by the FADC, the drift time for each voltage pulse is measured by looping over each bin of the FADC data and checking whether the chosen threshold of $U_{\mathrm{th}} = -146$ mV is exceeded (see figure 6.2). The number of the first bin fulfilling this condition is then multiplied with the time scale of the ADC bins (4 ns) and returned, the iteration is stopped. If the threshold has not been exceeded after checking the last bin in an event, a negative drift time is returned to indicate events that were triggered but no drift tube signal was found. A flow chart of the algorithm is show in figure 6.5. The amount of events with positive drift times over the total number of events is used to determine the efficiency of the drift tube. Note that the threshold can be arbitrarily chosen within the software and may thus be changed for later analysis.

The drift time spectrum, obtained utilizing the method described above is shown in figure 6.6. Threshold voltages lower than $U_{th} = -146$ mV had no significant effect on the shape of the drift time spectrum but just lowered the efficiency. On the other hand, threshold voltages *higher than* -146 mV, showed errors in the computation of the drift time spectrum. Examplary drift time spectra with $U_{\mathrm{th}} = -29$ mV and $U_{\mathrm{th}} = -234$ mV are shown in figure 6.7. For a detailed description of possible error sources, see chapter 6.8.

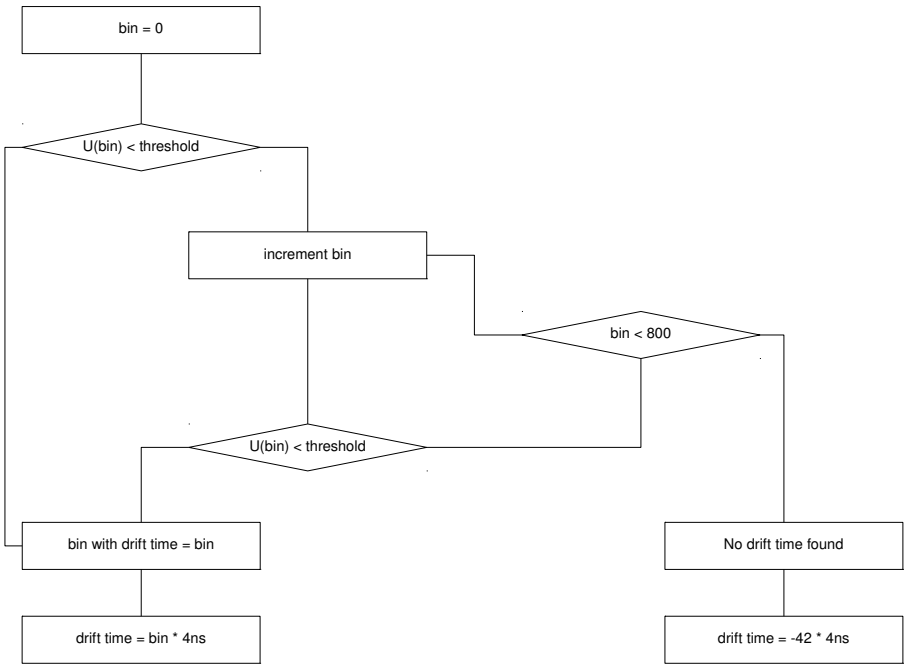

Figure 6.5: Flow chart of the algorithm for determining the drift time

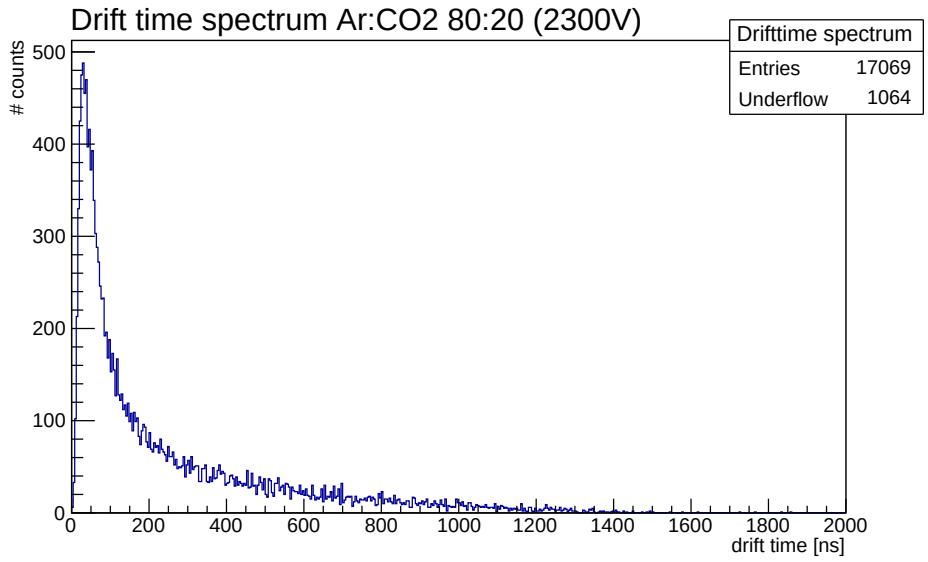

Figure 6.6: Measured drift time spectrum for 80% Ar and 20% CO_2 at $U_{\mathrm{HV}} = 2300$ V with a threshold of $U_{\mathrm{th}} = -146$ mV. This drift time spectrum is compatible with previous results using the same type of drift tube with the same gas mixture. It does *not* show the *shoulder*, a common feature which describes a cutoff for high drift times at the tube's wall. This is due to edge effects, as the scintillators, acting as trigger overlap the whole drift tube, which is relatively short. Thus, edge effects, resulting in deviations of radial symmetry of the electric field, cannot be neglected.

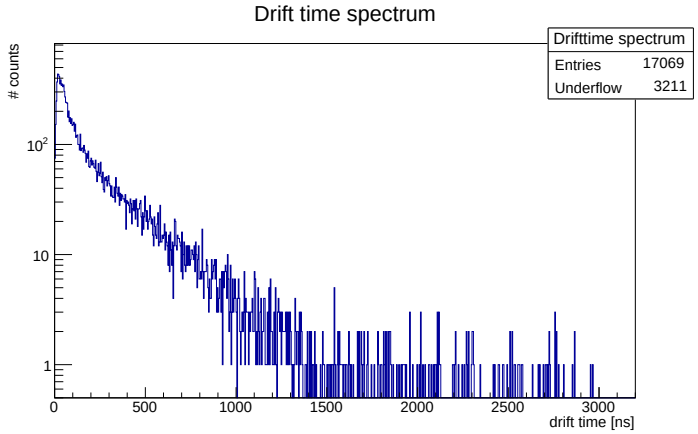

(a) $U_{\text{th}} = -29$ mV

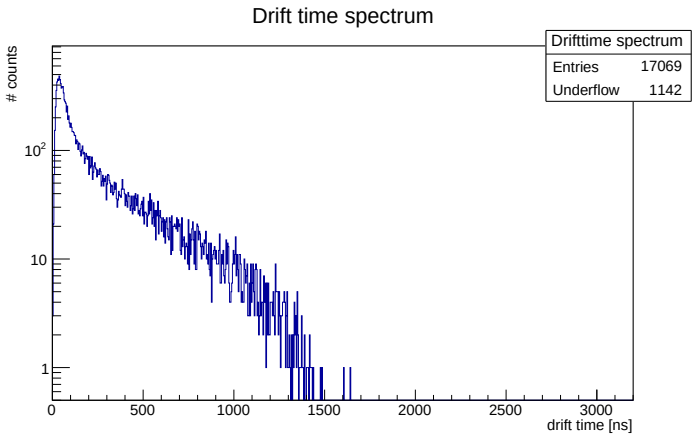

(b) $U_{\text{th}} = -234$ mV

Figure 6.7: Drift time spectra of Ar:CO_2 80:20 at $U_{\text{HV}} = 2300$ V with different threshold voltages for the drift time reconstruction. A logarithmic scale is chosen to emphasize single counts for higher drift times. The upper one is computed with a *smaller* threshold of $U_{\text{th}} = -29$ mV (note that a smaller threshold means higher voltage), the lower one with a larger threshold of $U_{\text{th}} = -234$ mV. A smaller threshold shows more bias at the end of the drift time spectrum. Larger thresholds, on the other hand, do not enhance the quality of the drift time spectrum while reducing the overall efficiency. A threshold of $U_{\text{th}} = -146$ mV was found as good compromise between bias and efficiency.

6.4 Signal end distribution and maximum drift time

Two different methods are presented for determining the maximum drift time (D1,D2). Additionally, two methods to find the end position of a voltage pulse are discussed (V1,V2). A correlation of the ends of voltage pulses with the maximum drift time is investigated. The goal was to determine robust methods for finding the maximum drift time, corresponding to a particle passing the drift tube near the cathode wall. In particular, the following methods are introduced:

D1. Fitting a linear function to the end of the drift time spectrum and finding the root

of the linear function.

D2. Finding the time $t_{\max}$, where a fraction of 99.95% of events are included when integrating the drift time spectrum up to that time.

V1. Finding the last bin of the FADC voltage pulses exceeding a threshold voltage U_{th}. (Further-on called *pulse end*.)

V2. Finding the position of the minimum of the pulse integral. (Called *integral minimum position*.)

6.4.1 Linear fit to the end of the drift time spectrum

The maximum drift time can be found by fitting a linear function to the end of the drift time spectrum. Examples of a linear fit are shown in figure 6.8. By finding the root of

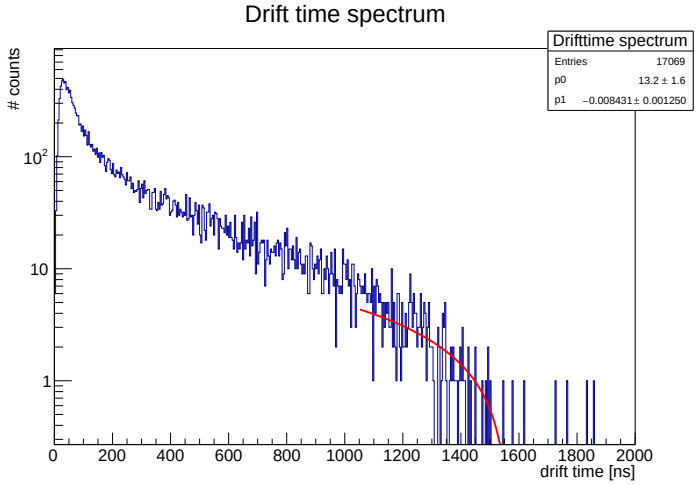

Figure 6.8: Analysis of the maximum drift time by fitting a linear function to the end of the drift time spectrum. This a logarithmic plot for better visibility.

the linear function fitted to the end of the drift time spectrum, the end of the drift time spectrum was determined to be

$$t_{\max} = (1565 \pm 302)\text{ns}. \tag{6.1}$$

The fit was performed in a range around the *first bin* with zero entries t_0 of $[0.8t_0, 1.2t_0]$. The error was calculated using Gaussian propagation of errors on the errors of the fitted parameters. Note that this method shows a large error ($\approx 20\%$). A linear function does not describe the end of the drift time spectrum and is performed in a range with few entries, thus low statistics. However, this does provide an estimate of the maximum drift time. The error is expected to be a massive over-estimation and should not be taken too seriously since it is calculated from the parameters of a fit that does not describe the real

behavior. An absolute measure of the maximum drift time should be obtained in a setup suited for tracking in future research.

6.4.2 Integrating the drift time spectrum

This method defines a time t_{end} as the bin in the drift time spectrum up to which 99.95% of events are integrated. Thus, the time t_{end} is defined via equation 6.2:

$$\int_0^{t_{\text{end}}} \frac{dN}{dt'} dt' = 0.9995\, N_{\text{events}} \tag{6.2}$$

This method results in a *fixed* time close to the maximum drift time achieved with a linear fit but is easily automizable. Following equation 3.21, given the rt-relation, this t_{end} can be found by finding the first bin in the rt-relation, where the drift radius exceeds 99.95% of the drift tube's inner radius. This method results in a maximum drift time of

$$t_{\text{end}} = 1584\,\text{ns}$$

Here, no error is given since this is defined time near the maximum drift time. Note that this is an empirical method without physical motivation. However, this is easily automizable. It is used for the following:

1. Computing the slope of a linear function to check for linearity of the rt-relation (see chapter 6.5)

2. Definition of a time after which a pulse exceeding a threshold voltage is counted as afterpulse

Even though this is an empirical method, it seems reasonable. The value found is well within the error from the fitting method. Additionally, the deviation from the value computed using the fit is well below the systematic error, that is described in chapter 6.8.

6.4.3 Pulse end

First, in analogy to finding the drift time, the *last bin* where a given threshold was excceeded, is found by looping over all bins for each triggered event. The distribution of signal ends using this method with a threshold of $-146\,\text{mV}$ is shown in figure 6.9.

When setting the threshold to 0 V, the distribution peaks at the maximum drift time, as shown in figure 6.10, On the other hand, this method is sensitive to bias and afterpulses. Thus, the maximum recordable time of the FADC is with a high frequency. The peak near the maximum drift time is an over-estimation, since the drift time corresponds to the falling slope of a pulse whereas this method finds the rising slope. The second peak in figure 6.10 is due to bias. For events with small signal heights, the capacitor in the

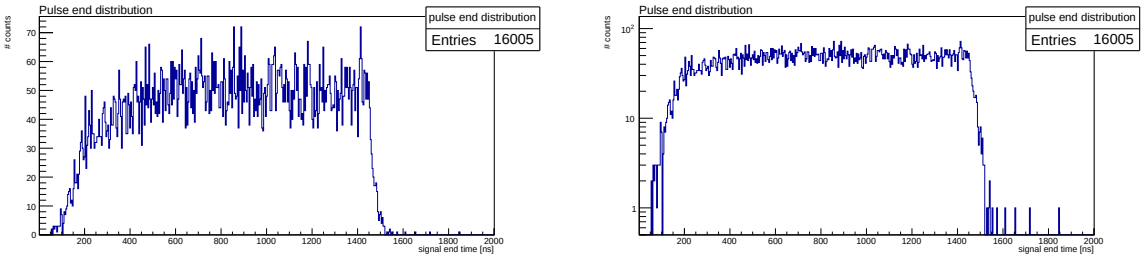

(a) linear scale (b) logarithmic scale

Figure 6.9: Voltage pulse end distribution obtained by finding the last bin, where a threshold of $U_{\text{th}} = -146\,\text{mV}$ is undershot.

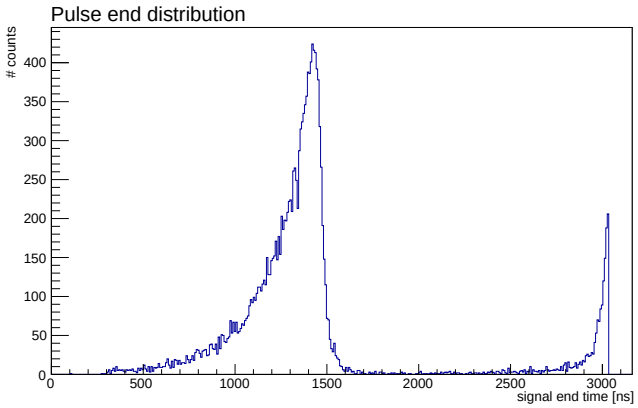

Figure 6.10: Distribution of voltage pulse ends by finding the last bin, where the threshold voltage $U_{\text{th}} = 0\,\text{V}$ is undershot. This peaks at the maximum drift time but is not robust to late pulses. It does often find the maximum recordable time of the FADC. The second peak is due a capacitor in the amplifier. For smaller pulses the voltage offset is small, thus a voltage of zero can be reached within the record time of the FADC. For those pulses, bias is counted and a bin at the end of the FADC record is found.

amplifier is less charged than for higher events. Thus, durings its discharge after the pulse, the voltage reaches zero within the record time of the FADC. Therefore, for small pulses, this method frequently finds bias, which results in the peak at the end of the FADC record.

The broad distribution with higher thresholds can be understood due to the statistical character of the pulse heights.

6.4.4 Integral minimum position

The distribution of signal ends calculated by finding the integral minimum position is shown in figure 6.11. This method is expected to find the time, where the threshold $U_{\text{th}} = 0\,\text{V}$ is overshot *for the first time*. Only larger pulses after that first overshooting

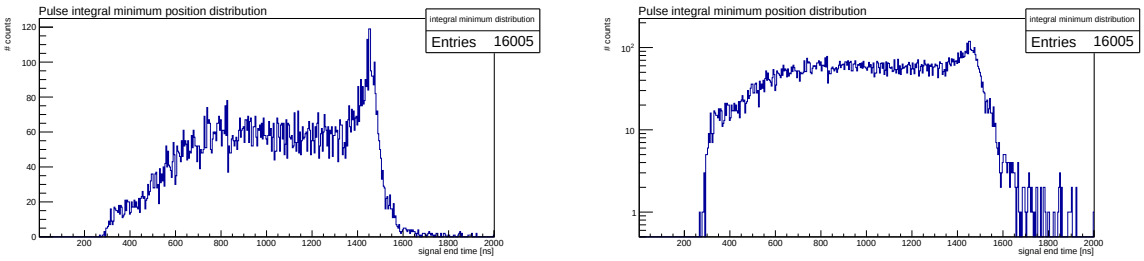

(a) linear scale

(b) logarithmic scale

Figure 6.11: Signal end found using the timeposition of the integral minimum. This shows a broad distribution with a peak near the maximum drift time.

have sufficient contributions to the integral to shift its *global minimum* to later times[2]. This can be seen, when comparing figures 6.1 and 6.3(a). Here, small pulses after the first time overshot of the threshold 0 V are not sufficient to shift the *global* minimum. Thus, this method is more robust against afterpulses and bias.

This distribution is comparable to the results obtained in figure 6.9. However, this peaks near the maximum drift time. The distribution of pulses is random, however, the first time, a threshold of 0 V can be undershot can be *at last* at the maximum drift time. This way, the peak at the end can be understood.

6.4.5 Correlation between signal end finding methods

The above-mentioned methods to find the signal end should result in similar results. Figure 6.12 shows a correlation plot of the pulse end (at $U_{\text{th}} = -146\,\text{mV}$) and the integral minimum position methods to find the signal end. The color-scale indicates the number of events at a specific point in the plot. They show a correlation, stating that both methods yield comparable results. The same plot, comparing the integral minimum time with the pulse end time at a threshold of $U_{\text{th}} = -0\,\text{mV}$ is shown in figure 6.13. Here, a peak at the maximum drift time is present. Ideally, both methods should result in the *maximum drift time*. As stated above, the integral minimum method typically finds the first time, where the voltage drops to zero and small pulses after that time don't shift the global minimum. On the other hand, the pulse end method finds the last time, the voltage drops to zero. Due to the long maximum drift time, the pulses from different clusters are distinguishable (see fig. 6.1). For geometrical reasons, later clusters typically have smaller signal heights. As the integral minimum method is more sensitive to larger pulses, its distribution is wider for this gas mixture. On the other hand, it is less sensitive to bias or afterpulses and does not show entries after the maximum drift time.

[2]because than the voltage is shifted to small positive values and the integral rises again

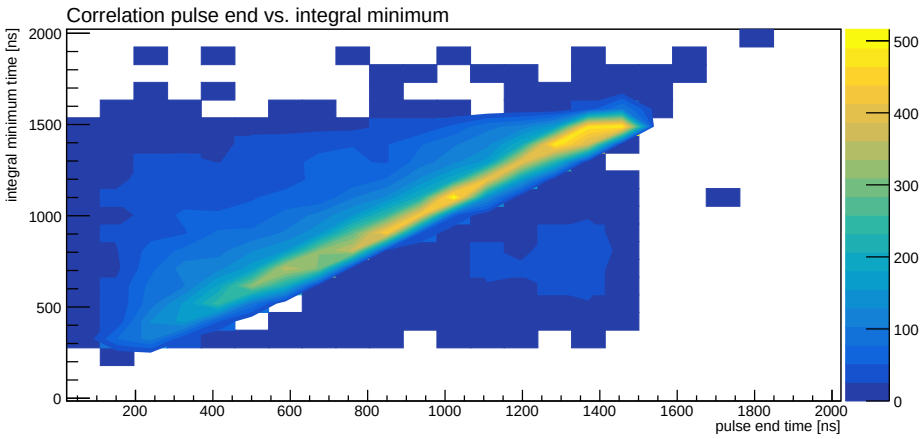

Figure 6.12: Correlation between the signal end found by finding the last bin containing a voltage lower than a threshold of $U_{\text{th}} = -146\,\text{mV}$ and the time, where the integrated voltage pulse has its minimum.

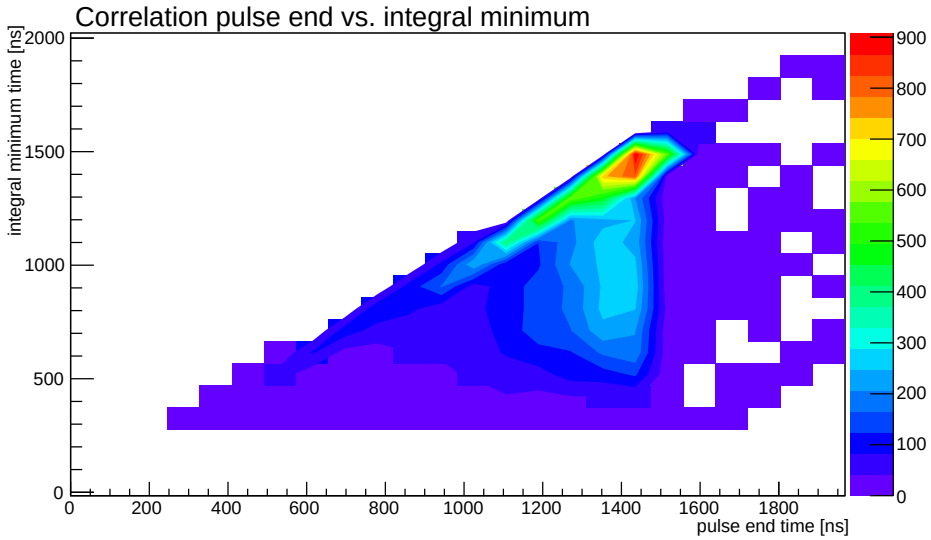

Figure 6.13: Correlation between the signal end with $U_{\text{th}} = -0\,\text{mV}$ and the integral minimum.

6.5 *rt*-relation

By integrating the drift time spectrum and proper scaling, the *rt*-relation can be calculated, as described in equation (3.21), the result is shown in figure 6.14. This *rt*-relation is non-linear. A more linear *rt*-relation is benefitial, as the drift velocity then becomes independent on the electric field and less negative effects on the spatial resolution of a drift tube setup are present.

In order to check the linearity, a linear function $f(t) = at$ is introduced. Here, $a = \frac{r_{\text{tube}}}{t_{\text{max}}}$ is the slope needed for a linear function from $r = 0$ to $r = r_{\text{tube}}$. A plot of the linear function $f(t)$ and the *rt*-relation is shown in figure 6.15. The linear function depends on

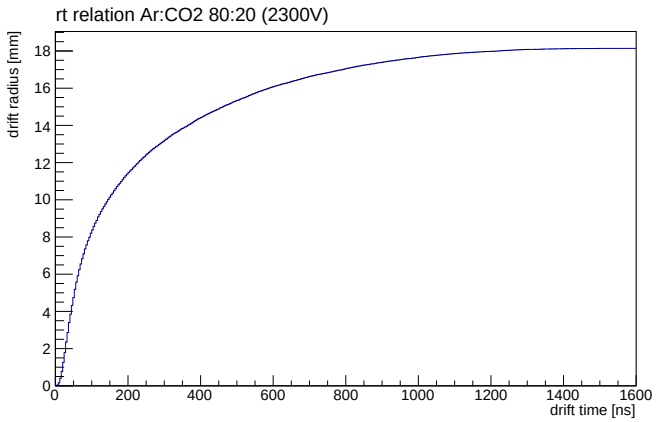

Figure 6.14: *rt*-relation for Ar:CO_2 80:20. The *rt*-relation is computed with equation (3.21) by integrating the drift time spectrum. Note that the *rt*-relation is non-linear and converges to a maximum radius of $r = r_{\text{tube}} = 18.15$ mm.

the maximum drift time. Here, the time $t_{\max}$ is determined using the method described in chapter 6.4.2. A measure for the linearity of the *rt*-relation is achieved by performing a

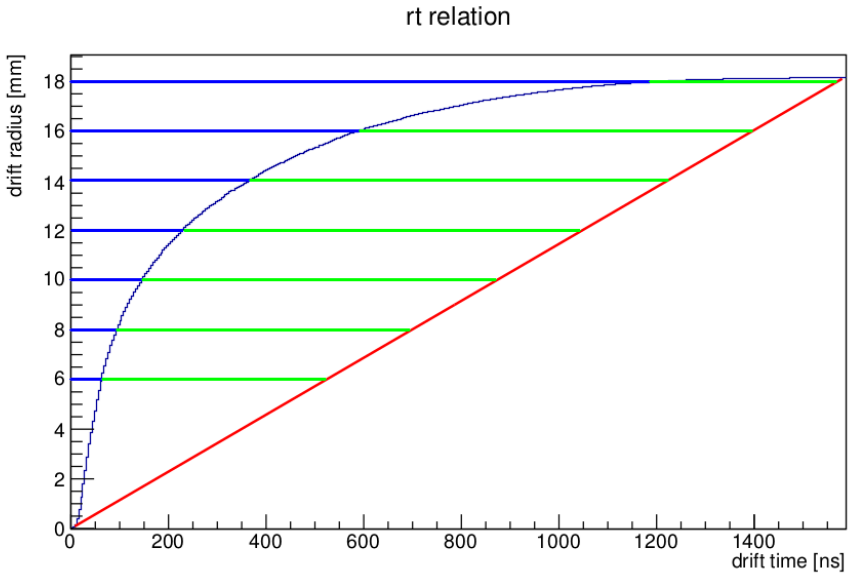

Figure 6.15: *rt*-relation for Ar:CO_2 80:20 with a linear function (red) that shared the start and endpoint of the *rt*-relation. The drift radius axis is subdivided into 181 bins of 100 μm width, on each of those bins, the difference between the linear function and the actual *rt*-relation (green) is calculated and divided by the drift time, this event would have considering a linear *rt*-relation (green + blue). Not all bins are shown in this illustration.

χ^2-test with the zero-hypothesis of a linear behavior. For that purpose, the *radius axis* is subdivided into bins of 100 μm width. Now, the sum of squared differences for the inverse

functions $t(r)$ and $f^{-1}(r)$ is computed as shown in equation (6.3).

$$\chi^2 = \sum_r \frac{(f^{-1}(r) - t(r))^2}{t(r)} \tag{6.3}$$

An illustration of the method to calculate the deviation from linearity of the rt-relation is shown in figure 6.15

The χ^2 is then divided by the *number of degrees of freedom (ndf)*, which, due the binning of the radius axis, is 181. The test results in a value

$$\frac{\chi^2}{\text{ndf}} = 401.21 \tag{6.4}$$

6.6 Efficiency

The efficiency η can be calculated following equation (3.22). The number of triggered events is shown as the number of entries in figure 6.6. The number of events, where no drift time was found is given as the number of *underflow* events. The difference then is the number events, detected by the drift tube.

The efficiency can now be calculated to:

$$\eta = \frac{17096 - 1064}{17096} \approx 0.937 \pm 0.002 \tag{6.5}$$

Again, for future research with an experimental setup suited for tracking, more detailed studies on the efficiency can be performed. For example, the efficiency as a function of the tube's radius could then be analyzed.

6.7 Afterpulses

In order to have a quantitive measure of the probability for afterpulsing, a criteria for an afterpulse needs to be defined. Here, an afterpulse is counted if the threshold voltage $U_{th} = -146$ mV is undershot after the maximum drift time. The detection of afterpulses heavily depends on precise knowledge of the maximum drift time. The before-mentioned method of finding the maximum drift time by fitting a linear function to the end of the drift time spectrum, showed large errors. The probability P_a for an afterpulse is computed via:

$$P_a = \frac{N_{\text{afterpulses}}}{N_{\text{events}}} \tag{6.6}$$

Assuming a Poissonian distribution of afterpulses, the error σ_{P_a} is calculated as shown in (6.7).

$$\sigma_{P_a} = \sqrt{\frac{N_{\text{afterpulses}}}{N^2_{\text{events}}} + \frac{N^2_{\text{afterpulses}} N_{\text{events}}}{N^4_{\text{events}}}} \tag{6.7}$$

For this drift gas mixture, a probability for afterpulsing of

$$P_a = (0.20 \pm 0.04)\%$$

was computed.

6.8 Discussion of errors

Multiple systematic errors are present in the presented measurements. Concerning the drift tube itself, due to its short length and complete trigger area coverage, edge effects reducing the electric field strength near the end caps of the drift tube, can not be neglected. An analysis of the drift time spectrum with the scintillators covering only a small part of the drift tube in its center, is shown in figure 6.16. However, this scintillator setup was not used for practical reasons, as it leads to significantly lower trigger efficiency, resulting in the need for an ineligibly long data acquisition.

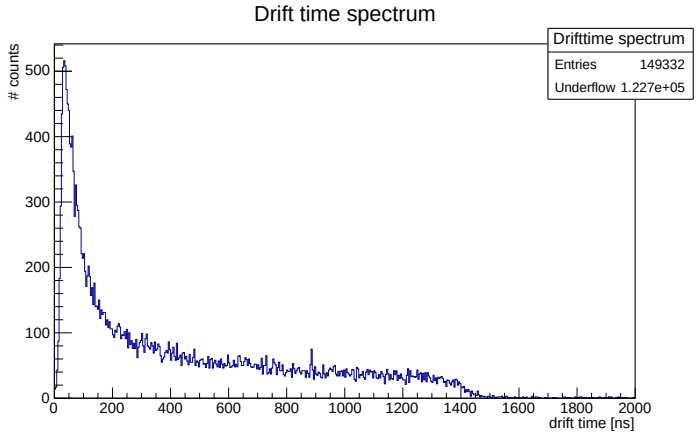

Figure 6.16: Drift time spectrum for Ar:CO_2 80:20 with the scintillators just covering a small part in the center of the drift tube along its whole diameter. With this setup, edge effects, reducing the effective field strength along the tube's radius, can be neglected. This drift time spectrum shows the well known *shoulder*. Therefore it is shown than edge effects are a major contribution to the systematic error in all other measurements. Due to the limited amount of time available for measurements, the before-mentioned trigger setup with edge effects contributing is chosen since, using this setup, the efficiency is unsuitably low. This results in the need for too long data acquisition.

The drift time spectrum, shown in figure 6.16 shows a smaller maximum drift time compared to the one shown before. It can be assumed, that this offset is present in all further measurements. Thus any maximum drift time presented in the following is expected to be an *over-estimation*. However, as all measurements are performed using the same test setup, these offsets cancel out when comparing the measurements with each other.

This spectrum, which is computed at the same threshold voltage as before, has a relatively high rate of counts after the shoulder. A possible explanation of that feature is that the scintillators are placed over the housing for a radioactive source, thus in a region, where a significant charge was deposited on the sense wire. This might have resulted in higher influence of aging effects in that region, which needs to be investigated in further research. The drift time spectrum is computed using a threshold voltage of $U_{\mathrm{th}} = -146$ mV. As lower values do not influence the shape, but only the efficiency of the drift time spectrum, higher values lead to distortions. This can be described with an electromagnetic bias coupling into the signal cables. The laboratory does not provide electromagnetic shielding and is situated just a few meters off the *PETRA* synchrotron, which is considered to be a source of electromagnetic bias.

An *estimation of the systematic error* can be achieved by dividing the drift time spectrum with the scintillators at the tube's center by the drift time spectrum described earlier. A plot of the resulting spectrum is shown in figure 6.17. The range in that the

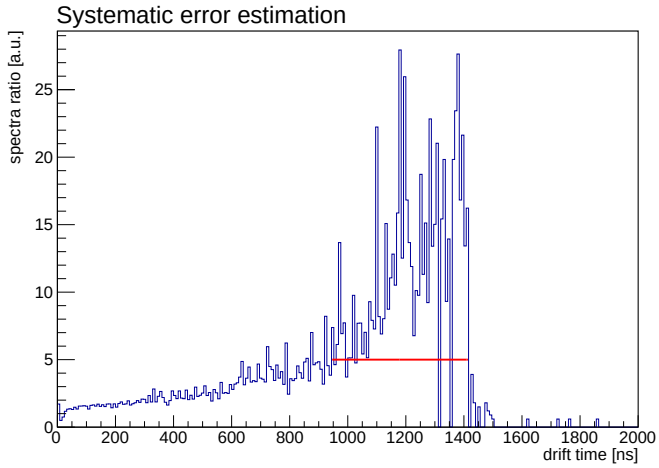

Figure 6.17: An estimate of the systematic error by dividing the spectrum shown in figure 6.16 by the one shown in 6.6. The range, where the first one is a factor 5 larger than the latter spectrum is indicated with the red line.

distribution differ by a factor 5 is 480 ns long. The drop for drift times greater than 1400 ns is a *numerical error.* If one of the two spectra has zero entries for a bin, zero is found, which is an error. It is expected, that the distribution shown in figure 6.17 is wider than shown here, resulting in an even larger systematic error.

Another source of errors is the electronic amplifier. For future research, additional measurements using a voltage-amplifier should be used. Additionally, the amplifier shows saturation for large pulses[3]. This contributes to an error of the gas amplification.

[3]shown in chapter 7.1

7 Studies with different drift gas mixtures

Using the methods described in the previous chapter, a set of different drift gas mixtures is studied. Among those drift gas mixtures, two mixtures of Argon and Carbondioxide and four mixtures that have additional admixtures of Nitrogen are investigated. In particular, the following drift gas mixtures are studied:

1. Ar:CO_2 90:10
2. Ar:CO_2 93:7
3. Ar:CO_2:N_2 96:2.5:1.5
4. Ar:CO_2:N_2 96:3:1
5. Ar:CO_2:N_2 96:3.5:0.5
6. Ar:CO_2:N_2 97:2:1

The examination of those drift gas mixtures is motivated by results, described in [79], for the *Monitored-Drift-Tubes* of the muon spectrometer of the *ATLAS* experiment. There, drift gas mixtures with admixtures of Nitrogen of approximately 1% showed a short maximum drift time as well as a linear rt-relation. The drift tubes of the ATLAS experiment, however, are operated at a pressure of 3 bar, it must be tested if the results achieved in [79] can be reproduced at an atmospheric pressure.

7.1 Gas amplification

With too high gas amplification, the drift tube can be damaged due to sparks. It is not known, how high the gas amplification for the new drift gas mixtures. For security reasons, the high voltage is slowly raised from a safe voltage. The gas amplification is not measured in absolute units, as described above. However, as every gas mixture is studied using the same experimental setup and conditions, a relative measurement of the gas amplification is sufficient. A measure for the gas amplification is the charge in a voltage pulse, which can be determined by integrating the current on the signal wire. As no absolute measure is needed here, the voltage pulses are integrated, their average

minimum height is being compared to the corresponding value for the known gas mixture of Ar:CO_2 80:20. For each tested drift gas mixture, after flooding the tube for a sufficient amount of time, the high voltage is slowly raised, monitoring the drift tube's signals with an oscilloscope. When pulses become visible on the oscilloscope screen the high voltage is fixed and a measurement using the FADC for 24 hours is performed. When analyzing the data, the average minimum height of the integrated voltage pulses is now compared to that of the reference gas Ar:CO_2 80:20. If the latter one is higher, the high voltage is raised and the measurement is repeated.

Any results presented in the following text is computed for a gas amplification comparable to that of Ar:CO_2 80:20 at $U_{\mathrm{HV}} = 2300$ V. No studies on the dependence of high voltage are performed. In the following, the amplification of the gas mixture Ar:CO_2:N_2 97:2:1 is about 20% lower than any other presented gas mixture. This is due to the high pulses of that gas mixture, where the amplifier saturates. An example of a pulse with saturation of the amplifier is shown in figure 7.1.

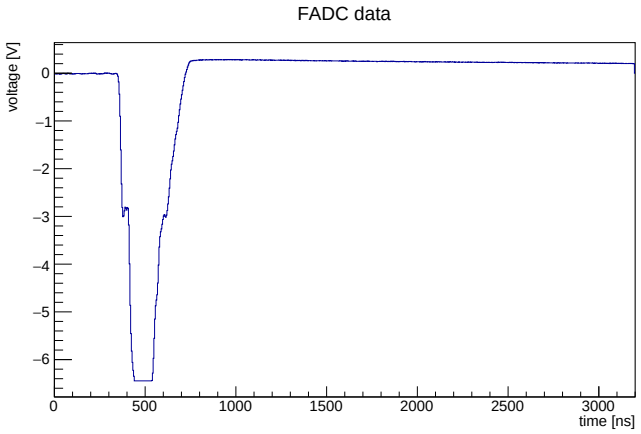

Figure 7.1: Example of an event with amplifier saturation. This is a voltage pulse for Ar:CO_2:N_2 97:2:1. When a high number of events has sufficiently high pulses to result in amplifier saturation, the integral results in wrong values. Thus, the amplification is under-estimated. Therefore, for this special gas mixture, a lower high voltage was chosen for security reasons.

7.2 Spectra of drift times with different gases

Using the method described in chapter 6.3, for each studied drift gas mixture, drift time spectra were calculated. For better comparability, the scaling on the time axis will be the same as for Ar:CO_2 80:20 for each shown gas. The drift time spectra of all tested drift gas mixtures are shown in figure 7.2. Here, in order to maintain comparability, the scaling is the same as for the reference gas Ar:CO_2 80:20. The shapes of the drift time spectra do not differ largely with the applied high voltage. Only the drift time spectra are shown, where the gas amplification is comparable to that of the reference gas.

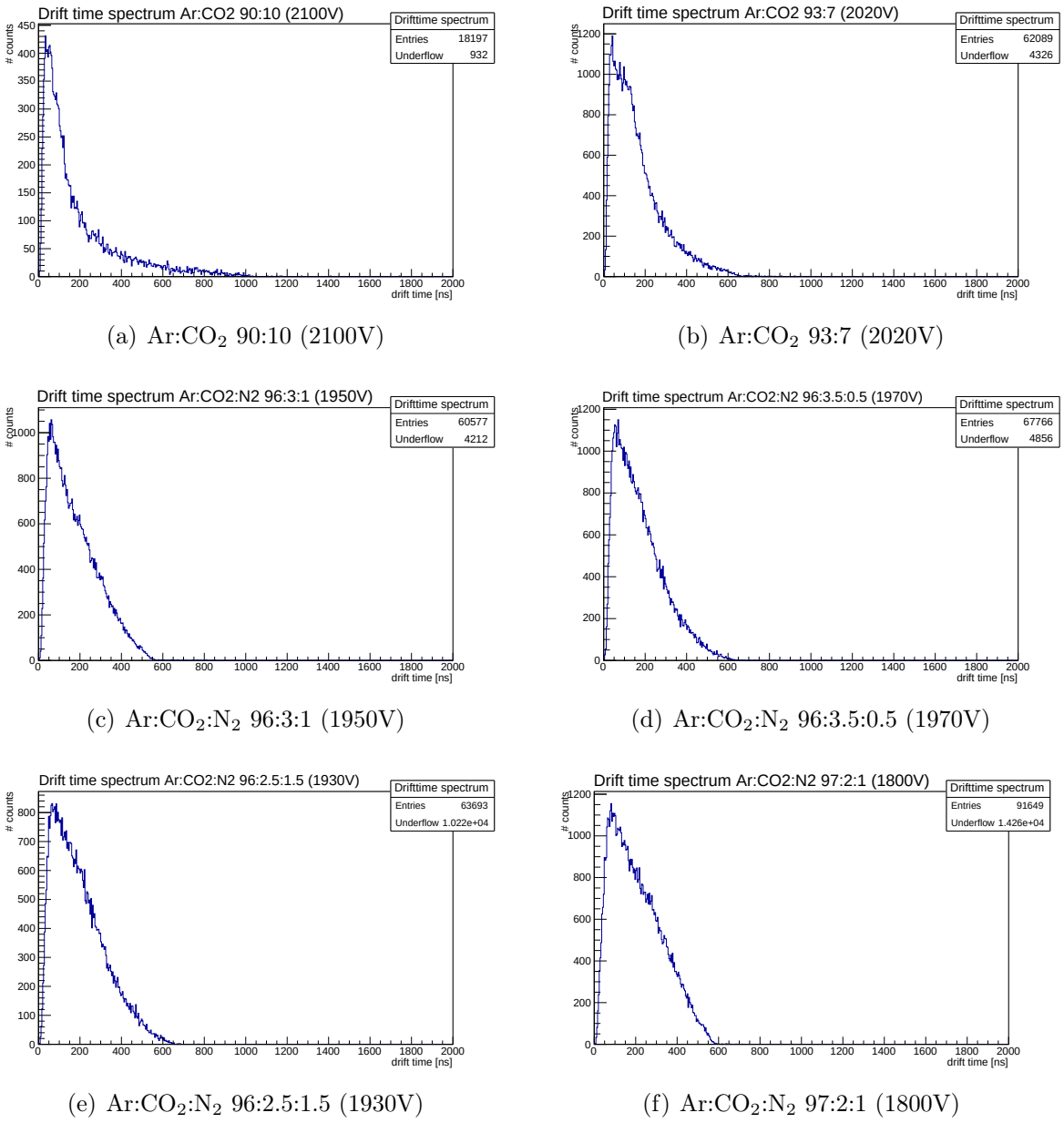

(a) Ar:CO_2 90:10 (2100V)

(b) Ar:CO_2 93:7 (2020V)

(c) Ar:CO_2:N_2 96:3:1 (1950V)

(d) Ar:CO_2:N_2 96:3.5:0.5 (1970V)

(e) Ar:CO_2:N_2 96:2.5:1.5 (1930V)

(f) Ar:CO_2:N_2 97:2:1 (1800V)

Figure 7.2: Drift time spectra for different drift gas mixtures. For each drift gas mixture, the spectrum for only one high voltage is shown. The shape of the drift time spectrum does not change significantly with the applied high voltage. The maximum drift time, however, is expected to decrease with increasing high voltage.

7.2.1 Maximum drift time

The maximum drift time, in order to maintain comparability between different drift gas mixtures, is again computed using a linear fit to the end of the drift time spectrum. Finding the root of the fit results in the maximum drift time $t_{\mathrm{drift,max}}$. Its error is calculated using the Gaussian propagation of errors. An example of a linear fit to the end of the drift time spectrum for the gas mixture Ar:CO_2:N_2 96:2.5:1.5 is shown in figure 7.3. The

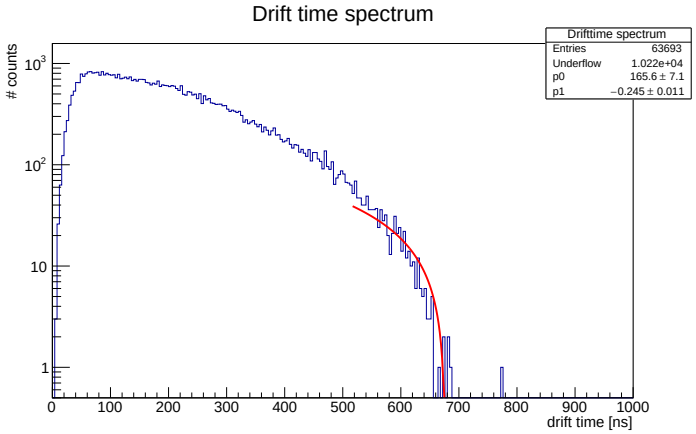

Figure 7.3: Linear fit (red) to the end of the drift time spectrum of Ar:CO_2:N_2 96:2.5:1.5.

results a summarized in table 7.1.

Table 7.1: Maximum drift times as computed using two methods. The time $t_{\mathrm{drift,max}}$ is found by fitting a linear function to the signal end and calculating its root . The error is computed using the Gaussian propagation of errors (3.23). The time $t_{\mathrm{max,int}}$ is computed using an empirical method, using the integration method described in chapter 6.4.2. Note that these methods result in comparable times, due to its empirical definition, an error estimation would not be meaningful.

Ar ($\%_{\mathrm{vol}}$)	CO_2 ($\%_{\mathrm{vol}}$)	N_2 ($\%_{\mathrm{vol}}$)	U_{HV} (V)	$t_{\mathrm{drift,max}}$ (ns)	$\sigma_{t_{\mathrm{drift,max}}}$ (ns)	$t_{\mathrm{max,int}}$ (ns)
90	10	0	2100	1168	200	1112
93	7	0	2000	756	90	820
96	2.5	1.5	1930	717	61	648
96	3	1	1950	635	51	628
96	3.5	0.5	1970	694	67	624
97	2	1	1800	661	64	584

7.3 Signal end distributions

For the tested drift gas mixtures with admixtures of Nitrogen, the positions of the pulse end and the integral minimum show a different behavior than what was described for the reference gas, Ar:CO_2 80:20. Here, both distribution show a peak near the maximum drift time, correlation plots for Ar:CO_2:N_2 96:3:1 are shown in figure 7.4. The threshold voltage for the pulse end method is $-146\,\mathrm{mV}$. The different behaviour compared to the reference gas can be understood with the lower amount of CO_2 in the gas. In the low electric field at the cathode, electrons from ionizations are slowly accelerated. The electronegative CO_2 has enough time here to capture free electrons. A lower amount of CO_2 leads to

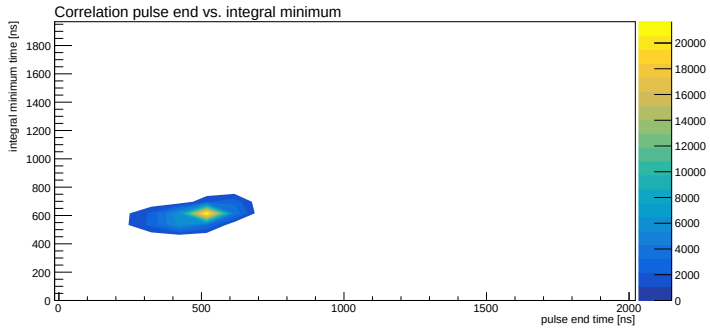

(a) pulse end and integral minimum

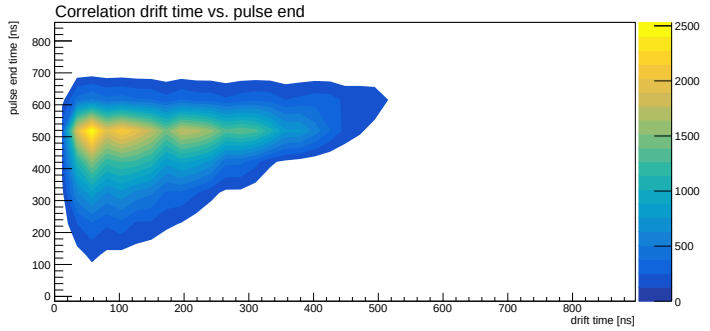

(b) pulse end and drift time

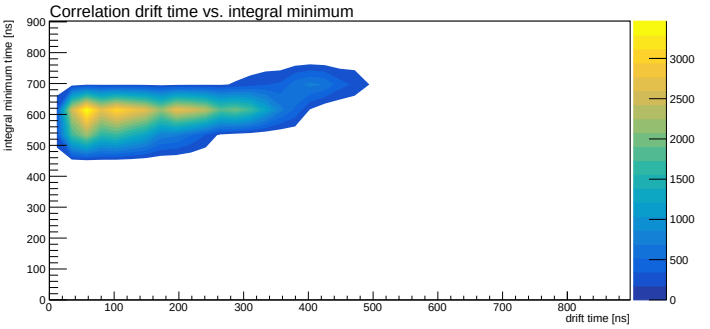

(c) integral minimum and drift time

Figure 7.4: Correlation between pulse end and integral minimum for Ar:CO_2:N_2 96:3:1. This shows a significant difference from the corresponding plot for Ar:CO_2 drift gas mixtures, as for gas mixtures with additions of Nitrogen, both of these measures for the signal end correspond the maximum drift time, independent of the measured drift time for a specific event.

higher pulses from clusters at the cathode and the integral minimum method becomes more effective. This is shown in figure 7.6, where correlations of both methods to the maximum drift time are shown for decreasing amounts of CO_2 in the drift gas mixture. In addition, due to the faster signal development, the signals of different clusters overlap each other. Thus, for a typical pulse the voltage does only drop to zero once per event Two examples of voltage pulses with a gas mixture of Ar:CO_2:N_2 96:3:1 at a high voltage of 1950 V are shown in figure 7.5. Therefore, both methods result in the same time.

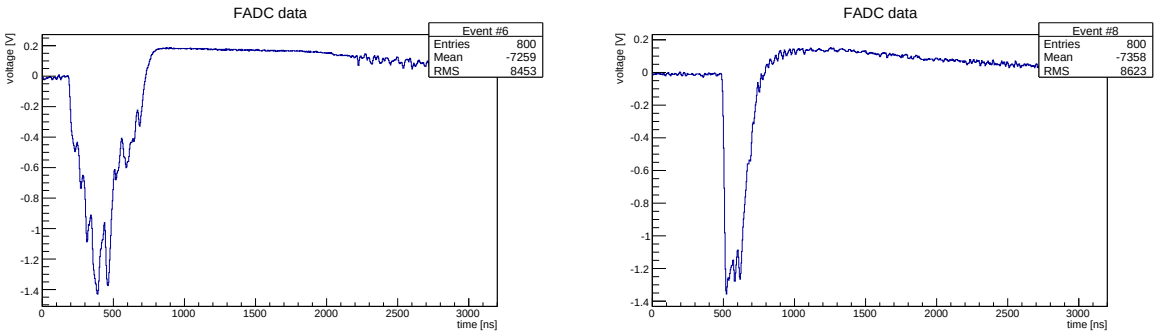

(a) Voltage pulse of event with short drift time

(b) Voltage pulse of event with long drift time

Figure 7.5: Representative voltage pulses for Ar:CO_2:N_2 96:3:1 at $U_{HV} = 1950\,V$. These show a difference to the reference gas. The single pulses due to different clusters overlap and only pulse can be seen.

Both methods over-estimate the maximum drift time, as the drift time corresponds to the falling edge of a pulse and both of these methods correspond to the rising edge of a pulse.

This hints to a possbible method for triggerless readout of drift tube detectors[1].

[1]for a more detailed study of this topic see [74]

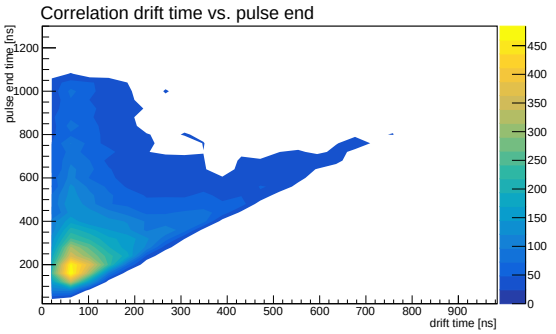

(a) drift time vs. pulse end for Ar:CO_2 90:10

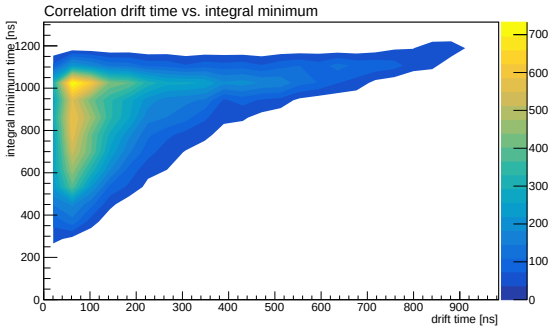

(b) drift time vs. integral for Ar:CO_2 90:10

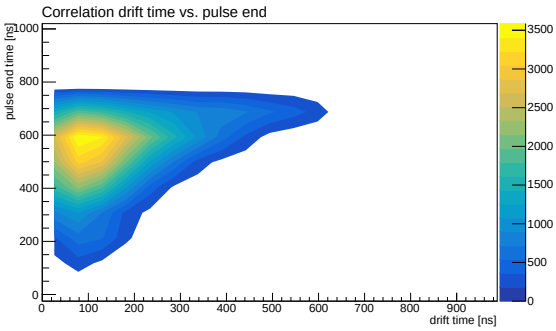

(c) drift time vs. pulse end for Ar:CO_2 93:7

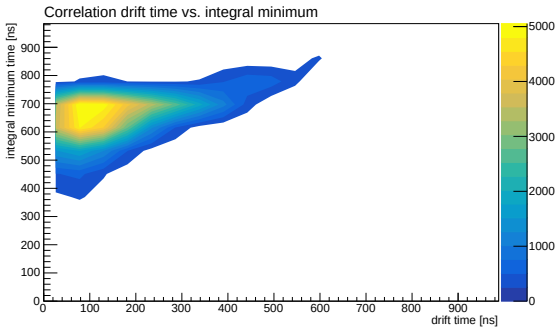

(d) drift time vs. integral for Ar:CO_2 93:7

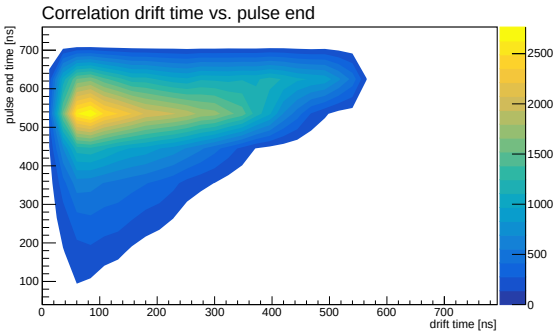

(e) drift time vs. pulse end for Ar:CO_2:N_2 97:2:1

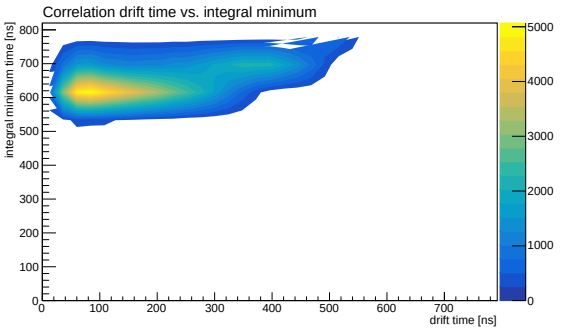

(f) drift time vs. integral for Ar:CO_2:N_2 97:2:1

Figure 7.6: Correlation between drift time and signal end for decreasing amounts of CO_2 admixtures to the drift gas mixture. For each gas mixture, the signal end is found by the pulse end method (left column) at $U_{\text{th}} = -146\,\text{mV}$ and integral minimum (right column). For Ar:CO_2 90:10 the pulse end method (7.6(a)) shows a different behavior than all other displayed gas mixtures, as the probability for clusters near the cathode wall is lower here, than for higher amounts of Argon.

7.4 *rt*-relations

The *rt*-relations for the drift gas mixtures shown in figure 7.2 are computed using (3.21). How the *rt*-relation is achieved is described in chapter 6.5. Figure 7.7 shows the *rt*-relations for all tested drift gas mixtures.

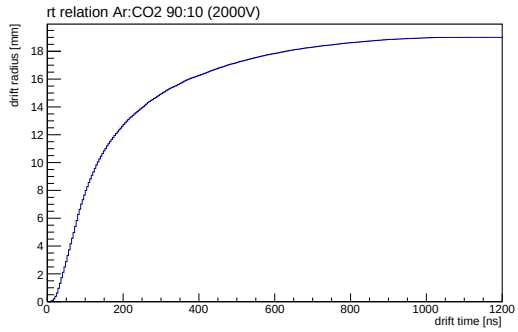

(a) Ar:CO_2 90:10

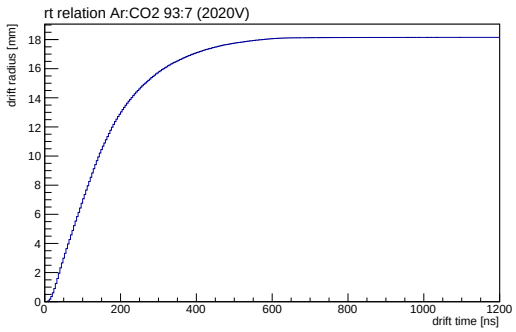

(b) Ar:CO_2 93:7

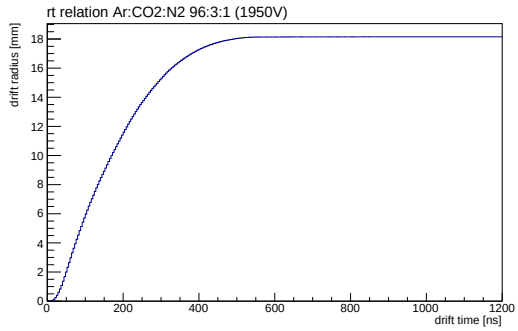

(c) Ar:CO_2:N_2 96:3:1

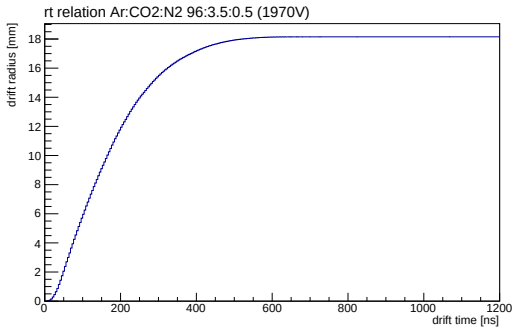

(d) Ar:CO_2:N_2 96:3.5:0.5

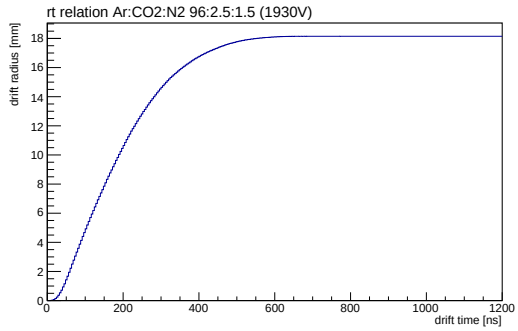

(e) Ar:CO_2:N_2 96:2.5:1.5

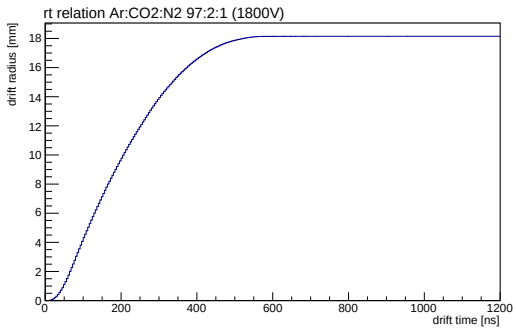

(f) Ar:CO_2:N_2 97:2:1

Figure 7.7: *rt*-relations for different drift gas mixtures. The *rt*-relations are computed using equation (3.21) by integrating the drift time spectra shown in figure 7.2, each plotted in the same scale.

7.4.1 *rt*-relation linearity

The linearity of the tested drift gas mixtures' *rt*-relations is computed with the χ^2-test as described in chapter 6.5. It can be seen that the drift gas mixtures containing Nitrogen are more linear than mixtures without Nitrogen. The most linear and fast mixture identified is Ar:CO_2:N_2 97:2:1. The drift gas mixture Ar:CO_2:N_2 96:3:1 showed good values for maximum drift time as well as linearity.

Table 7.2: Linearity of the rt-relations for different drift gas mixtures tested with a χ^2-test. Values closer to 1 represent most linear rt-relations.

Ar ($\%_{vol}$)	CO_2 ($\%_{vol}$)	N_2 ($\%_{vol}$)	χ^2/ndf
80	20	0	401.21
90	10	0	250.925
93	7	0	158.478
96	2.5	1.5	89.8397
96	3	1	58.8447
96	3.5	0.5	59.7528
97	2	1	26.8119

7.5 Detection efficiency

The detection efficiency is calculated using equation (3.22) for every tested drift gas mixture and every high voltage applied to the sense wire for a specific drift gas mixture. The result is plotted in figure 7.8. Note that the drift gas mixture Ar:CO_2:N_2 96:2.5:1.5 is not included. During the measurements with that mixture, due to a false adjustment of the gas flow, the gas supply ran out, dramatically influencing the measured efficiency. The detected events were sufficient, however, in order to determine the drift time spectrum for this gas mixture. Note that all drift gases offer detection efficiency comparable to the

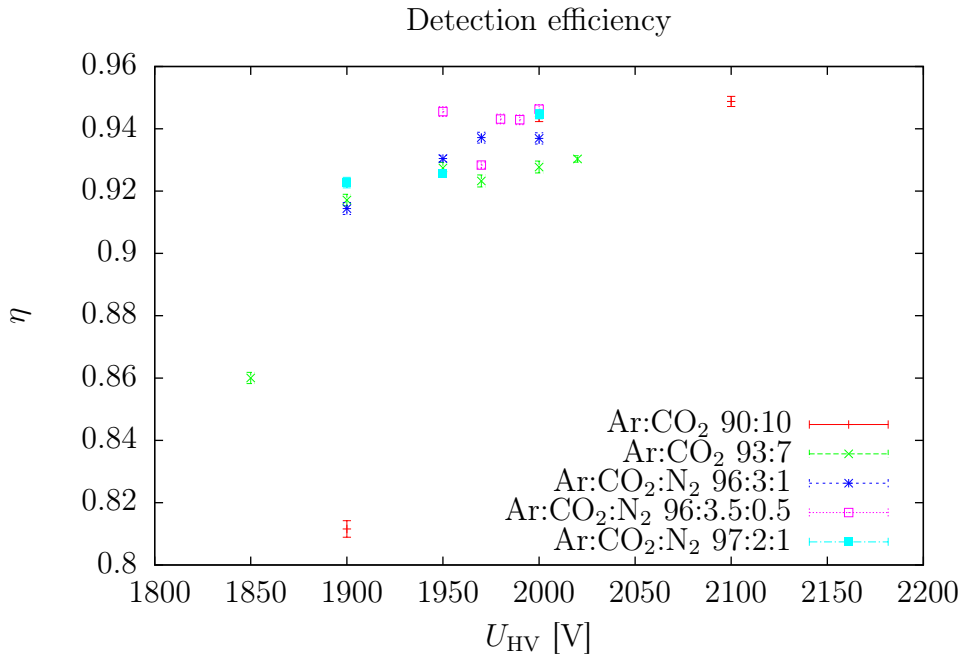

Figure 7.8: Efficiency for different gas mixtures depending on the high voltage applied to the sense wire

efficiency of the mixture used as reference. The efficiency, however, is lower than expected for a drift tube detector. Possible explanations for this observation are aging effects, as the drift tube was stored without being filled with a protection gas for a long time. In addition, the threshold voltage of the PMTs in used for triggering was not optimized for efficiency. Further studies on maximum achievable efficiency are recommended. In earlier experiments using OPERA-type drift tubes, a higher efficiency was measured for Ar:CO_2 80:20 at atmospheric pressure. The efficciecies presented here thus can be expected to be an under-estimation. The efficiencies for all drift gas mixtures except Ar:CO_2:N_2 with a gas gain comparable to that of the reference measurement are summarized in table 7.3.

Table 7.3: Detection efficiency for different drift gas mixtures.

Ar	CO_2	N_2	η
80	20	0	0.937 ± 0.002
90	10	0	0.949 ± 0.002
93	7	0	0.928 ± 0.002
96	3	1	0.930 ± 0.001
96	3.5	1.5	0.928 ± 0.001
97	2	1	0.92 ± 0.002

7.6 Afterpulsing studies

Afterpulses are being counted for every triggered event using an algorithm similar to finding the drift time. Multiple afterpulses per event *are allowed*. As it showed for every tested drift gas mixture, events with multiple afterpulses are very rare.

Table 7.4: Probability $P_{\text{afterpulse}}$ for afterpulses for different drift gas mixtures. An afterpulse is counted, if the threshold voltage $U_{\text{th}} = -146$ mV is undershot *after the maximum drift time* $t_{\max}$. The maximum drift time is computed using the method described in chapter 6.4.2. The error $\sigma_{P_{\text{afterpulse}}}$ is computed using equation 6.7.

Ar ($\%_{\text{vol.}}$)	CO_2 ($\%_{\text{vol.}}$)	N_2 ($\%_{\text{vol.}}$)	$t_{\max}$ (ns)	$P_{\text{afterpulse}}$ (%)	$\sigma_{P_{\text{afterpulse}}}$ (%)
80	20	0	1584	0.20	0.03
90	10	0	1112	0.30	0.04
93	7	0	820	1.35	0.08
96	2.5	1.5	648	2.11	0.06
96	3	1	628	0.83	0.03
96	3.5	0.5	624	4.58	0.08
97	2	1	584	8.30	0.10

The drift gas mixture Ar:CO_2:N_2 97:2:1, which is fast and linear shows a significantly higher probability for afterpulses than all other tested drift gas mixtures. Among the other tested drift gas mixtures containing admixtures of Nitrogen, the mixture **Ar:CO_2:N_2 96:3:1** shows the lowest probability while being fast and with a good linearity as well. Consequently, this drift gas mixture seems the most promising candidate.

7.7 Performance of Ar:CO_2:N_2 96:3:1

The most promising drift gas mixture for future experiments using drift tubes from the OPERA experiment is Ar:CO_2:N_2 96:3:1. For this mixture, a more detailed look at the signal ends is given. Figure 7.9 shows the distribution of signal end positions found by using the position of the minimum of the pulse integrals. This shows, that this gas mixture

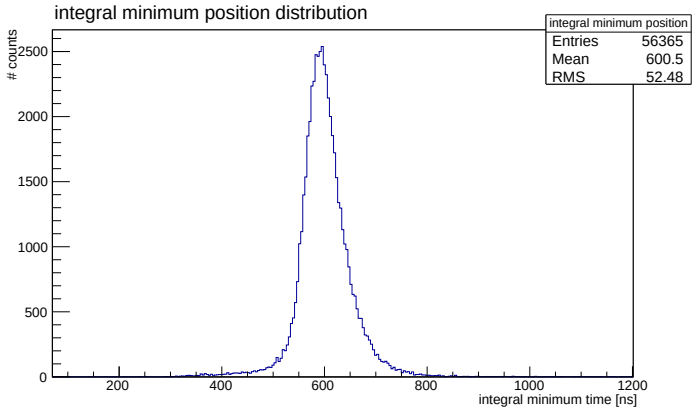

Figure 7.9: Distribution of integral minimum position for Ar:CO_2:N_2 96:3:1. This distribution seems not to follow a Gaussian distribution.

might be suitable for a triggerless readout as the pulse ends correspond to the maximum drift time.

The distribution of pulse ends by finding the last filled bin, exceeding a threshold voltage of -146 mV is shown in figure 7.10. While this is robust against bias due to the *high* threshold, it has a larger error on the maximum drift time. The pulse end method applied with a threshold of zero is shown in figure 7.11. This method shows a large second peak, which is again due to bias. Summarizing these results, the pulse end method can be used with higher thresholds than for the reference gas. The integral minimum position method remains more robust to bias and afterpulses.

The distribution of integral minimum positions as shown in figure 7.9 has an arithmetic mean of 600 ns and an RMS of 52 ns. This is again an estimate of the maximum drift time for this gas mixture and might hint to the ability for triggerless readout. This is studied in [74].

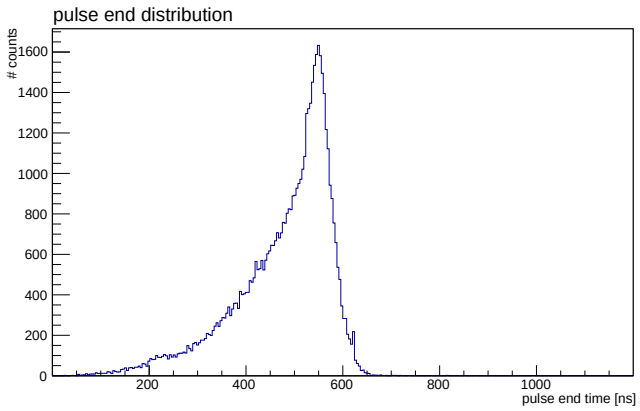

Figure 7.10: Distribution of pulse ends for Ar:CO_2:N_2 96:3:1 achieved by finding the last time, a threshold voltage of $-146\,\mathrm{mV}$ is exceeded.

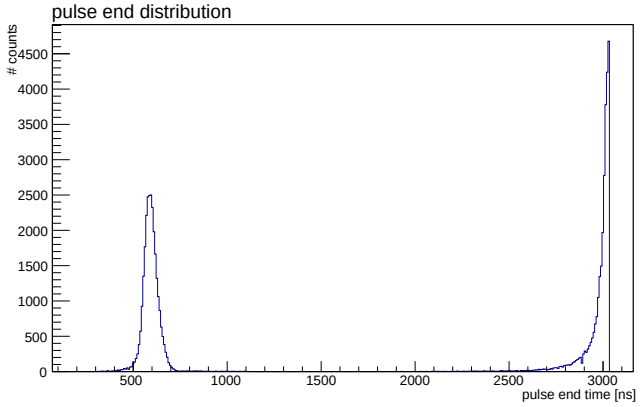

Figure 7.11: Pulse end distribution for Ar:CO_2:N_2 96:3:1 with $U_{\mathrm{th}} = 0\,\mathrm{mV}$. The first peak looks similar to the peak obtained with the integral minimum method. The second peak due to bias is much higher than for the reference gas. This can be understood with the short maximum drift time of this gas mixture. The capictor in the amplifier can discharge for most events as the FADC record time is long enough. When the amplitude of the bias is larger than the voltage offset due to the capacitor, bias is counted at the end of the FADC record.

7.8 Summary

Different drift gas mixtures were studied regarding their maximum drift time, the linearity of their rt-relation and the probability of afterpulses. Table 7.5 summarizes the experimental results. A good candidate for a linear and fast drift gas mixture with a low probability for afterpulsing is Ar:CO_2:N_2 96:3:1.

Table 7.5: Summary of the experimental results. $t_{\text{drift,max,fit}}$ is the maximum drift time computed by a linear fit to the end of the drift time spectrum as described in chapter 6.4.1, $t_{\text{drift,max,int}}$ is the time, after which a pulse is counted as afterpulse. The empirical method of obtaining that time is described in 6.4.2.

Ar	CO_2	N_2	U_{HV} (V)	$t_{\text{drift,max,fit}}$ (ns)	$t_{\text{drift,max,int}}$ (ns)	$P_{\text{afterpulse}}$ (%)	χ^2/ndf
80	20	0	2300	1565 ± 302	1584	0.20 ± 0.03	401.21
90	10	0	2100	1168 ± 200	1112	0.30 ± 0.04	250.925
93	7	0	2000	756 ± 90	820	1.35 ± 0.08	158.478
96	2.5	1.5	1930	717 ± 61	648	2.11 ± 0.06	89.8397
96	3	1	1950	635 ± 51	628	0.83 ± 0.03	58.8447
96	3.5	0.5	1970	694 ± 67	624	4.58 ± 0.08	59.7528
97	2	1	1800	661 ± 64	584	8.30 ± 0.10	26.8119

8 Conclusion and outlook

In this thesis, drift gas mixtures containing Argon, Carbon dioxide and Nitrogen were studied at atmospheric pressure regarding their maximum drift time as well as their rt-relation, especially its linearity. For that purpose, in a test setup of one shortened OPERA drift tube, the electronically amplified voltage signal on the sense wire was measured using a *FADC* and then analyzed. First a well-known drift gas mixture of Ar:CO_2 80:20 was examined. All subsequently tested drift gas mixtures were then compared to this *reference gas*. A maximum drift time of

$$t^{\text{ref}}_{\text{drift,max}} = (1565 \pm 302)\,\text{ns}$$

was found. This is compatible with results found in earlier experiments using drift tubes of the same type and the same drift gas mixture. The large uncertainty can be explained with the scintillators, used as external trigger, covering the whole area of the drift tube, thus edge effects near the tube's ends cannot be neglected. The rt-relation was calculated and tested for its linearity using a χ^2-test. It shows a $\chi^2/\text{ndf} = 401.21$, which is a significant deviation from linearity.

Additionally, methods for finding the end of a voltage pulse as well as the maximum drift time were studied. Two methods in particular were investigated giving the end of a voltage pulse. However, in the case of Ar:CO_2 80:20, due to the low primary ionization density, both of those methods do not correlate with the maximum drift time.

Motivated by simulations of different drift gas mixtures, as well as the results of measurements presented in [79], several drift gas mixtures were studied. Among those are different mixing ratios of Argon and Carbon dioxide as well as drift gas mixtures of the two before-mentioned gases with admixtures of $0.5\% - 1.5\%$ Nitrogen. Those hat previously been found to be fast and linear at a pressure of 3 bar, it was unknown, if these results applied to atmospheric pressure, as planned for the operation of the drift tubes for the SHiP muon magnetic spectrometer.

By studying drift gas mixtures with Argon and Carbon dioxide in the mixing ratios 90:10 and 93:7, it was found that, due to the rising primary ionization density, the voltage pulse end begins to correlate with the maximum drift time. Using drift gases containing about 1% N_2, a significantly lower maximum drift time and more linear behavior could be attained. The most promising drift gas mixture identified is Ar:CO_2:N_2 96:3:1. Here,

a maximum drift time of

$$t_{\mathrm{drift,max}} = (635 \pm 51)\,\mathrm{ns}$$

was found, which is a decrease to about 40% of the reference gas. Again, the linearity of the rt-relation was tested by a χ^2-test, which results in

$$\frac{\chi^2}{\mathrm{ndf}} = 58.8447,$$

showing a significantly more linear behavior. Both the probability for afterpulses of $P_a = (0.83 \pm 0.03)\,\%$ and the efficiency $\eta = 0.930 \pm 0.001$ are comparable with those of the reference gas. Any further reduction of the CO_2 fraction would lead to an unsuitably increase of the afterpulsing probability. Studies on aging for that drift gas mixture were performed in [72], where no aging indications were found under high irradiation.

For future experiments, the most promising drift gas mixtures, and most importantly the mixture Ar:CO_2:N_2 96:3:1, should be tested in a setup allowing a track reconstruction. The spatial resolution that can be achieved with these new drift gas mixtures needs to be studied. Additionally, longer drift tubes would be preferable so that edge effects become neglegible. The test setup for the OPERA High Precision Tracker at the University of Hamburg thus seems a reasonable choice for future research. It consists of OPERA-type drift tubes with a length of 8 m, arranged in four modules. One of these modules could be filled with the new drift gas mixture, enabling to check the spatial resolution against that of a reference gas. Furthermore, the drift time spectrum's dependence on the high voltage should be analyzed in more detail.

A Electronics

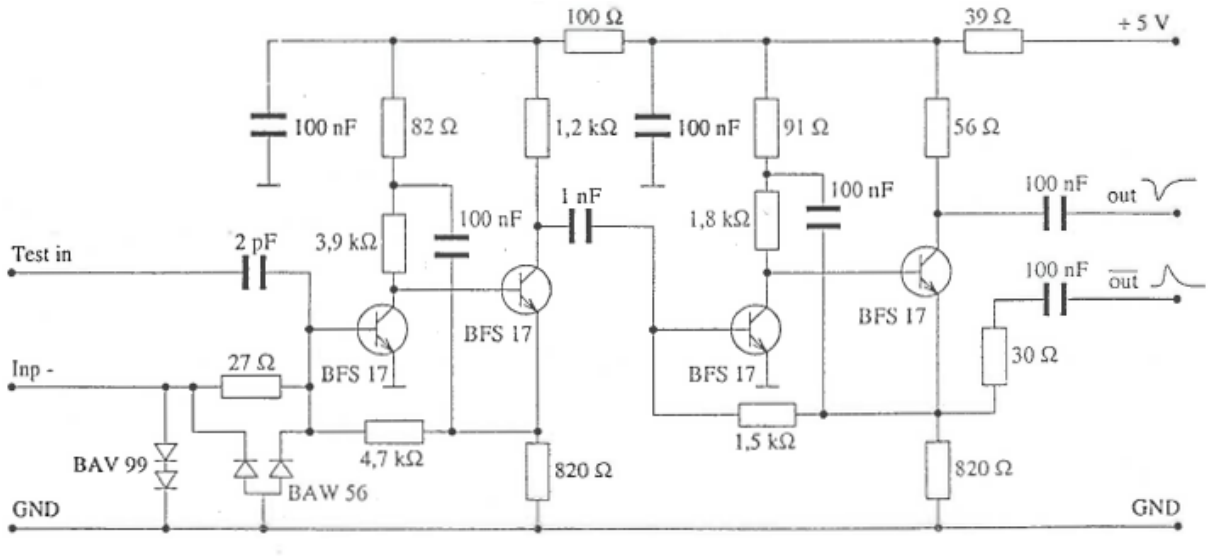

Figure A.1: Circuit layout of the *L3-Amplifier* [71]. It is a differential amplifier, originally designed for the L3 experiment at CERN [83]

B Software

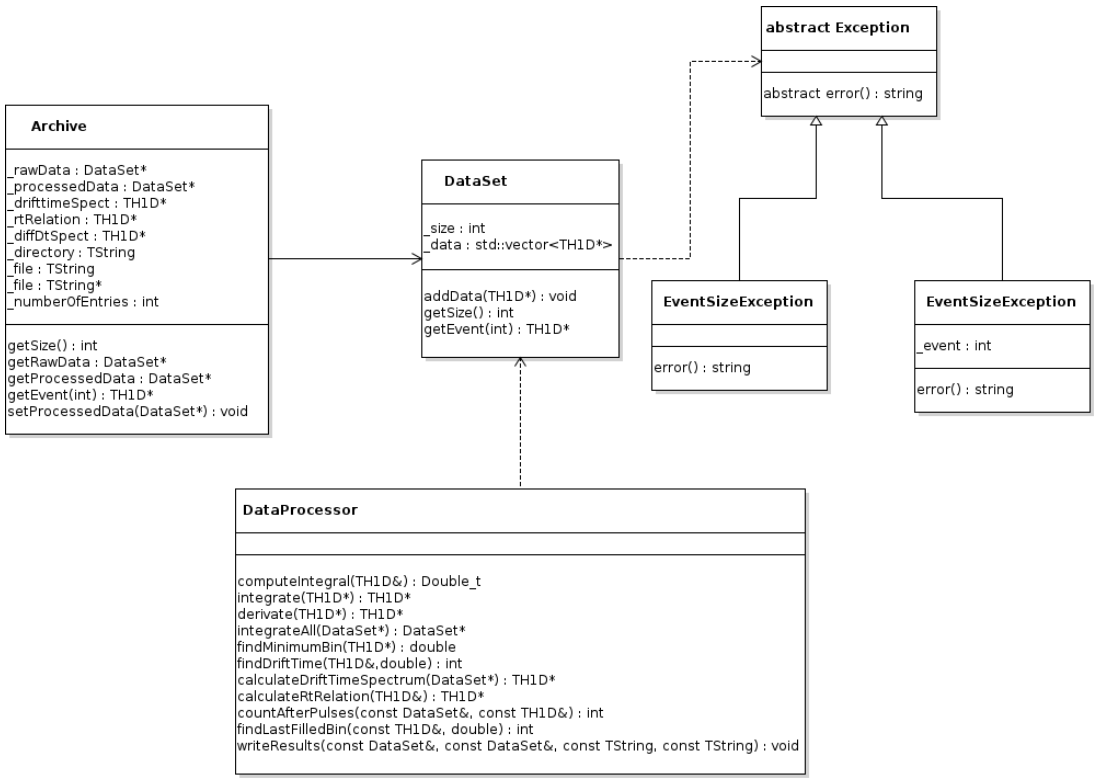

Figure B.1: UML class diagram of the software used for data processing and analysis.

List of Figures

List of Tables

Bibliography

[1] Georges Aad et al. Observation of a new particle in the search for the Standard Model Higgs boson with the ATLAS detector at the LHC. *Phys. Lett.*, B716:1–29, 2012.

[2] K. N. Abazajian et al. Light Sterile Neutrinos: A White Paper. 2012.

[3] K. Abe et al. Observation of Electron Neutrino Appearance in a Muon Neutrino Beam. *Phys. Rev. Lett.*, 112:061802, 2014.

[4] Y. Abe et al. Indication for the disappearance of reactor electron antineutrinos in the Double Chooz experiment. *Phys. Rev. Lett.*, 108:131801, 2012.

[5] H. Abramowicz et al. Measurement of charm fragmentation fractions in photoproduction at HERA. *Journal of High Energy Physics*, 2013(9):58, 2013.

[6] N. Agafonova et al. Discovery of τ Neutrino Appearance in the CNGS Neutrino Beam with the OPERA Experiment. *Phys. Rev. Lett.*, 115(12):121802, 2015.

[7] Q. R. Ahmad et al. Measurement of the Rate of $\nu_e + d \rightarrow p + p + e^-$ Interactions Produced by ^8B Solar Neutrinos at the Sudbury Neutrino Observatory. *Phys. Rev. Lett.*, 87:071301, Jul 2001.

[8] J. K. Ahn et al. Observation of Reactor Electron Antineutrino Disappearance in the RENO Experiment. *Phys. Rev. Lett.*, 108:191802, 2012.

[9] T. Akesson et al. Aging studies for the ATLAS transition radiation tracker (TRT). *Nucl. Instrum. Meth.*, A515:166–179, 2003. [,28(2001)].

[10] C.H. Albright and C. Jarlskog. Neutrino production of M+ and E+ heavy leptons (I). *Nuclear Physics B*, 84(2):467–492, 1975.

[11] Sergey Alekhin et al. A facility to Search for Hidden Particles at the CERN SPS: the SHiP physics case. *arXiv:1504.04855v1*, April 2015.

[12] E. Aliu et al. Evidence for muon neutrino oscillation in an accelerator-based experiment. *Phys. Rev. Lett.*, 94:081802, 2005.

[13] F. P. An et al. Observation of electron-antineutrino disappearance at Daya Bay. *Phys. Rev. Lett.*, 108:171803, 2012.

[14] F. P. An et al. Improved Measurement of Electron Antineutrino Disappearance at Daya Bay. *Chin. Phys.*, C37:011001, 2013.

[15] Takehiko Asaka, Steve Blanchet, and Mikhail Shaposhnikov. The nuMSM, dark matter and neutrino masses. *Phys. Lett.*, B631:151–156, 2005.

[16] Takehiko Asaka and Mikhail Shaposhnikov. The nuMSM, dark matter and baryon asymmetry of the universe. *Phys. Lett.*, B620:17–26, 2005.

[17] ATLAS Collaboration, G. Aad, E. Abat, J. Abdallah, A. A. Abdelalim, A. Abdesselam, O. Abdinov, B. A. Abi, M. Abolins, H. Abramowicz, and et al. The ATLAS Experiment at the CERN Large Hadron Collider. *Journal of Instrumentation*, 3:S08003, August 2008.

[18] G. Bernardi, G. Carugno, J. Chauveau, F. Dicarlo, M. Dris, J. Dumarchez, M. Ferro-Luzzi, J.-M. Levy, D. Lukas, J.-M. Perreau, Y. Pons, A.-M. Touchard, and F. Vannucci. Search for neutrino decay. *Physics Letters B*, 166(4):479–483, 1986.

[19] G. Bernardi et al. FURTHER LIMITS ON HEAVY NEUTRINO COUPLINGS. *Phys. Lett.*, B203:332–334, 1988.

[20] H. Bethe. Zur Theorie des Durchgangs schneller Korpuskularstrahlen durch Materie. *Annalen der Physik*, 397(3):325–400, 1930.

[21] H. Bethe. Bremsformel für Elektronen relativistischer Geschwindigkeit. *Zeitschrift für Physik*, 76(5-6):293–299, 1932.

[22] Walter Blum, Werner Riegler, and Luigi Rolandi. *Particle Detection with Drift Chambers*. Particle Acceleration and Detection. Springer-Verlag Berlin Heidelberg, 2 edition, 2008.

[23] R. Brun and F. Rademakers. ROOT: An object oriented data analysis framework. *Nucl. Instrum. Meth.*, A389:81–86, 1997.

[24] Benjamin Büttner. Beidseitige Auslese an OPERA-Driftröhren zur Rekonstruktion des Durchgangsortes entlang der Rohre. Diplomarbeit, Universität Hamburg, August 2011.

[25] Nicola Cabibbo. Unitary Symmetry and Leptonic Decays. *Phys. Rev. Lett.*, 10:531–533, Jun 1963.

[26] CAEN. *Mod. V1720 8 Channel 12bit - 250MS/s Digitizer*, 26 edition, July 2014.

[27] J. Chadwick. The Existence of a Neutron. *Proceedings of the Royal Society of London A: Mathematical, Physical and Engineering Sciences*, 136(830):692–708, 1932.

[28] Serguei Chatrchyan et al. Observation of a new boson at a mass of 125 GeV with the CMS experiment at the LHC. *Phys. Lett.*, B716:30–61, 2012.

[29] B. T. Cleveland, Timothy Daily, Raymond Davis, Jr., James R. Distel, Kenneth Lande, C. K. Lee, Paul S. Wildenhain, and Jack Ullman. Measurement of the solar electron neutrino flux with the Homestake chlorine detector. *Astrophys. J.*, 496:505–526, 1998.

[30] SHiP Collaboration. A facility to Search for Hidden Particles (SHiP) at the CERN SPS. Technical proposal, CERN, April 2015. arXiv:1504.04956v1.

[31] The ATLAS TRT collaboration. The ATLAS TRT Barrel Detector. *Journal of Instrumentation*, 3(02):P02014, 2008.

[32] C. L. Cowan et al. Detection of the Free Neutrino: a Confirmation. *Science*, 124(3212):103–104, July 1956.

[33] G. Danby, J. M. Gaillard, Konstantin A. Goulianos, L. M. Lederman, Nari B. Mistry, M. Schwartz, and J. Steinberger. Observation of High-Energy Neutrino Reactions and the Existence of Two Kinds of Neutrinos. *Phys. Rev. Lett.*, 9:36–44, 1962.

[34] R. Davis. A review of the Homestake solar neutrino experiment. *Prog. Part. Nucl. Phys.*, 32:13–32, 1994.

[35] Raymond Davis. Solar Neutrinos. II. Experimental. *Phys. Rev. Lett.*, 12:303–305, Mar 1964.

[36] Donato Di Ferdinando. Results from the OPERA experiment. In *NuPhys2015: Prospects in Neutrino Physics (NuPhys2015) London, UK, December 16-18, 2015*, 2016.

[37] W. Diethorn. *A METHANE PROPORTIONAL COUNTER SYSTEM FOR NATURAL RADIOCARBON MEASUREMENTS (thesis)*. Mar 1956.

[38] Zelimir Djurcic et al. JUNO Conceptual Design Report. 2015.

[39] J. Dorenbosch, J.V. Allaby, U. Amaldi, G. Barbiellini, C. Berger, F. Bergsma, A. Capone, W. Flegel, L. Lanceri, M. Metcalf, C. Nieuwenhuis, J. Panman, K. Winter, I. Abt, J. Aspiazu, F.W. Büsser, H. Daumann, P.D. Gall, T. Hebbeker, F. Niebergall, P. Schütt, P. Stähelin, P. Gorbunov, E. Grigoriev, V. Kaftanov, V. Khovansky, A. Rosanov, A. Baroncelli, L. Barone, B. Borgia, C. Bosio, M. Diemoz, U. Dore, F. Ferroni, E. Longo, L. Luminari, P. Monacelli, F. De Notaristefani, P. Pistilli, R. Santacesaria, C. Santoni, L. Tortora, and V. Valente. A search for decays of heavy neutrinos in the mass range 0.5–2.8 GeV. *Physics Letters B*, 166(4):473–478, 1986.

[40] Drifttube software. https://github.com/StBies/Drifttube, 2016.

[41] K. Eguchi et al. First results from KamLAND: Evidence for reactor anti-neutrino disappearance. *Phys. Rev. Lett.*, 90:021802, 2003.

[42] Torben Ferber. Messung der Gaseigenschaften unter Einfluss von molekularem Sauerstoff und Aufbau eines Gassystems für das Driftröhren-Myon-Spektrometer des OPERA-Detektors. Diplomarbeit, Universität Hamburg, July 2006.

[43] E. Fermi. Versuch einer Theorie der β-Strahlen. I. *Zeitschrift für Physik*, 88(3):161–177, 1934.

[44] S. Fukuda et al. The Super-Kamiokande detector . *Nuclear Instruments and Methods in Physics Research Section A: Accelerators, Spectrometers, Detectors and Associated Equipment*, 501(2–3):418–462, 2003.

[45] Y. Fukuda et al. Evidence for Oscillation of Atmospheric Neutrinos. *Phys. Rev. Lett.*, 81:1562–1567, Aug 1998.

[46] Monojit Ghosh, Pomita Ghoshal, Srubabati Goswami, Newton Nath, and Sushant K. Raut. New look at the degeneracies in the neutrino oscillation parameters, and their resolution by T2K, NOνA and ICAL. *Phys. Rev.*, D93(1):013013, 2016.

[47] M. C. Gonzalez-Garcia, Michele Maltoni, and Thomas Schwetz. Updated fit to three neutrino mixing: status of leptonic CP violation. *JHEP*, 11:052, 2014.

[48] David Griffiths. *Introduction to Elementary Particles*. WILEY-VCH, second, revised edition, 2010.

[49] M Güler et al. An appearance experiment to search for $\nu_\mu \nu_\tau$ oscillations in the CNGS beam: experimental proposal. Technical Report CERN-SPSC-2000-028. LNGS-2000-25. SPSC-P-318, CERN, Geneva, Jul 2000.

[50] Zach Hartwig. https://github.com/zach-hartwig/ADAQ.

[51] Makoto Kobayashi and Toshihide Maskawa. CP-Violation in the Renormalizable Theory of Weak Interaction. *Progress of Theoretical Physics*, 49(2):652–657, 1973.

[52] K. Kodama, N. Ushida, C. Andreopoulos, N. Saoulidou, G. Tzanakos, P. Yager, B. Baller, D. Boehnlein, W. Freeman, B. Lundberg, J. Morfin, R. Rameika, S. H. Chung, J. S. Song, C. S. Yoon, P. Berghaus, M. Kubantsev, N. W. Reay, R. Sidwell, N. Stanton, S. Yoshida, S. Aoki, T. Hara, J. T. Rhee, D. Ciampa, C. Erickson, M. Graham, E. Maher, K. Heller, R. Rusack, R. Schwienhorst, J. Sielaff, J. Trammell, J. Wilcox, T. Furukawa, K. Hoshino, H. Jiko, M. Komatsu, M. Nakamura, T. Nakano, K. Niwa, N. Nonaka, K. Okada, B. D. Park, O. Sato, S. Takahashi, V. Paolone,

C. Rosenfeld, A. Kulik, T. Kafka, W. Oliver, T. Patzak, and Schneps. Final tau-neutrino results from the DONuT experiment. *Physical Review D (Particles and Fields)*, 78(5):052002+, 2008.

[53] Hermann Kolanoski. Detektoren in der Elementarteilchenphysik, 2007.

[54] Joachim Kopp, Pedro A. N. Machado, Michele Maltoni, and Thomas Schwetz. Sterile Neutrino Oscillations: The Global Picture. *JHEP*, 05:050, 2013.

[55] Carsten Kreyser. Studien zum Einfluss von Magnetfeldern auf die Funktionsweise von Drahtkammern. Diploma thesis, Universität Hamburg, February 2008.

[56] Z. Maki, M. Nakagawa, and S. Sakata. Remarks on the Unified Model of Elementary Particles. *Progress of Theoretical Physics*, 28:870–880, November 1962.

[57] A. B. McDonald. Sudbury neutrino observatory results. *Phys. Scripta*, T121:29–32, 2005.

[58] G. Mention, M. Fechner, Th. Lasserre, Th. A. Mueller, D. Lhuillier, M. Cribier, and A. Letourneau. The Reactor Antineutrino Anomaly. *Phys. Rev.*, D83:073006, 2011.

[59] D. G. Michael et al. Observation of muon neutrino disappearance with the MINOS detectors and the NuMI neutrino beam. *Phys. Rev. Lett.*, 97:191801, 2006.

[60] Peter Minkowski. $\mu \to e\gamma$ at a Rate of One Out of 10^9 Muon Decays? *Phys. Lett.*, B67:421–428, 1977.

[61] Rabindra N. Mohapatra and Goran Senjanovic. Neutrino Mass and Spontaneous Parity Violation. *Phys. Rev. Lett.*, 44:912, 1980.

[62] NA57 Collaboration and T. Virgili. Study of the production of strange and multi-strange particles in lead-lead interactions at the CERN SPS: the NA57 experiment. *Nuclear Physics A*, 681:165–173, January 2001.

[63] Kyoshi Nishijima. The Super-Kamiokande experiment . *Radiation Physics and Chemistry*, 61(3–6):247–253, 2001. 8th International Symposium on Radiation Physics - {ISRP8}.

[64] K.A. Olive and Particle Data Group. Review of Particle Physics. *Chinese Physics C*, 38(9):090001, 2014.

[65] J. Orloff, S. Lavignac, and M. Cribier, editors. *Seesaw mechanism. Proceedings, International Conference, SEESAW25, Paris, France, June 10-11, 2004*, 2005.

[66] Wolfgang Pauli. Liebe Radioaktive Damen und Herren - Offener Brief an die Gruppe der Radioaktiven bei der Gauvereins-Tagung zu Tübingen, Dezember 1930.

[67] B. Pontecorvo. Neutrino experiments and the problem of conservation of leptonic charge. *Soviet Physics Jetp*, 26:984–988, 1968.

[68] X. Qian and P. Vogel. Neutrino Mass Hierarchy. *Prog. Part. Nucl. Phys.*, 83:1–30, 2015.

[69] Pierre Ramond. The Family Group in Grand Unified Theories. In *International Symposium on Fundamentals of Quantum Theory and Quantum Field Theory Palm Coast, Florida, February 25-March 2, 1979*, page 265–280, 1979.

[70] M. H. Reno. Electromagnetic structure functions and neutrino-nucleon scattering. *Phys. Rev. D*, 74:033001, Aug 2006.

[71] P. Rewiersma. The L3 Wire-Amplifier. *NIKHEF-H*, February 1986.

[72] Alexander Ruschke. Erzeugung von hochenergetischen Neutronen und Protonenbestrahlungen an ATLAS Driftrohren. Diploma thesis, Ludwig-Maximilians-Universität München, December 2010.

[73] F. Sauli. Principles of operation of multiwire proportional and drift chambers. *Lectures given in the academic training programme of CERN*, 1977.

[74] Benedict Schacht. Studie zum zeitlichen Verlauf von Driftröhrensignalen. Bachelor thesis, Universität Hamburg, December 2016.

[75] Jay A. Schecker and David Kestenbaum. Celebrating the Neutrino. *Los Alamos Science*, 25, 1997.

[76] Aldo Serenelli. Alive and well: a short review about standard solar models. *Eur. Phys. J.*, A52(4):78, 2016.

[77] Yuta Takahashi. ATLAS Muon Spectrometer - Status and Performance. Technical Report ATL-MUON-PROC-2009-008, CERN, Geneva, Oct 2009.

[78] J.J. Thomson. Cathode Rays. *Philosophical Magazine*, 90(sup1):25–29, 2010.

[79] Nicola Tyler. Studies on Linear and Fast Drift Gases for ATLAS MDT Chambers. Master thesis, Ludwig-Maximilians-Universität München, August 2011.

[80] Universität Zürich. http://www.physik.uzh.ch/groups/serra/StandardModel.html, April 2016.

[81] A. Vaitaitis et al. Search for neutral heavy leptons in a high-energy neutrino beam. *Phys. Rev. Lett.*, 83:4943–4946, 1999.

[82] F Vannucci. Sterile neutrinos: From cosmology to the LHC. *Journal of Physics: Conference Series*, 136(2):022030, 2008.

[83] M. M. White. Recent results from L3. In *New and exotic phenomena '90. Proceedings, 25th Rencontres de Moriond, 10th Moriond Workshop, Les Arcs, France, January 20-27, 1990*, page 81–93, 1990.

[84] Björn Wonsak. *Die Spurrekonstruktion für das Driftröhren-Myon-Spektrometer des Neutrino-Experiments OPERA*. Dissertation, Universität Hamburg, 2007.

[85] R. Zimmermann et al. The precision tracker of the OPERA detector. *Nuclear Instruments and Methods in Physics Research A*, 555:435–450, 2005.

[86] Kai Zuber. *Neutrino Physics*. CRC Press, Taylor and Francis Group, 2 edition, 2012.

Acknowledgement

The last year was a challenging but very rewarding time. It was an intense time of learning. By the time of writing these words, a thesis completing my studies reaches its finalization. Without a few persons, I might not have reached this point, so I want to thank you.

I would like to thank Prof. Dr. Caren Hagner for the kind acceptance in her research group and making this thesis possible. Thank you for offering me opportunity to visit the collaboration meeting in London.

Additionally, I would like to thank Dr. Daniel Bick for the kind supervision and the great help with lots of questions that arose throughout the last year. You were always there, when things went wrong (and right). Thanks for the fun evenings and a few interesting finds of geocaches.

Furthermore, I want to thank Prof. Dr. Walter Schmidt-Parzefall for the help with electronics and some expedient ideas.

Thank you, Hans-Jürgen Ohmacht for the assistance in the lab and organizing a lot of stuff.

Thank you, Dr. Björn Wonsak, Dr. Björn Opitz, Dr. Joachim Ebert, Annika Hollnagel and. Mikko Meyer for the last-minute help with a lot of questions. To Benedict Schacht for the good cooperation in the lab.

Thanks to Lisa Steppat, David Meyhöfer, Bosse Bein, Simon Reichert and Benedict Kaiser for a lot of fun in our office. Thank you, Henning Rebber, Felix Benckwitz, Katharina Voss and Hauke Schmidt for a great atmosphere to work in.

In addition, I would like to thank Michael Hagemann, Christoph Mangels, David Meyhöfer, Marc Momme, Marcel Völschow and Tobias Wagner[1]. Without you I might not have reached this point.

Of course, a special thank is for my family that supported me throughout my whole studies and was always there. Foremost, I would like to thank Julia Koch for always being by my side. For the constant belief and support for the last few years. Of course, thank you to Julia's family.

Thank you!

[1] in alphabetic order, I hope

Honorable mentions:

- GCC
- ssh
- canteen
- football table
- coffee maker
- everyone that thinks I should have thanked him/her

Erklärung

Hiermit bestätige ich, dass die vorliegende Arbeit von mir selbständig verfasst wurde und ich keine anderen als die angegebenen Hilfsmittel - insbesondere keine im Quellenverzeichnis nicht benannten Internet-Quellen - benutzt habe und die Arbeit von mir vorher nicht einem anderen Prüfungsverfahren eingereicht wurde. Die eingereichte schriftliche Fassung entspricht der auf dem elektronischen Speichermedium. Ich bin damit einverstanden, dass die Masterarbeit veröffentlicht wird.

Hamburg, d. 19.12.2016

S. Bieschke